Kinetic and Microstructural Control of Elemental and Composite Electrodeposited Metallic Thin Films

By

Stephen Louis Gratian Farias

A dissertation submitted to The Johns Hopkins University in conformity with the requirements for the degree of Doctor of Philosophy

Baltimore, Maryland

March, 2014

Abstract

Electrodeposition plays a key role in current industry by providing metallic coatings and nanoscale materials for electronic, optical, magnetic, wear, corrosion, and even aesthetic applications. Current manufacturing processes rely heavily on chemical additives, whose effects are poorly understood, in order to optimize the microstructure and properties of these materials. A novel alternative approach using under potential deposited (UPD) monolayers of a mediating metal to produce high quality metallic materials with low intrinsic stresses and resistivities without the use of complex additives is presented here. Specific attention is given to the deposition of Ag and Cu using Pb as the mediator metal. These materials display up to 85% reductions in intrinsic stress and improved crystal quality compared to samples synthesized in the conventional manner. Applications of this approach for thin film and nanostructured materials processing will be discussed.

Electrochemical deposition of uniformly dispersed and hierarchical composite structures will also be discussed. This technique presents a means of substantially improving the mechanical properties of electroplated material. Specific attention is given to a model Ni matrix - Al_2O_3 nanoparticle composite system. Manufacturing capabilities, scalability, and unique mechanical properties of this system are presented. These mediated and composite deposition techniques are significant advancements in electroplating technology and allow for tuning of microstructures and material properties.

Dedication

This work is dedicated to my parents, Christopher and Maria Farias, who have tirelessly supported me in all of my endeavors. This work is also dedicated to my grandparents Gratian & Philomena Farias and Fabian & Grace Fernandes. Their example and their memory has fueled my academic pursuits.

Acknowledgments

I would first like to thank my mentor, Prof. Robert Cammarata, for his incredible support and patience over my entire graduate career.

I would also like to acknowledge my reader Prof. Jonah Erlebacher and my committee, Prof. Evan Ma, Prof. Tim Weihs, Prof. Michael Bevan, Prof. David Gracias, and Prof. John Schafer for their insights on this work.

There are many faculty members, colleagues, and friends that have made this work possible and my time as a graduate student so enjoyable. I would like to especially acknowledge my past and present lab mates Ike Chi, Austin Young, Nicholas Dee, Tyler Pounds, Rustin Golbani, Maranda Wong, and Patrick Breysse. Special thanks also go to Prof. Patricia McGuiggan, Prof. Kevin Hemker, Mark Koonz, Dr. Gregory Fritz, and Stephen Ryan for their experimental support that made this work possible.

Finally I would like to thank my family, who have supported me for my entire life and my education. Without their backing, inspiration, and occasional prodding, I would not have made it this far. Thank you to my parents, Christopher and Maria, my brothers, Michael and Andrew, and my sister in-law, Kristin.

I will never be able to fully repay all of those who have helped me complete my doctorate, but I hope to make your efforts worthwhile in my future career. I thank you all for your intellectual support, encouragement, and friendship throughout my time at Johns Hopkins.

Table of Contents

Table of Contents

Table of Contents

List of Figures

List of Figures

List of Figures

List of Figures

List of Figures

List of Figures

List of Figures

Chapter 1: Current Challenges in Thin Film and Electrodeposition

Electrodeposition plays a key role in modern industry by providing metal coatings for electronic, optical, magnetic, wear, corrosion, and even aesthetic purposes. Electroplating comprises a ~$6 billion annual industry in the United States alone. In many ways that value is understated as the electroplated materials are not standalone products but vital components in larger devices. Electrodeposition is widely used in industry because it offers a low cost, low temperature, and highly scalable means of depositing metallic thin films. It is also able to conform to unique geometries where physical vapor deposition techniques cannot due to line of sight issues. While there are significant advantages to electroplating metals, it is limited to conductive surfaces and can result in films with very small grains, rough surfaces, and large intrinsic stresses. Despite industry's reliance on electrodeposited materials, the science behind this crucial manufacturing technology is still poorly understood. In order to take full advantage of the capabilities of this technique, it is necessary to continue exploring the kinetic processes behind electrodeposition and the unique microstructures and properties attainable in electrodeposited materials.

One important example of industrial use of electrodeposited materials is in the manufacturing of electrical interconnects in integrated circuits. Electrodeposited copper is the material of choice for these devices that operate all modern inorganic electronics.

Chapter 1: Current Challenges in Thin Film and Electrodeposition

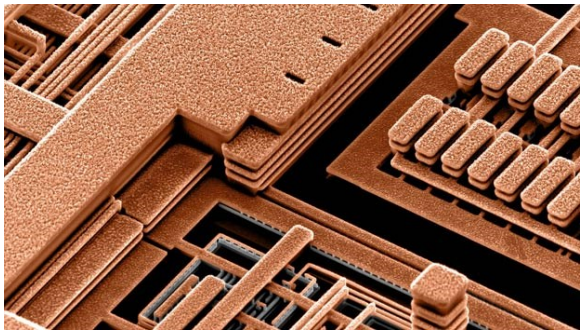

Figure 1: Electrodeposited Copper in Integrated Circuit:

Many complex geometries and small features need to be plated reliably in order to manufacture these architectures [1].

Most electrochemical research on improving copper film quality to date has focused on using various additives to influence electrodeposition. These additives are generally thought to influence surface energies at the deposition surface or influence ion motion through near the charged surface, but these behaviors are not well understood. Additives can significantly improve the quality and efficiency of electrodeposition but their effects are purely empirically determined. Their beneficial effects are also a direct function of the concentration of the additive in the electrolyte and this concentration often varies as the additive is depleted during deposition. More robust solutions for depositing Cu and other materials of interest are needed to further improve film quality and to meet rising industrial demands on plated materials.

Mediating electrochemical deposition using under potentially deposited (UPD) monolayers provides a unique and controllable means of affecting electrodeposition. Instead of adding substances with ambiguous influence on deposition, UPD monolayers

act as a direct atomic barrier layer to deposition with coverage as a well determined function of applied voltage. This allows for direct control of the UPD additive throughout deposition and an active means of controlling kinetics. By controlling the kinetics of deposition it may be possible to alleviate the problems of small grain sizes, rough surfaces, and large intrinsic stresses in electrodeposited thin films.

This type of controlled mediated deposition has already been demonstrated as a means of manufacturing large grained and smooth Ag films [2,3], but little work has been done to study how this change in microstructural development affects the stress development in the films. The resultant microstructures from mediated growth should correlate with low intrinsic stress in the deposited film, which would be a significant beneficial attribute for industrial purposes. There has also been little work put into exploring other potential mediated deposition systems. Correlating stress behavior to this change in kinetics and to extending this technique to other deposition systems would represent a substantial advancement in electrodeposition.

Many other electroplated materials are used for surface protection especially from mechanical and chemical wear. One of the key materials of interest for this purpose is nickel. Nickel has very good chemical corrosion resistance but needs to be strengthened to stand up to the mechanical requirements of coatings in many applications [4,5]. Current research in strengthening metal coatings has largely focused on developing nanocomposites and ordered composite structures, but most current manufacturing technologies are process intensive and expensive. Recent developments in

manufacturing metal matrix-ceramic nanocomposites using electrochemical deposition has opened up the possibility of electroplating unique hierarchical composite systems and functionally graded materials [6,7].

Hierarchical ordered materials have grown as a topic of research interest since the 1990s. Natural materials with these unique constructions have strength to weight ratios and failure properties vastly superior to any manmade materials to date [8,9]. These materials have controlled composite structures at nanometer length scales as well as higher order structures ranging from nanometer to 100 micron length scales. While maintaining these finely controlled microstructures and nanostructures, these materials can exist at bulk size scales. Simulations and analytical models on these structures indicate that manufactured artificial hierarchical materials would display superior properties compared to those produced by most current industry technologies. Despite extensive research into studying natural materials, limited progress has previously been made in actually manufacturing materials with these unique structures and properties. Much of the difficulty in manufacturing these hierarchical structures has come in controlling them at both nanoscale and macroscopic length scales. While there are many refined techniques for creating nanostructures and processing bulk materials, generating these nanostructures in bulk quantities and organizing them over large scales has proved challenging.

Many top-down designs of artificial hierarchical composites have been proposed over the past two decades. These structures have been proposed and used for engine,

armor, and tool technologies. Specific attention has been given to functionally graded materials (FGM), which serve as a transition material between a bulk substrate and a surface coating. Industry devices often require tough and light weight core materials but hard and wear resistant outer surfaces. This problem is largely solved by surface coatings, but these coatings have also led to a new set of materials problems due to the properties mismatch between the core material and outer casing. Under thermal or mechanical loading, differences in thermal expansion or modulus lead to stress concentrations in the device. These stress concentration in turn lead to fatigue failure. FGMs are compositionally graded materials that transition from the core material to the casing material over a defined volume. By taking the properties mismatch and spreading it over a larger volume, it is possible to reduce the stress concentrations. FGMs are currently manufactured in industry but require process intensive techniques. The often drastic difference in material properties makes it difficult to process the materials together, and the techniques that have been developed tend to require layer by layer manufacturing and require dozens of processing steps. Many of the current manufacturing techniques also result in micro-cracks and void formation that counteract the benefits of stress reduction on fatigue life. Thus developing a facile method of creating an FGM that is continuous and crack free has significant industrial applications.

Electrochemical deposition provides unique means of tackling many of the difficulties that have hindered the synthesis of artificial high order composite structures. Deposition rates can be finely tuned to nanometers/minute, but these same systems can

also be robust enough to deposit at rates on the order of microns/minute. Additionally, total deposition thicknesses of the order of millimeters can be achieved. It has been shown in previous work that electrodeposition can also be used to create uniform, void-free metal-ceramic nanocomposite structures. By using a rotating disk electrode (RDE) system in an electrolyte solution that contains a suspension of ceramic nanoparticles, it is possible to imbed these particles into the metal matrix as the metal ions are being deposited. While metal-matrix composite deposition has been in use since the 1970s, this unique system allows for control of the oxide volume fractions of the metal-ceramic composites as a function of rotation rate in addition to deposition current per unit area. The ability to finely control nanoparticle incorporation and metal deposition at nanometer to millimeter length scales makes electrodeposition in an RDE system an ideal process for overcoming the challenges that have stifled the manufacturing of artificial hierarchical structures. Developing this system would extend electroplating to meet many of the new materials demands in industry.

In the body of this dissertation, I will discuss work relating to UPD mediation of Ag and Cu systems. I will present the kinetically controlled structural evolution of mediated Ag systems and corresponding changes in the stress evolution of these films. I will also present work on mediation of Cu deposited films including structural development resulting in desirable property changes. This work on mediated electrochemical deposition represents significant enhancement in kinetic control of electroplating. I will additionally discuss electrochemical deposition of Ni-Al_2O_3

hierarchical and functionally graded composite structures. I will specifically detail the manufacturing capabilities and scalability of this technique. I will also present unique mechanical properties attainable using these composite structures.

References

1. History of Copper Interconnects, http://www-03.ibm.com/
2. Sieradzki, K., et al. Electrochemical Defect-Mediated Thin-Film Growth. Science **284**, 138-141 (1999).
3. Brankovic, S., et al. Surfactant mediated electrochemical deposition of Ag on Au (111). *Electrochemical and Solid-State Letters* **2**, 443-445 (1999).
4. Garciaa I., et al. Electrodeposition and sliding wear resistance of nickel composite coatings containing micron and submicron SiC particles. *Surface and Coatings Technology* **148**, 171–178 (2001)
5. Schuh C., et al. Hall–Petch breakdown manifested in abrasive wear resistance of nanocrystalline nickel. *Scripta Materialia* **46**, 735-740 (2002)
6. Shao, X. Synthesis and Characterization of Soft Magnetic Thin Films, Nanocomposites, and Nanowires by Electrodeposition. (2002).
7. Shao, I., Vereecken, P. & Chien, C. Synthesis and characterization of particle-reinforced Ni/Al2O3 nanocomposites. *Journal of Materials Research* **17**, 1412-1418 (2002).
8. Mortensen, A. & Suresh, S. Functionally graded metals and metal-ceramic composites: Part 1 Processing. *International Materials Reviews* **40**, 239-265 (1995).
9. Suresh, S. & Mortensen, A. Functionally graded metals and metal-ceramic composites: Part 2 Thermomechanical behaviour. *International Materials Reviews* **42**, 85-116 (1997).

Chapter 2: Fundamentals of Electrodeposition and Thin Film Growth

2.1 Fundamentals of Electrochemistry

All electrochemical reactions can be considered a unique subset of reduction-oxidation (Redox) reactions. In reduction reactions atoms of one species in their oxidized state will take on electrons to change into their reduced state. Oxidation reactions are the inverse of reduction reactions where atoms in their reduced state will expel electrons to change into their oxidized state. Oxidation and reduction reactions will often occur in tandem where one species of atoms will oxidize and donate its electrons to a distinct species of atoms, which will in turn be reduced. This reaction will occur depending on the relative stabilities of the species as determined by their reduction potentials (energetic propensity to be in the reduced state). If the reduction potential of species 1 is lower than that of species 2, the constituents will be driven to keep species 1 in its reduced state and species 2 in its oxidized state. This will happen until the reactions reach an equilibrium concentration of each species in its given state. In these simple coupled Redox reactions the oxidation reaction directly supplies electrons to the enable the reduction reaction.

$O_1 + ne^- \rightarrow R_1$ (Reduction, Cathodic Reaction)

$R_2 \rightarrow O_2 + ne^-$ (Oxidation, Anodic Reaction)

Electrochemical reactions differ from these direct exchange scenarios by physically separating the oxidation and reduction reactions and having the electrons transfer through an electrical conductor. If system is not equilibrium, Redox reactions will occur and current will be passed through the conductor. This is effectively how

chemical batteries are able to supply electrical power. The cells of the battery are in a non-equilibrium state and when the electrical circuit is connected, the Redox reaction occurs to drive the system towards equilibrium and generates a current in doing so. Instead of drawing current from electrochemical reactions, electrical power can be supplied to the system to drive the reaction in a desired direction. When recharging a battery, current is run through the system to bring it to a non-equilibrium chemical state.

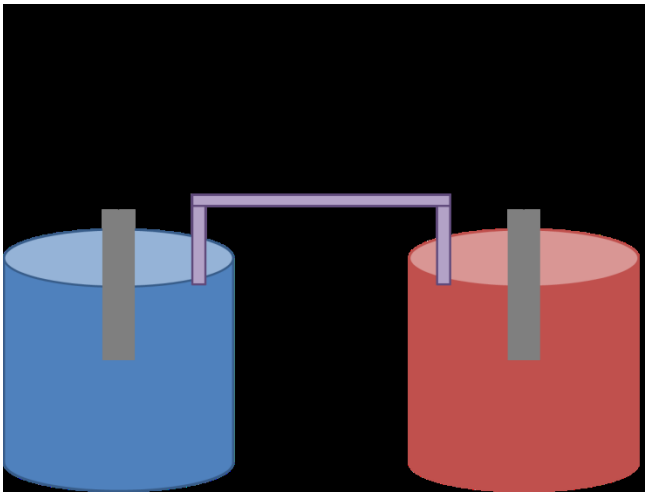

Figure 2: Electrochemical (Galvanic) Cell showing two half-reactions. The oxidation reaction occurs at the anode and the balancing reduction reaction occurs at the cathode

Since the reduction and oxidation reactions in electrochemical systems are physically separated, we can look at each reaction as an independent system. The isolated reduction or oxidation reaction is referred to as a "half reaction." Experimental and theoretical studies are typically carried out on half cells and half reactions in order to simplify problems to an isolated system. In electrodeposition we are specifically

interested in the reduction half reaction. Here electrons supplied through the cathode, also referred to as the working electrode, combine with metal ions in solution. The positive metal ions (dissolved in a solution) are the oxidative state of the species and accept the electrons to form a neutral atom at the electrode surface. This metal atom is in solid form and will attach to the cathode surface. Thus by passing a current through the system it is possible to grow a metallic layer on the cathode surface. This current does not have to be driven by a corresponding oxidation reaction, but can be supplied by any electrical power source.

This electrically driven half reaction is described by the Nernst equation (EQ 2.1). This equation results from balancing the electrical and chemical work associated with the reaction [1,2]:

$$U_{eq} = U_{eq}^{*} + \frac{RT}{nF}\ln\left(\frac{a_O}{a_R}\right) \qquad \text{EQ 2.1}$$

where U_{eq} is the equilibrium potential, U_{eq}^{*} is the standard potential, R is the ideal gas constant, T is the temperature, n is the charge number of the ion, F is Faraday's constant, a_O is the activity of the oxidized species, and a_R is the activity of the reduced species.

If the system is held at U_{eq}, the solid metal species is at equilibrium with its ionic counterpart and no net reaction occurs. If a negative voltage (over potential) relative to U_{eq} is imposed, metal ions from the solution will deposit onto the cathode or working electrode. Vice versa, if a positive voltage relative to U_{eq} is imposed, metal atoms on the cathode will be ionized and dissolved into the solution. Electrochemical potentials are typically measured relative to a reference electrode. The reference electrode is a third

electrode in the electrolyte that does not pass current (is independent of the electrochemical reaction) but can be used to monitor the potential of the electrode of interest. U_{eq} is typically reported relative to a Standard Hydrogen Electrode (SHE). Other common reference electrodes include a Saturated Calomel Electrode (SCE), where the potential is 0.242V above SHE, and an Ag/AgCl electrode, where the potential is 0.2V above SHE. It is also common in electroplating to use a pure foil of the material being deposited as the reference electrode. This exposed metal reference will be at the equilibrium potential, thus applying a negative voltage bias to the working electrode relative to the reference will result in deposition and applying a positive bias will result in stripping of the material. This technique effectively zeroes the system around the equilibrium potential.

It is also worth noting that very thin films or even single monolayers of material can sometimes be deposited at voltages above the equilibrium voltage described by the Nernst equation. This is because the Nernst equation only considers bulk thermodynamic values and ignores changes in free energies due to surface effects, which can be significant at small length scales.

If the elemental form of metal M has a favorable surface interaction (or work function) with the electrolyte solution compared to the substrate material S such that EQ 2.2 is satisfied, it is possible to deposit M at a potential positive of the equilibrium potential in order to cap the high energy surface:

$$\gamma_{SE} > \gamma_{MS} + \gamma_{ME} \qquad \text{EQ 2.2}$$

where γ_{SE} is the energy of the substrate-electrolyte interface, γ_{MS} is the energy of the M-substrate interface, and γ_{ME} is the energy of the M-electrolyte interface. This reduction of ions at voltages higher than Ueq is commonly referred to as underpotential deposition (UPD). It is driven by surface energies and will not result in bulk deposition of the metal. In fact UPD films can often be single atomic monolayers covering the underlying material. UPD behavior has been studied for decades and significant attention has been given to Ag, Au, Pt, and Cu as substrate materials [3,4].

While the Nernst equation and properly describes the thermodynamic stability of the system at a given voltage, it does not fully predict the chemical kinetics of the plating or dissolution reactions. The reaction kinetics of electroplating are a direct function of the electrical current passed through the system. The ions in solution are the charge carriers in the electrolyte segment of the completed circuit and therefore the rate of ions being reduced must be directly proportional to the current passed through the system. This relation is shown in EQ 2.3 [1,2]:

$$I = nFAv \qquad \text{EQ 2.3}$$

where I is the reaction current, n is the valence state of the ion, F is Faraday's constant, A is the area of the electrode, and v is the reaction rate.

In addition to the deposition reaction, some current can also be passed to charge the electric double layer. This layer is a water cage that builds around the working electrode as the polar water molecules orient around the applied electric field. Thus electrical work is done to move the molecules rather than reduce metal ions. This step

can be thought of as charging a capacitor and does not result in a chemical reaction. This current will also be transient and diminish to zero once the double layer is formed. Thus only the current described in EQ 2.3 will be considered here.

It is typical to consider two distinct regimes for the reaction kinetics of an electrochemical system, a reaction-limited regime and a mass-transfer limited regime. In the reaction-limited regime the chemical reaction is occurring slowly enough that diffusion is able to maintain a constant concentration of species at the electrode surface. In the mass-transfer limited regime, the chemical reaction occurs readily and chemical species available at the electrode surface is consumed creating a depletion zone where the concentration is lower than the bulk solution concentration. Diffusion of species across this depletion zone is then what controls the rate of the reaction and the current passed through the system under these conditions.

By monitoring the current at different applied potentials it is possible to fully map out the different kinetic regimes relative to the Nernst potential. This is often done by running a cyclic voltammogram which sweeps the potential between set limits while recording the current.

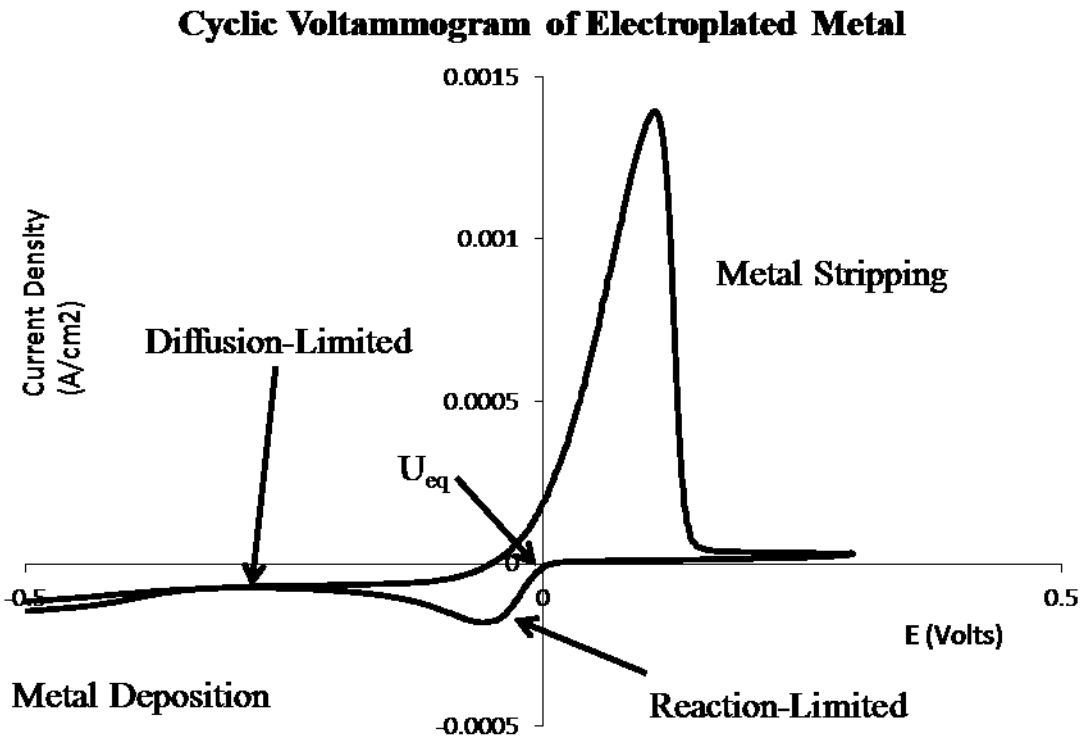

Figure 3: Cyclic Voltammogram of Electroplated Metal. Shows reaction-limited current at potentials just negative of equilibrium and diffusion limited for large negative potentials.

As seen in Figure 3 the reduction reaction beings to occur at potentials negative of the equilibrium potential. This is seen as a change from zero current to increasingly negative currents with increasingly negative voltages. This is the reaction limited regime where deposition rates are controlled directly by the overpotential and the solution is effectively able to supply an unlimited source of ions for the reaction to occur. This behavior is described by the Butler-Volmer Relation (EQ 2.4) [1,2]:

$$I = FAk^0 C_O^{1-\alpha} C_R^{\alpha} \left[exp\left(\frac{\alpha F(U-U_{eq}^*)}{RT}\right) - exp\left(-\frac{(1-\alpha)F(U-U_{eq}^*)}{RT}\right)\right] \qquad \text{EQ 2.4}$$

where k^0 is the exchange rate constant, C_O and C_R are the concentrations of the oxidant and reductant respectively, and α is the transfer coefficient (typically taken to be 0.5).

At even greater overpotentials, the reaction rate occurs too fast for the electrolyte solution to supply sufficient ions to the working electrode. In this regime the current is limited by the diffusion of ions from the bulk solution to the surface, so the current levels off at a fixed value. This diffusion limited current is the greatest sustainable reaction rate the solution can attain in a static setup and follows the Cottrell relation (EQ 2.5) as a function of the diffusivity, *D*, and time, *t*. [1,2]:

$$I = \frac{nFAC_R\sqrt{D}}{\sqrt{\pi t}} \qquad \text{EQ 2.5}$$

Work discussed in subsequent chapters will be focused on the diffusion limited deposition regime of a given electrochemical system.

2.2 Fundamentals of Thin Film Growth Kinetics and Stress Evolution

The reaction kinetics described in Section 2.1 determine the rate at which oxidized species are reduced. In the case of metal deposition, this rate is effectively the flux of ions reaching the electrode and becoming neutral atoms. How these atoms organize during this flux will be guided by thin film growth kinetics. Most thin film deposition can be characterized under three distinct growth modes. Frank-van der Merwe (F-VM) Growth is layer by layer growth and can occur when EQ 2.6 is satisfied so that

the depositing material will completely wet the substrate. Volmer-Weber (V-W) Growth occurs when the conditions of EQ 2.7 are met and results in discrete 3-D islands nucleating, growing, and eventually coalescing into a continuous film. Stranski-Krastanov (S-K) growth described a growth mode in between F-VM and V-W growth where initial deposition is layer by layer on top of the substrate but eventually 3D islands nucleate on the free surface and begin to grow and coalesce [5-7]:

$$\gamma_{sl} > \gamma_{sf} + \gamma_{fl} \qquad \text{EQ 2.6}$$

$$\gamma_{sl} \leq \gamma_{sf} + \gamma_{fl} \qquad \text{EQ 2.7}$$

where γ corresponds to the surface stress between the substrate, film and liquid interfaces as indicated by subscripts.

This results from analyzing the contact angle, θ, imposed from Young's Equation, $\gamma_{sl} = \gamma_{sf} + \gamma_{fl}\cos(\theta)$. As θ approaches zero the depositing material will completely wet the surface and deposition will proceed as single layers developing on top of one another. If θ is greater than zero, the surface thermodynamics are such that the depositing material will form a discrete hemispherical cap. This condition corresponds to individual island nucleation and growth.

S-K growth modes often occur because of epitaxial (crystal lattice matching) strains induced in the film. Though the depositing material will wet the surface, there is a misfit strain due to the difference in atomic spacing (lattice parameter) of the substrate and the film. This growing film will accommodate this strain until it reaches a critical film thickness where the strain volume energy is high enough that the system will favor

formation of defects over continued epitaxial growth [6-9]. This introduction of defects is often linked with the nucleation of 3-D islands. In addition to this thermodynamic-mechanically driven process, kinetic limitations of the system can also lead to S-K growth modes. In kinetically driven S-K growth 2-D monolayer islands form and grow but the continuous influx of atoms to the deposition surface results in nucleation of a second monolayer [9,10]. This is a purely kinetic process that leads to 3-D island formation.

All three of these growth modes can lead to films with epitaxial stress due to substrate-film lattice mismatches, though substantial differences in epitaxy will result in V-W growth or S-K growth in thick films. The epitaxial misfit strain can be written as a function of the lattice parameters of the two materials, *a*. [6-9]

$$\varepsilon_m^{epitaxy} = \frac{a_{film} - a_{substrate}}{a_{substrate}} \qquad \text{EQ 2.8}$$

In addition to epitaxial stress systems can also experience misfit strains from mismatches in coefficient of thermal expansion, *CTE*, if the component experiences a temperature change from the temperature during formation of the film [6-8]

$$\varepsilon_m^{epitaxy} = \left(CTE_{film} - CTE_{substrate}\right)(T - T_0) \qquad \text{EQ 2.9}$$

Finally, growing films can also experience intrinsic stresses or misfit strains due to nucleation, growth, coalescence, and continued growth of the film itself [6-9, 11-16]. V-W and S-K growth are also linked with intrinsic stress development associated with the 3-D growth of the films. This intrinsic stress development is generally found to have three unique phases linked to structural evolution of the growing film. Very early film

growth can experience compressive film stresses during Nucleation of initial 3-D islands. Tensile jumps in film stress are generally observed as the islands begin to coalesce and percolate. After the film is continuous, compressive stress can continue to develop and evolve for a variety of reasons including continued nucleation stress and adatoms migrating into the grain boundaries. The developing stress is directly linked to the structural development of the film. These stresses are important in manufactured films as they can lead to significant bowing of the film, hillock formation, and creep deformation. They can even be large enough to result in cracking, buckling, and delamination failures of the film.

2.3 References

1. Bard, A. J. (2001). Electrochemical Methods: Fundamentals and Applications, 2nd Ed. New York: Wiley.
2. Brett, C. M. (1993) Electrochemistry: Principles, Methods, and Applications, New York: Oxford
3. Kolb, D., Przasnyski, M. & Gerischer, H. Underpotential deposition of metals and work function differences. *Journal of Electroanalytical Chemistry and Interfacial Electrochemistry* **54**, 25–38 (1974).
4. Bewick, A. & Thomas, B. Optical and Electrochemical Studies of the Under-Potential Deposition of Metals Part III. Lead Deposition on Silver Single Crystals. *Journal of Electroanalitical Chemistry* **84**, 127-140 (1977).
5. Herrero, E., Buller, L.J. & Abruña, H.D. Underpotential deposition at single crystal surfaces of Au, Pt, Ag and other materials. *Chemical reviews* **101**, 1897-930 (2001).
6. Nix, W.D. *Mechanical Properties of Thin Films*. *Class Notes* (2005).
7. Seshan, K. Handbook of Thin-Film Deposition Process and Techniques: Principles, Methods, Equipment and Applications (2nd edition, 2002).
8. Thompson, C.V. Grain Growth in Thin Films. *Annu. Rev. Mater. Sci* **20**, 245-268 (1990)
9. Thompson, C.V. Structure Evolution During Processing of Polycrystalline Films. *Annu. Rev. Mater. Sci* **30**, 159-190 (2000)

10. Tersoff, J., et al. Critical Island Size for Layer-by-Layer Growth. *Physical Review Letters* **72** (1994)

11. Rosenfeld, G., Servaty, R., Teichert, C., Poelsema, B. & Cosma, G. Layer-by-layer Hrowth of Ag on Ag(111) Induced by Enhanced Nucleation: A Model Study for Surfactant-Mediated Growth. *Physical Review Letters* **71**, 895-898 (1993).

12. Floro, J., Chason, E. & Cammarata, R. Physical Origins of Intrinsic Stresses in Volmer – Weber Thin Films. *MRS Bulletin* 19-25 (2002)

13. Seel, S., et al. Tensile Stress Evolution During Deposition of Volmer-Weber Thin Films. *J. Applied Physics* **88** (2000)

14. Chason, E., et al. Origin of Compressive Residual Stress in Polycrystalline Thin Films. *Physical Review Letters* **88** (2002)

15. Freund, L. B. and Suresh, S. Thin Film Materials: Stress, Defect Formation and Surface Evolution, Cambridge University Press (2004).

Chapter 3: Effects of Pb Mediation on Ag Electrodeposited Films

3.1 Introduction

As noted in Chapter 1, electrodeposition plays a key role in modern industry by providing metal coatings for electronic, optical, magnetic, wear, corrosion, and even aesthetic purposes. Electrodeposition is widely used in industry because it offers a low cost, low temperature, and highly scalable means of depositing metallic thin films. It is also able to conform to unique geometries where physical vapor deposition techniques cannot due to line of sight issues. While there are significant advantages to electroplating metals, it is limited to conductive surfaces and can result in films with very small grains, rough surfaces, and large intrinsic stresses. It is also a relatively "dirty" process compared to ultra-high vacuum (UHV) and chemical vapor deposition (CVD) techniques. Despite industry's reliance on electrodeposited materials, the science behind this crucial manufacturing technology is still poorly understood. In order to take full advantage of the capabilities of this technique, it is necessary to continue exploring and improve upon current electroplating techniques.

One of the reasons electrochemical research has proven challenging is the wide use of many chemical additives to electroplating solutions to try and improve film quality. These additives are generally thought to influence surface energies at the deposition surface or influence ion motion through the electric double layer that forms at the charged surface, but these behaviors are not well understood. Additives can significantly improve the quality and efficiency of electrodeposition but their effects are

purely empirically determined and can often result in contamination of the film [1,2]. Their beneficial effects are also a direct function of the concentration of the additive in the electrolyte and this concentration often varies as the additive is depleted during deposition. Mediating electrochemical deposition using under potentially deposited (UPD) monolayers provides a unique and controllable means of effecting electrodeposition. Instead of adding substances with ambiguous influences on deposition, UPD monolayers act as a direct atomic barrier layer to deposition with coverage as a well determined function of applied voltage. This allows for direct control of the UPD additive throughout deposition and an active means of controlling growth kinetics. By controlling the kinetics of deposition it is possible to alleviate the problems of small grain sizes, rough surfaces, and large intrinsic stresses in electrodeposited thin films.

This type of controlled mediated deposition has been demonstrated as a means of manufacturing large grained and smooth Ag films on single crystal Au (111) substrates [3,4]. This kinetic manipulation has even been shown to result in 2-D layer by layer growth rather than 3-D island formation, which is typically seen Ag deposition. However, little work had previously been done to study how these changes in microstructural development affect stress development in the films or the applicability of this technique to polycrystalline substrates. Here we present results of in situ stress measurements taken during Pb mediated electrochemical growth of Ag films on polycrystalline Au (111) substrates. It is shown that the structural and kinetic changes

from mediation correlate to significant decreases in the intrinsic stress development in Ag films.

3.2 Background

3.2.1 Thin Films Growth Modes and Kinetically Driven Stranski-Krastanov Growth

As described in Chapter 2, most thin film deposition can be characterized under three distinct growth modes. Frank-VanderMerwe Growth is layer by layer growth and can occur when surface energies are satisfied such that the depositing material will completely wet the substrate. Volmer-Weber Growth occurs when the film will not completely wet the substrate and results in discrete 3-D islands nucleating, growing, and eventually coalescing into a continuous film [5-9]. Stranski-Krastanov growth is a unique growth mode where initial deposition is layer by layer on top of the substrate but eventually 3-D islands nucleate on the free surface and begin to grow and coalesce. S-K growth can either occur thermodynamically due to epitaxial strain in the growing film or it can occur due to growth kinetics [3,10-12]. Here we will focus on kinetically induced S-K growth.

In general kinetically limited thin film growth is thought to be determined by D/L^2, where D is the surface diffusivity and L is the characteristic length scale of an isolated atomic terrace as shown in Figure 4. We will consider this terrace part of the first monolayer of atoms on top of a substrate. This factor is the approximate rate at which an adatom, an individual atom sitting on a surface, will sample the edges of the terrace. If D/L^2 is sufficiently large, adatoms will frequently sample the edges of the terrace and

will have opportunity to jump the ledge and attach to the edge of the terrace [12-18]. This process will allow the terrace to continually grow laterally. As the terrace grows, L increases and lowers the edge sampling frequency. Eventually, if the 2-D terrace grows sufficiently large, the adatoms will randomly coalesce to nucleate a new terrace on top of the existing one. This creates a second monolayer of atoms on top of the first. This new nucleated terrace will grow laterally until it approaches the size of the underlying terrace at which point an additional terrace will nucleate on top of the structure. This stack of terraces will continue to grow laterally and vertically, effectively forming 3-D islands (see Figure 5) like those seen in Volmer-Weber growth. This kinetic limitation can be thought of relative to a few distinct physical attributes of the system. First, if the diffusivity is relatively high, adatoms at the surface are able to move to the edges of the terrace fast enough that it will grow outward. However, we will demonstrate that the nucleation of a new terrace stack will also increase with diffusivity so this offers limited improvement in lateral growth. Second, if the energy required for an adatom to jump over the ledge of the terrace (Schwoebel barrier) is lowered, lateral growth can be promoted. Third, if the density of terraces in the first monolayer is high enough, they will coalesce before reaching large L values. This allows for completion of the first monolayer before new terraces begin to form the second monolayer and results in layer-by-layer growth similar to that seen in Frank-VanderMerwe growth.

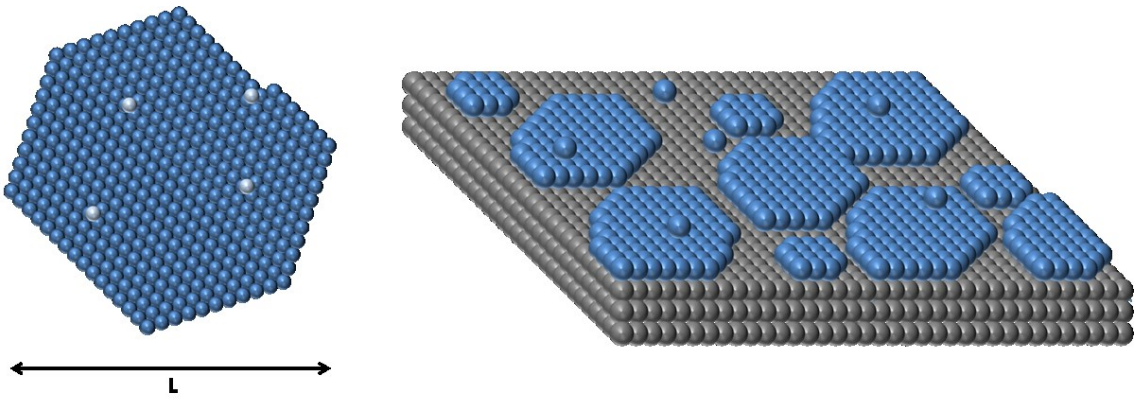

Figure 4: Schematic of 2-D Terrace Nucleation on a Substrate. In order to have continued layer by layer growth the adatoms on top of the terraces must be able to jump over the terrace edge and attach to the expanding terrace instead of nucleating a new 2-D terrace on top of the existing one. The nucleation density will control the maximum terrace size, L, of the growing monolayer. A high nucleation density will allow for the 2-D islands to grow and coalesce together before individual islands are large enough to nucleate multiple atomic layers.

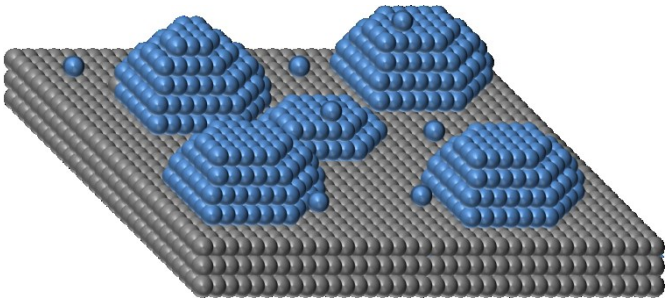

Figure 5: Schematic of Stacks of 2-D Terraces Forming 3-D Islands. A low nucleation density of terraces in the first monolayer will result in new levels of terraces forming before coalescence of the first monolayer.

Chapter 3: Effects of Pb Mediation on Ag Electrodeposited Films

We will now explore a more rigorous mathematical derivation of the kinetic process allowing for continued 2-D growth or resulting in stacks of 2-D terraces forming 3-D islands. In this derivation we will consider the rate at which stable nuclei form on top of a terrace relative to the growth rate of the terrace itself and determine the fraction of terraces that have nucleated a second layer. This was proposed by Tersoff et al [12].

Diads, two bonded surface atoms, are assumed to be stable nuclei in our system. The individual adatoms are in quasi-equilibrium and formation of a diad eliminates free surface in favor of forming a metallic bond. This assumption is often used in analytical solutions to adatom nucleation problems. We can write the nucleation rate, r, of the diads as:

$$R_{diad} = DC_{ad}^2 a^{-4} A_{diad} e^{-Qdiad/kT} \quad \text{EQ 3.1}$$

where D is the surface diffusivity, C_{ad} is the unitless concentration of adatoms in number of adatoms per number of lattice sites, a is the lattice parameter, and $A_{diad}e^{-Qdiad/kT}$ is an Arrhenius dependence that represents the probability of two adatoms that meet will form a diad. For our purposes we will assume $A_{diad}e^{-Qdiad/kT}$ is equal to 1.

In order to determine C_{ad} we will assume a dilute number of diads on top of the terrace and a steady state approximation for the concentration. That is to say the flux of atoms into the system is compensated by the attachment of adatoms to the edge of the initial terrace and the formation of diads but we are ignoring the growth of diads:

$$\frac{dC_{ad}}{dt} = D\nabla^2 C_{ad} + a^2 F \quad \text{EQ 3.2}$$

$$C_{ad} = C_{ad}^{0} - \frac{F}{4D} a^2 l^2 \qquad \text{EQ 3.3}$$

where F is the flux of adatoms to the surface and l is the position.

At steady state the change in concentration at the edge of the island must be balanced with the net rate of atoms moving across the ledge, giving the boundary condition $^{dC_{ad}}/_{dl} + {}^{C_{ad}P_{edge}}/_{a} = 0$ at the edge of the island, where P_{edge} is the relative probability of an atom crossing down to the ledge from the terrace versus leaving the ledge and moving onto the terrace. This allows us to solve for C_{ad}^{0}.

$$C_{ad}^{0} = \frac{F}{4D} a^2 \left(L^2 + L \frac{2a}{P_{edge}} \right) \qquad \text{EQ 3.4}$$

We can now express the nucleation rate as a function of island size. For the case of P_{edge} being small, we find that:

$$R' = \int_{\mathbf{0}}^{\boldsymbol{L}} R 2\pi l dl = \pi D \left(\frac{F}{4D} \right)^2 L^4 \left(\frac{2a}{P_{edge}} \right)^2 \qquad \text{EQ 3.5}$$

We can now solve for the fraction of terraces that have nucleated out second layers, *f*, given the that the island growth rate is $L^2 = Fa^2 L_{m1}^2 t$. Here L_{m1} is the spacing between nucleated terraces of the first monolayer.

$$\frac{df}{dt} = R'(1-f) \rightarrow f = 1 - \exp\left[- \left({}^{L}/_{L_c} \right)^6 \right] \qquad \text{EQ 3.6}$$

From this we get the critical island size, L_c, for which a second atomic will nucleate on top of the existing terrace.

$$L_c = \left[\frac{12L_{m1}^2}{\pi}\left(\frac{4D}{F}\right)\left(\frac{2}{P_{edge}}\right)^{-2}\right]^{1/6} \qquad \text{EQ (3.7) [12]}$$

If $L_c > L_{m1}$, then the first monolayer of atoms will grow and coalesce before the second layer nucleates out and there will be layer-by-layer deposition. If $L_c < L_{m1}$, then new terraces will nucleate on top of the existing ones and 3-D island formation will occur. Plugging typical numbers for deposition into EQ 3.7 estimates critical island sizes of 10-100 nm.

3.2.2 Effects of Mediators on Electrochemical Thin Film Growth

Mediating monolayers can be used to significantly change the structural development of a growing thin film. The layer acts as a barrier between adatoms and the bulk deposition surface. Surfactant monolayers have been studied extensively in ultra-high vacuum (UHV) systems as mediators [12-18]. In these systems an element is added that sits on top of the deposition surface and there is a net flux of a different element that form a film between the substrate and the surfactant layer. The surfactant is thermodynamically driven to the surface and floats on top of the bulk film. Mediated growth is able to change the diffusivity, nucleation density, and surface energies such that films that would typically grow in V-W or S-K growth modes can grow in a layer by layer fashion and has been demonstrated in these UHV systems. Additionally, the mediating layer may influence the Schwoebel barrier. Amongst the UHV systems creation of a high density of 2-D nuclei is attributed to causing layer-by-layer growth.

Mediated thin film growth during electrodeposition presents a novel and unique means of applying these UHV results in other systems. Underpotential deposition (UPD) of metal monolayers provides an easy means of controlling mediation during deposition of a metal. As discussed in Chapter 2, UPD behavior results from surface energy driving forces allowing for deposition of single or multiple monolayers of an element being deposited onto the surface of another material [19, 21]. These monolayers can parallel the surfactants used in UHV systems [19-29]. Thus UPD layers can be used as a means of directly manipulating growth kinetics of a depositing film [3, 4, 20]. In these systems,

the metal to be deposited is not the UPD metal, M, but rather an electrochemically more noble metal, N. The metals and electrolytes are chosen carefully such that M has UPD behavior on the surface of N and that the UPD peak of M is negative relative to the bulk deposition voltage of N. This allows for a unique deposition system where the metal N can be deposited in bulk while metal M is only stable as the surface of N. The percent coverage is controlled by applying a particular voltage relative to the UPD peak. The metal M is only thermodynamically stable at the surface of N, not as a bulk component, at the given voltage so it "floats" as a surfactant above the surface and does not alloy into the film. This system allows for direct control of a barrier layer between the bulk film and the depositing adatoms and thus a unique means of manipulating the kinetics of deposition. Two simple schemes can be constructed to use UPD monolayers to mediated deposition. One can hold a constant coverage percentage of metal M on N during deposition of N, which will be referred to as Surfactant Mediated Growth (SMG) [4], or oscillate the coverage percentage during deposition, which will be referred to as Defect Mediated Growth (DMG) [3]. When stripping the UPD monolayer in DMG systems we expect to create a large density of nuclei and attachment sites at the receding layer exposes small clusters of adatoms that interchanged with the UPD layer. In holding a particular coverage of the UPD monolayer in SMG systems we expect the exposed edges of the UPD monolayer to act as attachment sites to increase the nucleation rate and density. By increasing the density of 2-D nucleated islands, the films should be able to grow and coalesce in a layer-by-layer fashion.

3.3 Experimental Methods

The chemical system presented here uses Ag as the deposition material and Pb as the mediating material. Pb has well documented UPD monolayer behavior on Ag (111) [19,21]. The Ag-Pb Binary Phase diagram also shows no solubility of Pb in Ag at room temperature (Figure 6). This means that Ag will deposit as a pure elemental film and not as a Pb alloy. This is important as alloying means the activity of the atoms in the solid will not equal 1 and will change the Nernst potential of the system. Pb also has a standard electrode potential (SEP) of -0.13 V relative to a standard hydrogen electrode while Ag has an SEP of +0.8 V. The lead UPD will be at potentials slightly higher than -0.13 V however this will still be far from the Ag deposition potential. This means that the UPD coverage can be adjusted freely without affecting the deposition rate of the Ag atoms and without any bulk deposition of Pb. Lead Mediated growth of Silver therefore works well as a model system for this study. This system also parallels the single crystal work done by Sieradzki et al [3,4].

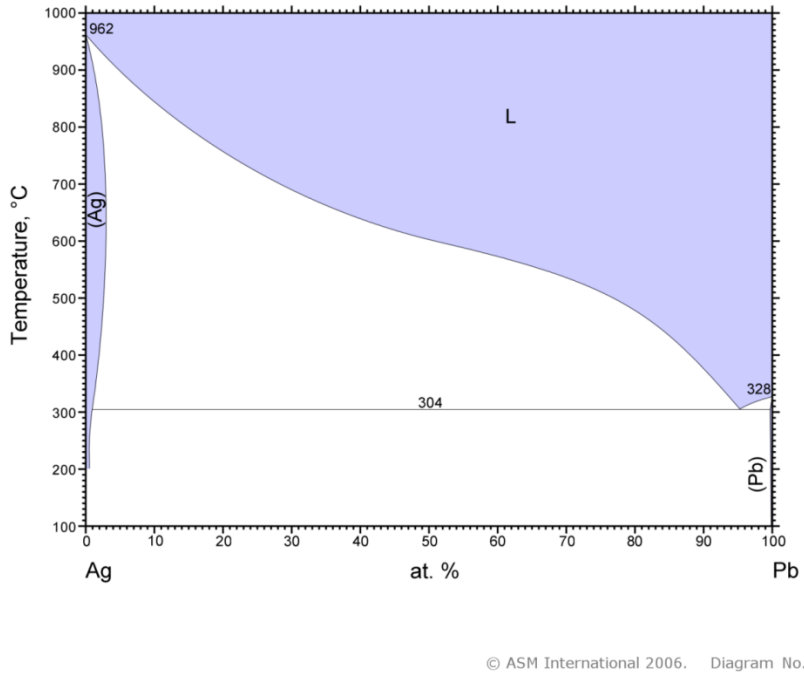

Figure 6: Silver-Lead Phase Diagram shows that there is no miscibility of lead into silver at room temperature. This is important as solubility of lead into silver would adjust the Nernst Potential by changing the activity of the element in the bulk solid making it difficult to ensure the final metallic film is lead free. Solubility of Pb into Ag would also result in a shift in the surface energy which could subsequently disrupt the UPD behavior.

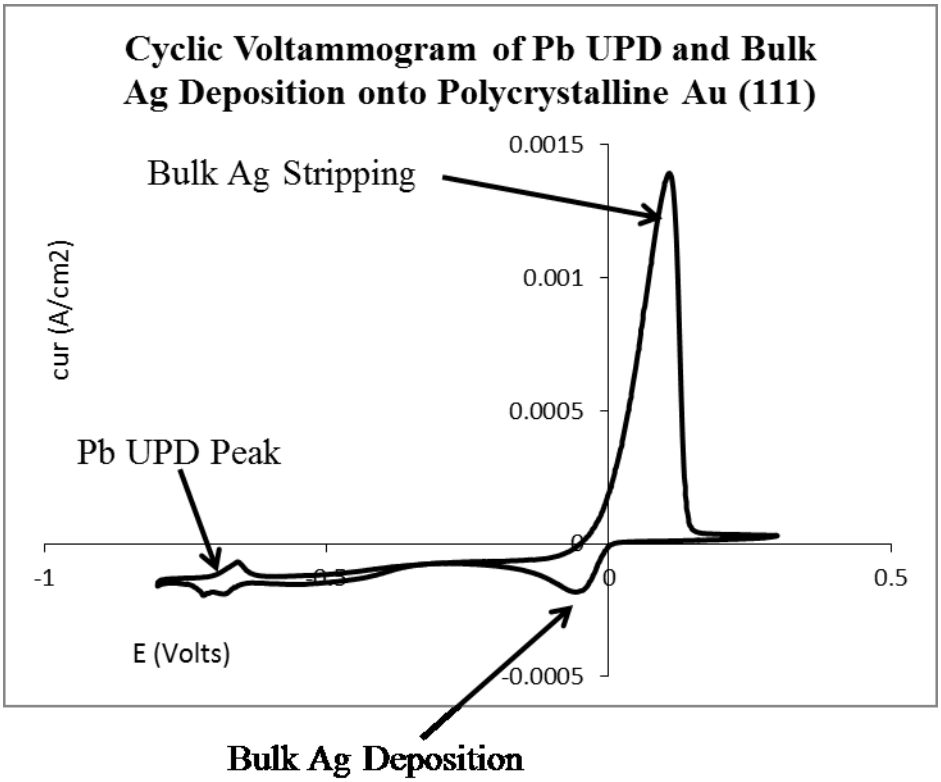

Figure 7: Cyclic Voltammogram of the mediated growth electrodeposition system using an Au (111) working electrode, a Pt foil counter electrode, and an Ag wire reference electrode, and an Ag-Pb electrolyte solution. The large set of peaks close to the origin is linked with bulk deposition of the noble metal, Ag. The small set of peaks at a voltage well negative of the Ag peaks (-0.7 V) are due to the UPD deposition of a Pb monolayer onto the Ag surface. The relative coverage of Pb on Ag is a function of the total charge passed under the UPD peak. This coverage can be controlled while maintaining a constant Ag deposition rate, which is diffusion limited at the relevant applied voltages.

Chapter 3: Effects of Pb Mediation on Ag Electrodeposited Films

For standard (mediation free) depositions of Ag onto Au substrates, a solution of 0.1 M $HClO_4$ and $5x10^{-4}$ M $AgClO_4$ was prepared. DMG and SMG experiments were run using an electrolyte of 0.1 M $HClO_4$, $5x10^{-4}$ M $AgClO_4$, and 0.01 M $PbClO_4$. The PbClO4 is used to supply the Pb ions to form a UPD monolayer during mediated deposition. All depositions reported here used Au (111) substrates as the working electrodes, a platinum foil as the counter, and a silver wire as the reference. Figure 7 shows a cyclic voltammogram of the electrolyte used for mediated deposition. By using a silver wire in the solution as a reference, the measured potentials are zeroed about the Nernst potential of Ag. That is any positive voltage relative to the reference will result in stripping of the Ag film while any negative voltage relative to the reference will result in Ag deposition. Standard Ag deposition was run at -0.68 V, these unmediated films serve as a control in these experiments. SMG experiments were run under potentiastatic conditions at voltages ranging from -0.5 V and -0.75 V which correspond to Pb monolayer coverage ranges from 0-100% on the Ag surface. Percent coverage is calculated as the ratio of the area under the UPD peak through a particular voltage to the area of the total UPD peak. Application of -0.68V in the solution containing Pb corresponds to 80% Pb coverage surfactant mediated growth. DMG was run by cycling the applied voltage between -0.75 and -0.1 V at a rate of 3 V/s the cycle frequency is approximately 2 Hz. These voltages correspond to 100% and 0% Pb monolayer coverage (see Figure 7). All experiments were run at voltages in the diffusion limited regime of

bulk Ag deposition so the current and flux of atoms to the surface was comparable between experiments. A schematic of the electrochemical cell used is shown in Figure 8.

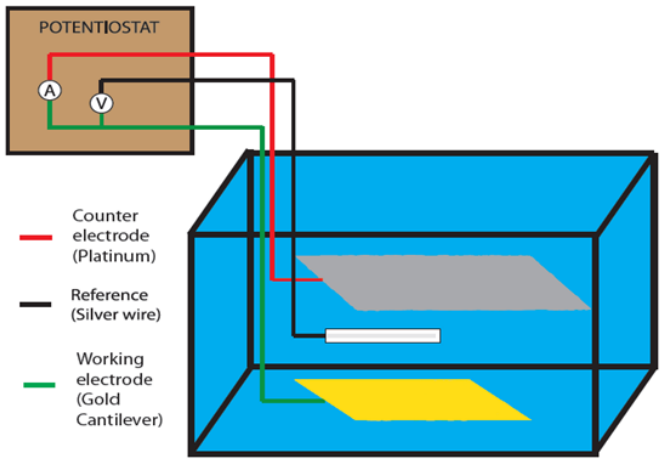

Figure 8: Schematic of Electrochemical Cell used for Pb Mediated Deposition of Ag Films. The bottom of the container is a quartz glass window to allow the optical system to measure changes in curvature of the working electrode

Polycrystalline Au (111) on glass substrates were prepared by evaporating Au onto glass cover slides. Au was selected as the substrate material because of its relative nobility. Ag epitaxially matches Au and is also known to undergo S-K growth due to kinetic limitations that may be overcome using mediation. It is well known that Au evaporated onto glass produces a polycrystalline film with a strong (111) texture parallel to the glass surface [22]. A (111) surface is required to get the appropriate UPD behavior of Pb on Au and Ag. A 5nm thick overlayer of Cr for adhesion and a 200nm thick overlayer of Au were deposited onto 1 x 5cm micro cover glasses at a rate of ~ 1 Å/s

using an e-beam evaporator. The slides were then briefly flame annealed. XRD confirmed the (111) texture and AFM revealed the grain size of the Au film to be approximately 100nm.

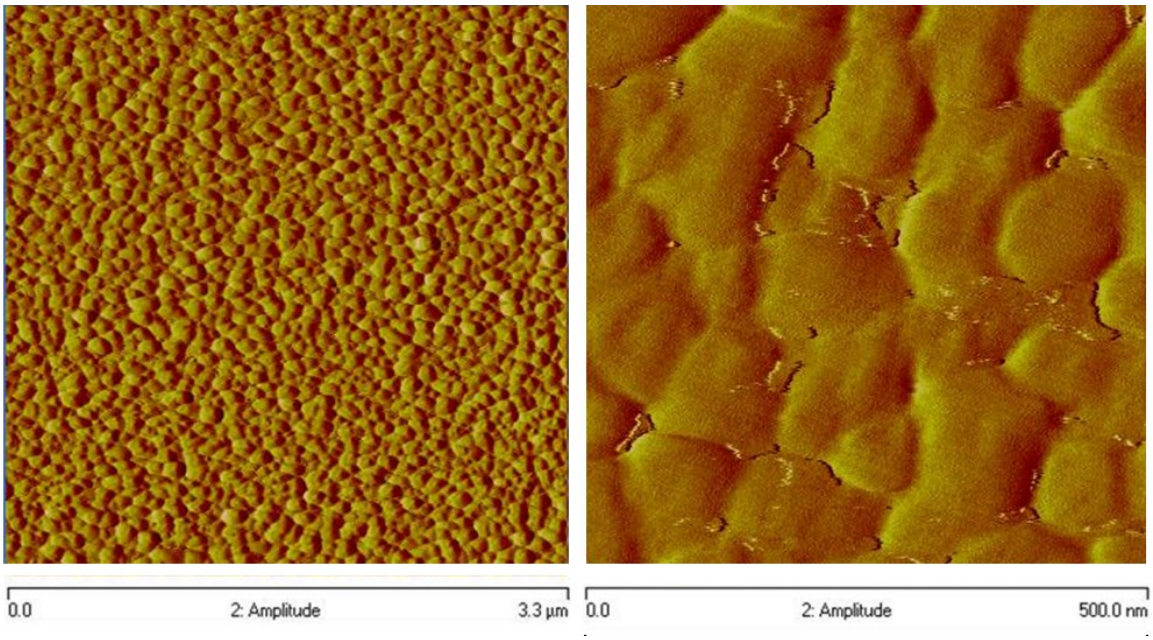

Figure 9: Tapping Amplitude Mode AFM Images of Au E-Beam Evaporated Surface After Flame Anneal. (Left) 3.3 x 3.3 micron image shows relatively uniform grain structure across the sample. (Right) 500 x 500 nanometer image shows relatively uniform surface with some small terrace formations at some grain boundaries

In situ curvature measurements of the Au (111) on glass working electrode were taken using a commercially available wafer curvature measurement system (KMOS, k-Space Technologies Inc.). Changes in curvature correspond to changes in the

stress*thickness of the film according to Stoney's equation (EQ 8). The instrument was calibrated using mass weights carefully placed at the end of the cantilever to correspond a particular deflection with a known load. It was also independently calibrated using fixed mirrors of known curvatures.

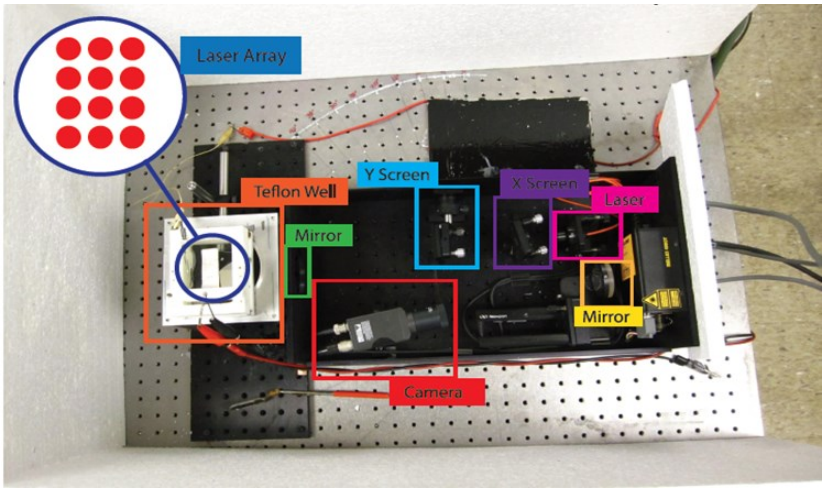

Figure 10: Schematic of K-MOS wafer curvature measurement setup. An array of parrallel laser spots are reflected off od the substrate and tracked electronically to determine the curvature changes of the substrate during deposition. The relative change in spot spacing is directly related to the focus length of the reflective substrate which is then used to calculate the curvature of the substrate.

$$\sigma h = \frac{E_S t_S^2 K}{6(1-v_S)} \qquad \text{EQ 8}$$

Here σ is the film stress, h is the film thickness, E_s is the substrate modulus, t_s is the substrate thickness, K is the curvature, and v_s is the Poisson's ratio of the substrate.

Using this setup, it is possible to measure stress development under a wide variety of different deposition conditions.

3.4 Results and Discussion

Figure 11 shows tapping mode AFM images of the as-deposited surfaces after deposition about 150 nm of deposition. The standard deposition Ag surface clearly shows the formation of many new 3-D island features that appear to be nucleating and growing on top of the underlying silver film. This is consistent with S-K growth that is expected for the unmediated system. The surfactant mediated films show a significant reduction in nucleating 3-D features. Films manufactured from 80% Pb coverage have very few 3-D features of note. Films deposited with 100% Pb coverage have a higher density of 3-D features than their 80% counterparts but still significantly less features than the unmediated film. SMG Ag films grown with 100% Pb also appeared to have these nuclei localized to the centers of existing grains unlike the features of unmediated control samples, which are randomly dispersed. AFM images of the DMG surface do not appear to show new nucleating island features but rather continued growth of the existing grain structure.

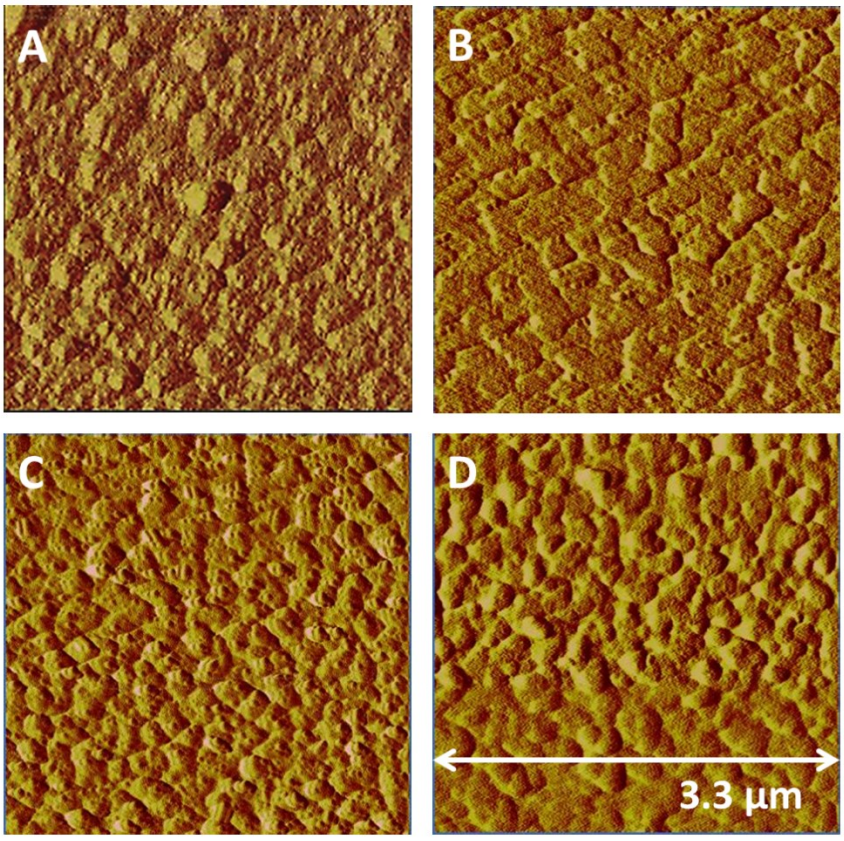

Figure 11: Tapping Mode AFM Images of Ag film surfaces: A) Surface of standard Ag electrodeposited film. Note there are many small 3D island features forming on top of the existing grain structure; B) Surface of Ag film deposited under surfactant mediation with 80% Pb monolayer coverage. Note there are significantly less small island sites compared to those formed during standard deposition; C) Surface of Ag film deposited under surfactant mediation with 100% Pb monolayer coverage. Note that while there are numerous small islands forming, they are sparse compared to those formed during standard deposition; D) Surface of Ag film deposited under defect mediation shows

uniform surface with few small nucleated islands forming but instead shows continued growth of existing grains.

Figure 12 shows the in situ stress*thickness versus thickness of standard Ag and SMG deposition. These results show a significant reduction in intrinsic stress with increasing Pb surfactant coverage during deposition. Because Au and Ag have nearly identical lattice parameters, we do not expect epitaxial stress to be significant and the measured stress should purely be due to intrinsic stress development. The standard Ag deposition had the highest (magnitude) measured stress, which is expected given its 3-D growth mode. The 80% Pb coverage showed a significant reduction in measured intrinsic stress, which seems to correspond with the observed changes in microstructure. While the reduction is stress corresponds somewhat to changes in microstructure, it is worth noting that 100% Pb coverage SMG samples had the smallest measured intrinsic stress among surfactant mediated samples despite the fact that it did have some 3-D island-like features on top of the surface. These island features appear to be small and centered on the underlying grains and may be acting as sources for ledges and kinks for lateral growth. Because the Pb layer completely covers the Ag surface in this deposition scheme, Ag ions that are reduced into adatoms need to migrate through the Pb barrier layer before incorporating into the bulk film. This requires an exchange of position with a Pb atom and would create a perturbation on the monolayer surface. This perturbation could be acting as a sink for other adatoms thus creating a particular spot on the grain where

adatoms attach and can migrate onto the grain surface. This may explain why the 100% Pb covered SMG samples have some consistent 3-D-like surface features but still have overall morphologies and stress behaviors like 2-D growth modes.

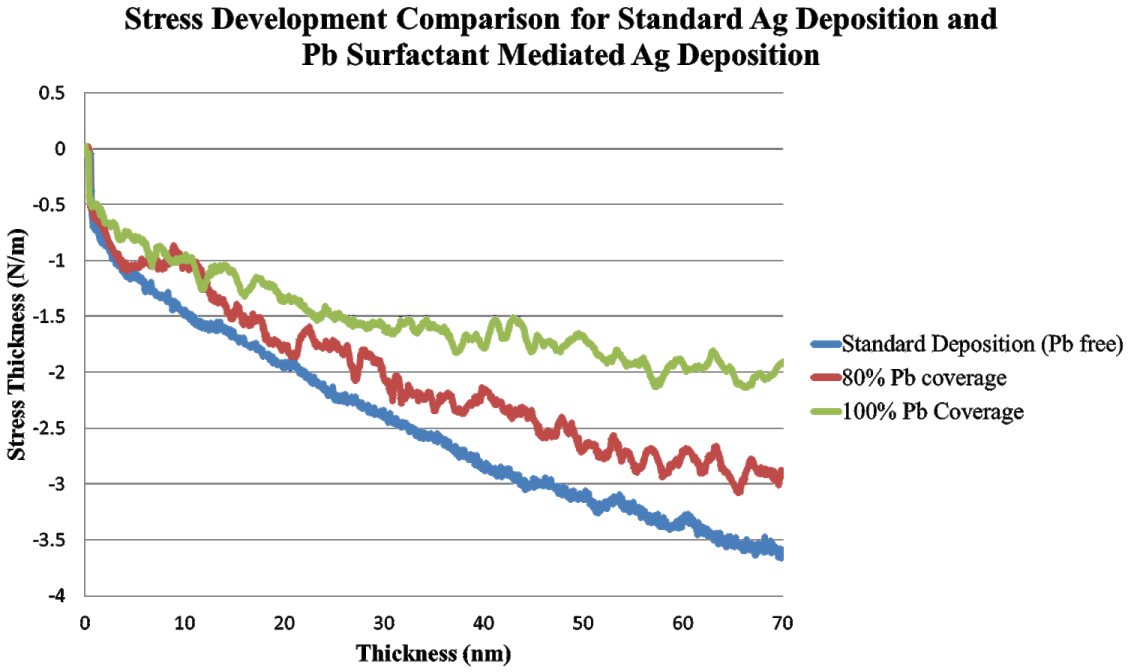

Figure 12: Stress*thickness (curvature) versus thickness of standard deposition, 80% Pb UPD coverage surfactant mediated deposition, and 100% Pb UPD coverage surfactant mediated deposition of Ag on a Au (111) polycrystalline surface. The introduction of a Pb mediating layer results in a lower film stress for a given ammount of Ag deposited.

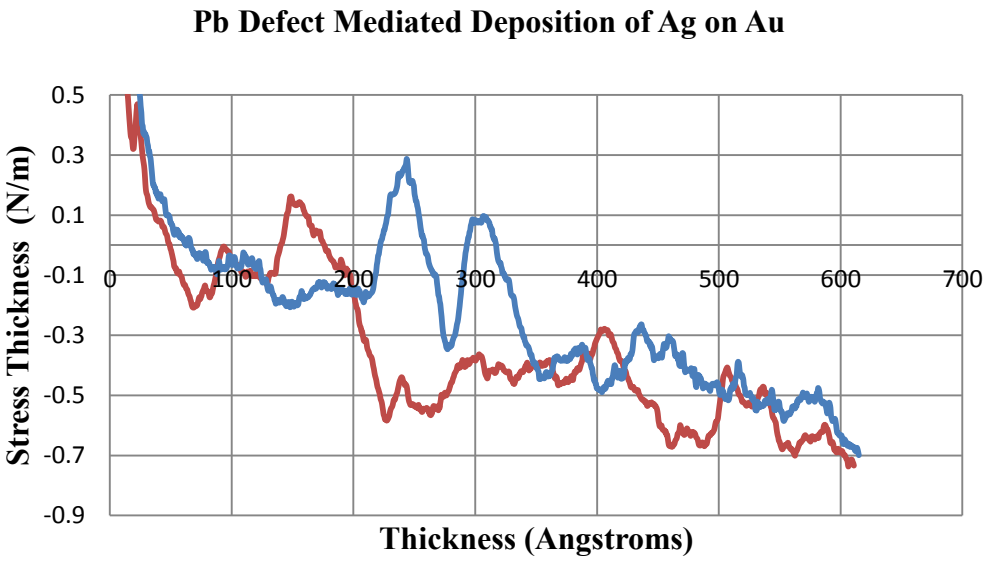

Figure 13: Stress*thickness (curvature) versus thickness of defect mediated deposition cycling Pb UPD coverage between 0 and 100%. Deposition conditions given resulted in a significant reduction in stress development as a function of Ag deposited compared to that of standard or surfactant mediated deposition. Two distinct runs are shown under the same deposition conditions; these measurements show very good agreement in trend despite significant noise during the experiment.

Defect Mediated Growth seems to result in a dramatic reduction in stress development with intrinsic stresses reduced by ~85% compared to those of standard deposition. Figure 13 shows in situ stress measurements of two Ag films grown under the 2Hz defect mediated growth scheme. Although the noise can be significant compared to the magnitude of the stress signal, depositions of multiple samples are in good agreement with each other. As observed in Figure 11, the DMG surfaces showed little signs of

nucleation of new surface features or grains but appeared to show continued growth of the underlying grain structure. Thus DMG can also be used to influence kinetics and microstructural development of the Ag films and lead to significant reductions in intrinsic stress development. Figure 14 compares the measured intrinsic stresses of the films deposited under the conditions reported here.

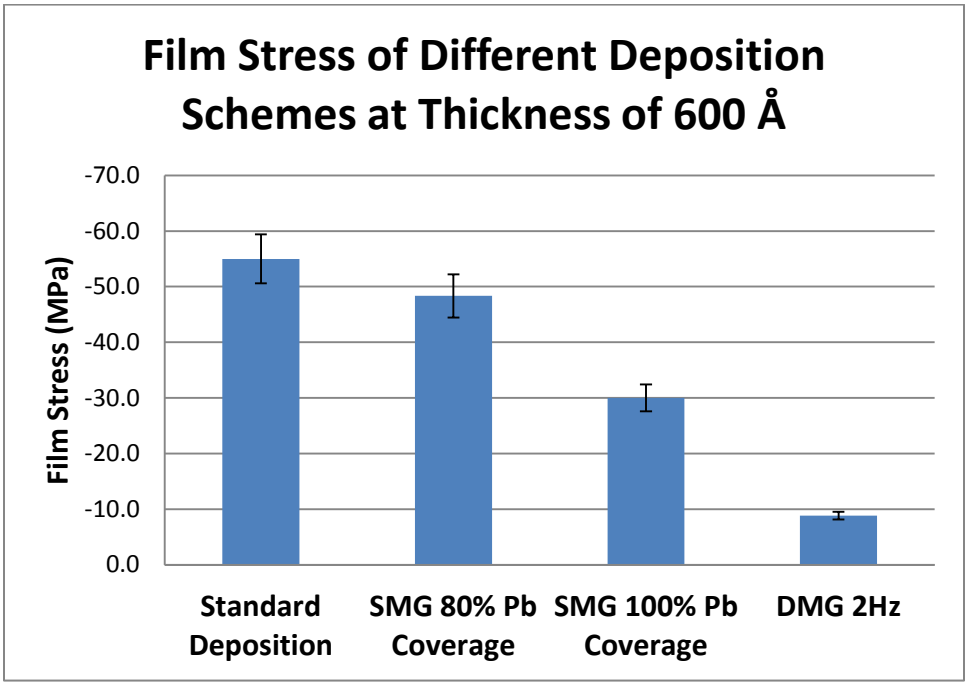

Figure 14: Comparison of Film Stresses for Different Deposition Schemes. Significant reductions in intrinsic stress were measured in the mediated electrodeposited materials. Defect mediated growth showed the most substantial stress reduction with compressive stresses of -8 MPa compared to those of standard deposition at -55 MPa.

3.5 Conclusions and Implications

Electrodeposition is a very important technique that is widely used in research and industry. While there are numerous benefits to electrodeposition, there are some serious drawbacks including small grain structures, rough surfaces, and high intrinsic stress developments. These drawbacks have been traditionally mitigated by use of additives in electrolytes; however the mechanisms in which these additives affect deposition are poorly understood. Use of additives is often purely empirically derived making design of electrochemical systems difficult. Mediation using UPD monolayers provides a controllable means of influencing kinetics and improving electrodeposition and can eliminate the need for ambiguous additives. By using UPD monolayers of a metal during deposition of a more noble metal, it is possible to induce terrace nucleation in the depositing metal in a manner that leads to layer-by-layer growth. Here we have demonstrated that defect and surfactant mediated growth can not only lead to large, smooth features but also result in significantly lower intrinsic stresses in Ag thin films. DMG and SMG grown Ag films showed substantially fewer 3-D surface features than unmediated Ag deposition; and measured stresses in unmediated films were several times those observed in mediated deposition. As a controllable means of improving the quality of the deposited film and substantially lowering the intrinsic film stress, UPD mediation represents a powerful alternative to other additives in electrochemical deposition.

Uses for this type of deposition system extend beyond the model silver system described here. This technique should extend to other electrochemical systems that still

meet the criterion of the mediating material being immiscible in and less noble than the deposition material. Applications of mediated electrochemical systems can then be extended to improve quality of other deposition materials. Residual and intrinsic stresses in deposited materials are an important driving force in failure of many thin film devices. These stresses can cause whisker formation, buckling, cracking, and delamination failure in films especially those that undergo thermo-mechanical cycling. Many of these problematic behaviors are also dependent on grain structure and texture so mediated deposition can serve to mitigate them through improvements on microstructure as well. Mediated electrochemical deposition of copper will be explored in Chapter 4 with microstructural changes and layer-by-layer growth linked to improvements in resistivity.

In addition to use in simple electroplated materials, mediated electrochemical deposition may also have potential applications in batteries and other cycled electrochemical cells. As discussed in Chapter 2, batteries are effectively two electrochemical half-cells linked through a semi-permeable membrane and an electrical load. Discharge of a battery during use is equivalent to electrochemical stripping of one of the electrodes. One of the major product lifetime issues in batteries is in recharging the electrode that was depleted during use. Recharging a battery is effectively electroplating a metal onto an electrode but this process can lead to non-uniform and even dendritic deformation that lead to inconsistencies and even catastrophic failure in batteries. If a simple scheme like surfactant or defect mediated growth could be implemented during recharging of the battery, it may be possible to obtain close to a pristine electrode after

each cycle. In fact many high energy density materials are avoided in commercial battery technology because their recharge microstructures lead to failure or physical hazards. Research into the use of mediated electrodeposition of energy storage materials could significantly improve the lifetime and reliability of battery technology, which has important social and commercial ramifications.

3.6 References

1. Kelly, J., et al. Leveling and Microstructural Effects of Additives for Copper Electrodeposition. *Journal of the Electrochemical Society* **146** (1999)
2. Andricacos, P.C., et al. Damascene Copper Electroplating for Chip Interconnections. *IBM Journal of Research & Development* **42,** 567-574 (1998)
3. Sieradzki, K., Brankovic, S.R. & Dimitrov, N. Electrochemical Defect-Mediated Thin-Film Growth. *Science* **284**, 138-141 (1999).
4. Brankovic, S., Dimitrov, N. & Sieradzki, K. Surfactant mediated electrochemical deposition of Ag on Au (111). *Electrochemical and Solid-State Letters* **2**, 443-445 (1999).
5. Floro, J., Chason, E. & Cammarata, R. Physical Origins of Intrinsic Stresses in Volmer – Weber Thin Films. *MRS Bulletin* 19-25 (2002)
6. Nix, W.D. *Mechanical Properties of Thin Films*. *Class Notes* (2005).
7. Seshan, K. Handbook of Thin-Film Deposition Process and Techniques: Principles, Methods, Equipment and Applications (2nd edition, 2002).
8. Thompson, C.V. Grain Growth in Thin Films. *Annu. Rev. Mater. Sci* **20**, 245-268 (1990)
9. Thompson, C.V. Structure Evolution During Processing of Polycrystalline Films. *Annu. Rev. Mater. Sci* **30**, 159-190 (2000)
10. Schwoebel, R., Shipsey E. Step Motion on Crystal Surfaces. *Journal of Applied Physics*. **37** 3682-3686 (1966)

Chapter 3: Effects of Pb Mediation on Ag Electrodeposited Films

11. Zhang, Z., et al. Atomistic Processes in the Early Stages of Thin-Film Growth. *Science* **276** (1997)

12. Tersoff, J., et al. Critical Island Size for Layer-by-Layer Growth. *Physical Review Letters* **72** (1994)

13. Liu, B-G., et al. Two-Dimensional Pattern Formation in Surfactant-Mediated Epitaxial Growth. *Physical Review Letters* **83,** 1195-1198 (1999)

14. Copel, M., Reuter, M. & Kaxiras, E. Surfactants in epitaxial growth. *Physical review letters* **63**, 632-635 (1989).

15. Rosenfeld, G., Servaty, R., Teichert, C., Poelsema, B. & Cosma, G. Layer-by-layer Hrowth of Ag on Ag(111) Induced by Enhanced Nucleation: A Model Study for Surfactant-Mediated Growth. *Physical Review Letters* **71**, 895-898 (1993).

16. Hoegen, M.H.-von, Pook, M., Falou, A.A., Muller, B.H. & Henzler, M. The interplay of surface morphology and strain relief in surfactant mediated growth of Ge on Si (111). *Surface science* **284**, 53-66 (1993).

17. Markov, I. Influence of surface active species on kinetics of epitaxial nucleation and growth. *Materials Chemistry and Physics* **49**, 93-104 (1997).

18. Hwang, I.-S., Chang, T.-C. & Tsong, T. Exchange-Barrier Effects on Nucleation and Growth of Surfactant-Mediated Epitaxy. *Physical Review Letters* **80**, 4229-4232 (1998).

19. Kolb, D., Przasnyski, M. & Gerischer, H. Underpotential deposition of metals and work function differences. *Journal of Electroanalytical Chemistry and Interfacial Electrochemistry* **54**, 25–38 (1974).

20. Hwang, S., Oh, I. & Kwak, J. Electrodeposition of epitaxial Cu(111) thin films on Au(111) using defect-mediated growth. *Journal of the American Chemical Society* **123**, 7176-7 (2001).

21. Bewick, A. & Thomas, B. Optical and Electrochemical Studies of the Under-Potential Deposition of Metals Part III. Lead Deposition on Silver Single Crystals. *Journal of Electroanalytical Chemistry* **84**, 127-140 (1977).

22. Golan, Y., Margulis, L. & Matlis, S. Vacuum-Deposited Gold Films. *Journal of The* **264**, 312-326 (1995).

23. Hachiya, T., Honbo, H. & Kingo, I. Detailed underpotential deposition of copper on gold (III) in aqueous solutions. *Journal of Electroanalytical Chemistry* **315**, 275-291 (1991).

24. Brisard, G.M., Zenati, E., Gasteiger, H.A., Markovie, N.M. & Ross, P.N. Underpotential Deposition of Lead on Copper (111): A Study Using a Single-Crystal Rotating Ring Disk Electrode and ex Situ Low-Energy Electron Diffraction and Auger Electron Spectroscopy. *Langmuir* 2221-2230 (1995).

25. Chu, Y.S., Robinson, I.K. & Gewirth, A.A. Properties of an electrochemically deposited Pb monolayer on Cu (111). *Physical Review B* **55**, 7945-7954 (1997).

Chapter 3: Effects of Pb Mediation on Ag Electrodeposited Films

26. Herrero, E., Buller, L.J. & Abruña, H.D. Underpotential deposition at single crystal surfaces of Au, Pt, Ag and other materials. *Chemical reviews* **101**, 1897-930 (2001).

27. Zheng, S.H. *et al.* Study of Bi UPD structures on Au (100) using in situ surface X-ray scattering. *Journal of Electroanalytical Chemistry* **649**, 189-197 (2010).

28. Shin, J.W., Bertocci, U. & Stafford, G.R. Underpotential Deposition of Tl on (111) - Textured Au : In Situ Stress and Nanogravimetric Measurements. *Society* 17621-17628 (2010).

29. Gokcen, D., Bae, S.-E. & Brankovic, S.R. Reaction kinetics of metal deposition via surface limited red-ox replacement of underpotentially deposited metal monolayers. *Electrochimica Acta* **56**, 5545-5553 (2011)

Chapter 4: Mediated Deposition of Copper Electrodeposited Thin Films

4.1 Introduction

In Chapter 3 we discussed in detail the kinetic processing control achievable using mediated electrochemical growth in a model Ag system. We also showed that mediated can affect the growth kinetics of the deposition system and lead to significant changes in the structural development and stress evolution of the resulting films. Ag serves as an ideal model system because it is electrochemically noble and Pb UPD monolayers on Ag have been extensively studied in the past. However, in order to prove this kinetic-structural behavior is a fundamental response to mediation, it is necessary to demonstrate this process in other electroplating systems. It is also beneficial to show this type of system is applicable to less noble and more industry relevant metallic films.

Copper is one of the most critical electrodeposited materials in industry. Because of its low resistivity and relative abundance, copper is used extensively for interconnects in integrated circuits [1,2]. While Cu interconnects show improvement in performance and processing compared to their Al predecessors, resistivity and electromigration in Cu lines still limit the performance and lifetime of these devices. Migration is particularly an issue at surfaces and grain boundaries, so we expect this problem to worsen as smaller device scales lead to larger surface area to volume ratios [3-6]. Thus it is vital to improve the quality of Cu in order to sustain continued reduction in scale and increase performance and lifetime of Cu interconnects.

Chapter 4: Mediated Deposition of Copper Electrodeposited Thin Films

Most Cu interconnects are grown electrochemically as electrodeposition provides a means of depositing large amounts of material over complex geometries and is easily scalable. However, electroplating generally results in small grain sizes, rough surfaces, and large stress developments during deposition; this leads to increased resistivity and poor migration properties. Chemical additives are typically used in electrolytes in order to mitigate these problems [1,2]. Unfortunately these additives are poorly understood and highly dependent on solution concentration. Often several additives must be used in tandem to try and manufacture a high quality film and the relative concentrations of additives can have significant impact on the microstructure of the film. Their effects are complex and empirically derived making it difficult to design electrolyte solutions and making progress in improving deposition tedious and slow.

Given the current processing issues with electrodeposited Cu, it is a key system of interest for application of defect and surfactant mediated electrochemical growth. This chapter will detail work investigating defect and surfactant mediation of electrodeposited copper thin films using a Pb UPD mediating monolayer. Changes in microstructure and correlated changes in resistivity show significant improvements in processing and properties of Cu films grown under mediation.

4.2 Background

As discussed at length in Chapter 3, thin film deposition can be categorized under three different growth modes. Frank-Vander Merwe growth is a layer-by-layer process where complete wetting occurs. Volmer-Weber and Stranski-Krastanov growth are processes that involve 3-D island nucleation, growth, and coalescence. One means of inducing layer-by-layer growth during deposition is to introduce a high-density of nucleation sites that will allow for terraces to grow and coalesce into a monolayer before new monolayers and terraces form 3-D structures. Mediation using surfactants can be used to create high-density nucleation and thus promote 2-D layer-by-layer growth. In electrochemical systems, Underpotential deposition of monolayers of a less noble metal can be used to mediate deposition of a more noble metal. Holding a constant UPD coverage is referred to as Surfactant Mediated Growth. Oscillating the coverage during deposition is referred to as Defect Mediated Growth.

Given that mediated deposition can result in significant changes in microstructure and surface roughness, it is expected that there will also be correlated changes in material properties. Of specific interest for copper electroplated materials are impacts of this microstructural change on resistivity. The resistivity is important to the function of copper interconnects as increases in resistivity lead to signal loss and heat generation in devices. Thus lowering the resistivity of the plated material will improve performance and energy efficiency in devices using Cu interconnects.

Chapter 4: Mediated Deposition of Copper Electrodeposited Thin Films

Analytical models for changes in resistivity due to surface roughness and grain size have previously been established by Fuchs & Sondheimer and Mayadas & Shatzkes respectively.

The surface scattering contribution to resistivity, ρ_s, can be written as:

$$\frac{\rho_0}{\rho_s} = k\left[\frac{3(1-p)}{2k^2}\int_1^\infty \left(\frac{1}{t^3}-\frac{1}{t^5}\right)\frac{1-e^{-kt}}{1-pe^{-kt}}dt\right]^{-1} \qquad \text{EQ 4.1 [8,9]}$$

where ρ_0 is the bulk resistivity, t is the film thickness, k is the ratio of the film thickness to the electron mean free path (λ_0), and p is a non-dimensional scattering factor. The scattering factor accounts for the surface roughness of the where a mirror finish would have a value of 1, leading to a ρ_s of 0. Increasing the surface roughness will increase the effective scattering and p will approach 0.

The grain boundary scattering contribution to resistivity, ρ_g, can be written as:

$$\frac{\rho_g}{\rho_0} = \left[1-\frac{2}{3}\alpha+3\alpha^2-3\alpha^3\ln\left(1+\frac{1}{\alpha}\right)\right] \quad ,\alpha = \frac{\lambda_0}{d}\left(\frac{p_g}{1-p_g}\right) \qquad \text{EQ 4.2 [7,9]}$$

where d is the grain size and p_g is the grain boundary scattering factor. For copper ρ_0 is 1.7 μΩ-cm and the reported p_g is for bulk copper is 0.24. From this model with expect the resistivity to increase significantly with decreases in grain sizes below ~50nm.

From these analytical solutions we find that resistivity of a film can be highly dependent on the microstructure of the metal. If grain size and surface roughness can be improved by means of mediation, we can expect corresponding improvements in the resistivity of the deposited films.

4.3 Experimental:

Substrates for depositions reported here were provided by Dr. G. Fritz, IBM TJ Watson. The substrates consisted of pure Si wafers sputter coated with 2 nm TaN, 2 nm Ta, and 3 nm Cu seed. TaN and Ta layers were deposited to prevent diffusion of Cu into the underlying Si. The Cu seed layer is deposited to prevent oxidation of Ta on exposure to atmosphere and to act as a metallization layer to enable electrodeposition. A 2 μm film of photoresist was coated onto the substrate to protect it from surface wear and oxidation. This resist was removed from samples using an acetone bath prior to any experimentation. These blanket substrates parallel those used in state of the art integrated circuit manufacturing.

Electrical contact was made by adhering 3M Copper Conductive Tape to the clean Cu surface of the previously described substrates. Two parallel lines of tape were spaced approximately 0.5 cm apart. The copper tape was encapsulated in 3M Model 470 Electroplater's Tape to ensure the electrical contact would not be exposed to the electrochemical solution and deposition could only occur at the desired working surface. The spacing between contacts was chosen to ensure that the internal resistance of the substrate metallization layer was substantially lower that the resistance of the solution. This guarantees that the rate limiting step is the reduction of Cu ions and not the supply of electrons to the deposition surface. This allows for uniform deposition rates across the width of the working electrode.

Chapter 4: Mediated Deposition of Copper Electrodeposited Thin Films

Pb was chosen as the mediating material because it is less electrochemically noble than Cu, it has no solubility in bulk Cu, and it has known UPD behavior on Cu [12-15]. Figure 15 shows a phase diagram of Cu-Pb showing no solubility at room temperatures.

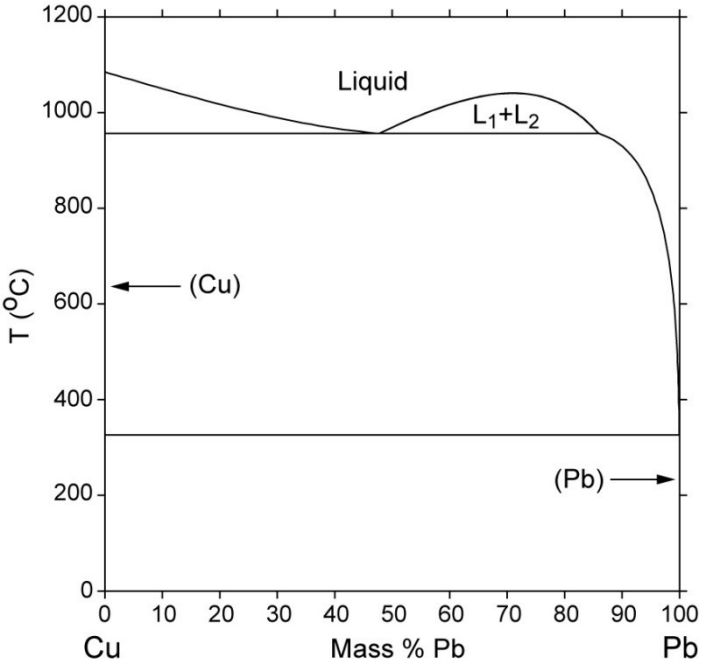

Figure 15: Copper-Lead Binary Phase Diagram shows that Pb is completely immiscible in solid Cu.

A solution of 0.01 M $Cu(ClO_4)_2$ and 0.01 M $Pb(ClO_4)_2$ in >17MΩ-cm water was used with a Cu plate counter electrode and Cu foil reference. The Cu reference electrode allows the system to be zeroed about the Nernst potential for Cu. The Cu counter electrode continuously supplies Cu ions to the solution to prevent changes in solution concentration during deposition. Figure 16 shows a Cyclic Voltammogram of this

solution system around the Pb UPD region of interest. Potentials positive of the Cu reference were avoided as this would strip the Cu including the substrate material.

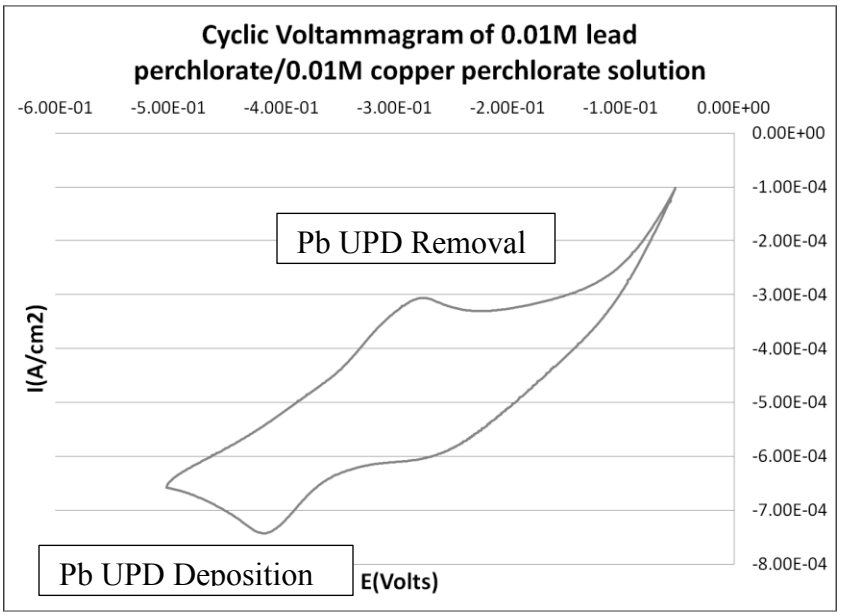

Figure 16: Cyclic Voltammogram of Pb-Cu Solution Versus Cu Foil Reference. The Cu deposition reaches a diffusion limited regime before deposition of the Pb UPD. There is some hysteresis in removing the Pb UPD layer, which has been reported previously [12-15]. For calculating the percentage of Pb coverage on the Cu film, the deposition peak is used. For Defect Mediated Growth upper potentials are used such that the Pb monolayer is completely stripped during each cycle.

Standard Cu deposition was run at a constant -0.3 V, which results in 0% Pb coverage of the depositing Cu. These unmediated films serve as a control in these experiments. SMG experiments were run under potentiastatic conditions at voltages

ranging from -0.42 V to -0.5 V which correspond to Pb monolayer coverage ranges from 40 to 100% on the surface. Percent coverage is calculated as the ratio of the area under the UPD deposition peak through a particular voltage to the area of the total UPD peak. DMG was run by cycling the applied voltage between -0.5 and -0.275 V at a rate of 3 V/s the cycle frequency is approximately 0.7 Hz. These voltages correspond to 100% and 0% Pb monolayer coverage (see Figure 16). All experiments were run at voltages in the diffusion limited regime of bulk Ag deposition so the current and flux of atoms to the surface was comparable between experiments.

4.4 Results and Discussion

Compositional analysis was performed on all films to ensure the resulting film was pure Cu using Energy-Dispersive X-ray Spectroscopy EDX. This is particularly important for applications of these films as the resistivity of Cu can significantly increase with trace amounts of contaminant metals. While most of the films showed no detectible traces of Pb in the film, materials deposited under 100% Pb coverage did show concentrations of Pb. Spectrum analysis determined the Pb atomic concentration to be approximately 2%. This is particularly high given there is no miscibility of Pb into Cu. Pb has been shown to be able to sit in the grain boundaries of Cu and the voltages applied for 100% mediation are close to the bulk Pb deposition potential so this may result in some kinetic trapping of Pb in the Cu film.

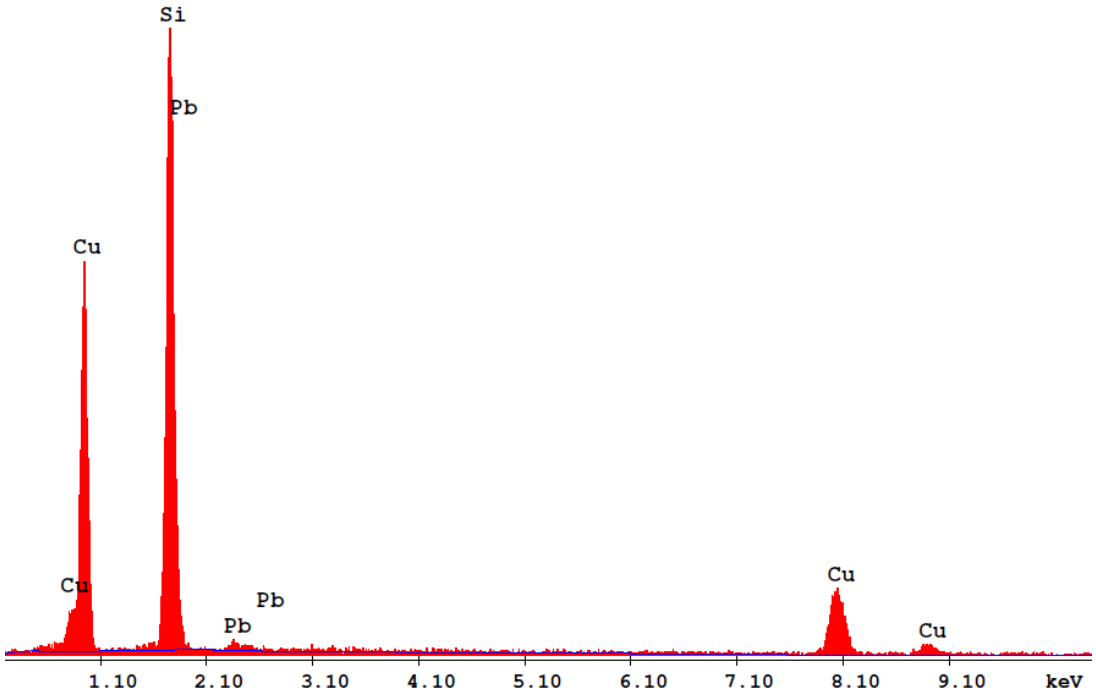

Figure 17: X-ray Spectrum of Cu SMG sample grown with 100% Pb Coverage. Trace amounts of Pb were detected in these films. No Pb was detected in films manufactured under any of the other deposition conditions presented for elemental copper.

Tapping mode AFM images were taken of the as deposited Cu surfaces to observe the microstructure as shown in Figures 4-6. These images clearly show the terrace nucleation and stacking model growth described in Chapter 3. Figure 18 shows the surface of the unmediated control sample. In these images terraces are shown growing out from the grain boundaries which serve as a nucleation site. These terraces are growing towards the center of each grain but seem to be kinetically pinned at a fixed size. The steps shown in Figure 18 are several Å high meaning they are stacks of several

atomic layers on top of each other. The overall sample has a wide distribution of feature sizes with many new grains nucleating on top of the film.

In contrast to the results seen in the control sample, the mediated deposition samples depicted in Figure 19 and Figure 20 show layer-by-layer type growth. In these samples many 2-D atomic terraces can be seen on top of the existing surface. The step heights at the edges of these terraces are single angstroms meaning they are atomic monolayers. The overall morphology shows a very consistent and uniformly dispersed grain size. These mediated films show enhanced 2-D nucleation which allows for coalescence of a monolayer of atoms at a time leading to layer-by-layer growth.

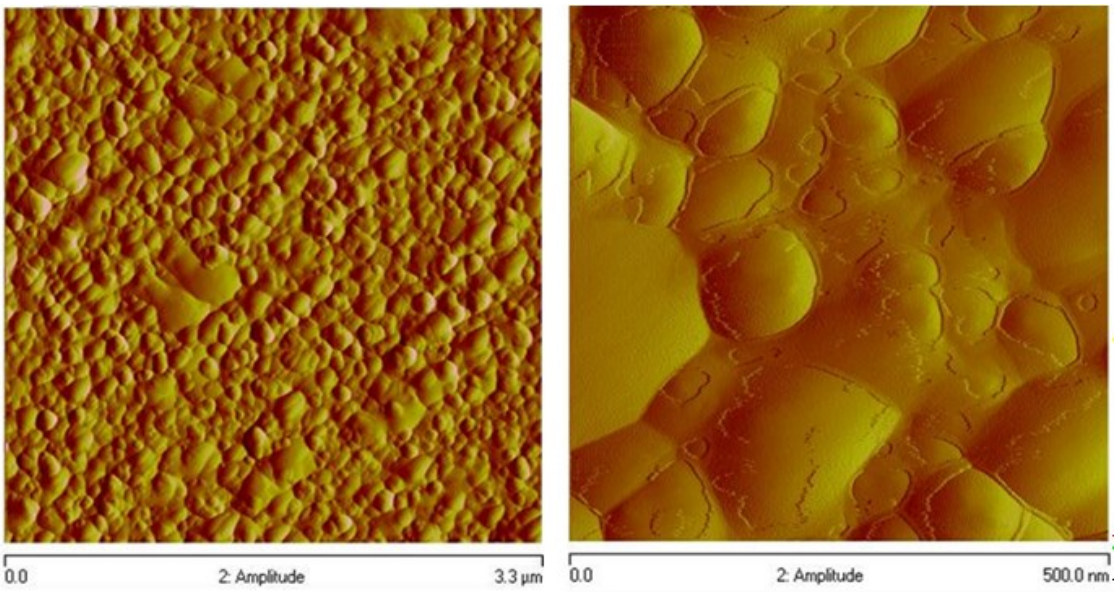

Figure 18: Tapping Mode Amplitude AFM Images of Control Copper Electrodeposited Sample (no Lead mediation). (Left) 3.3 x 3.3 micron image shows polycrystalline film with numerous small 3D islands. There is a large distribution of island sizes. (Right) 500 x 500 nanometer image of surface shows terrace and island formation on top of existing surface features. Nucleation of new terraces predominantly occurs at the grain boundaries. Step edges consistently have a positive change in height when moving from the center of the grain towards the grain boundary. Measured step heights are several angstroms high indicating stacking of several atomic terraces on top of each other. These features are consistent with a 3-D growth mode from 2-D terrace nucleation and stacking due to kinetic limitations.

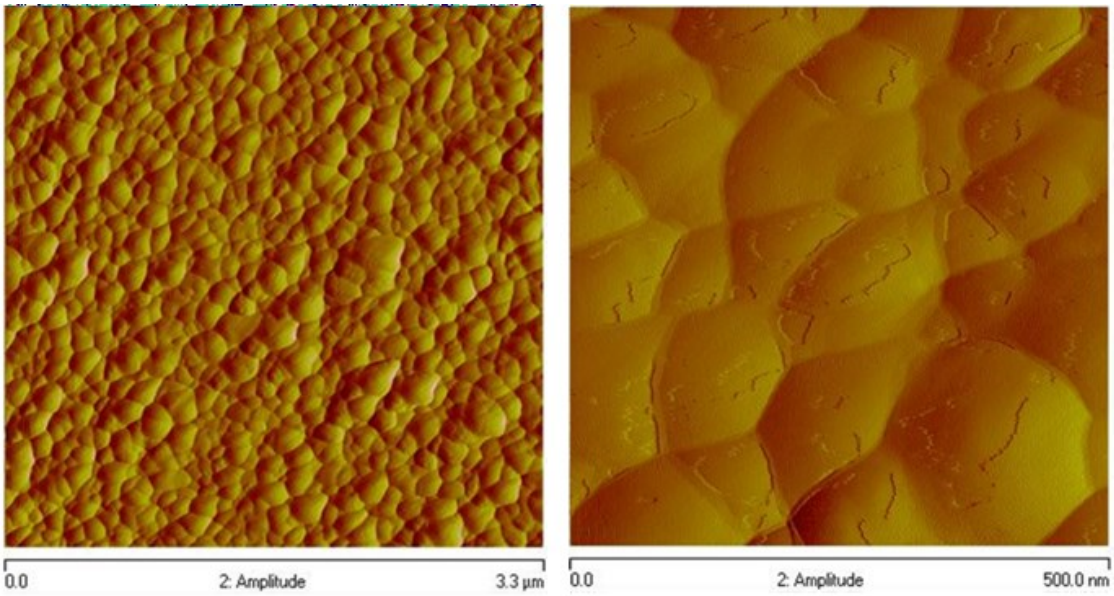

Figure 19: Tapping Mode Amplitude AFM Image of Surfactant Mediated Growth at 40% Pb Monolayer Coverage. (Left) 3.3 x 3.3 micron image shows polycrystalline film with relatively uniform growth of islands. (Right) 500 x 500 nanometer image of surface shows terrace and island formation on top of existing surface features. Nucleation of new terraces occurs at the grain boundaries and on the surface of the grain. Step edges randomly have a positive or negative change in height when moving from the center of the grain towards the grain boundary. Measured step heights are single angstroms high indicating single monolayer atomic terraces on top of the underlying grain. These features are consistent with 2-D terrace nucleation and growth in a layer-by-layer fashion. Grain size is ~100 nm.

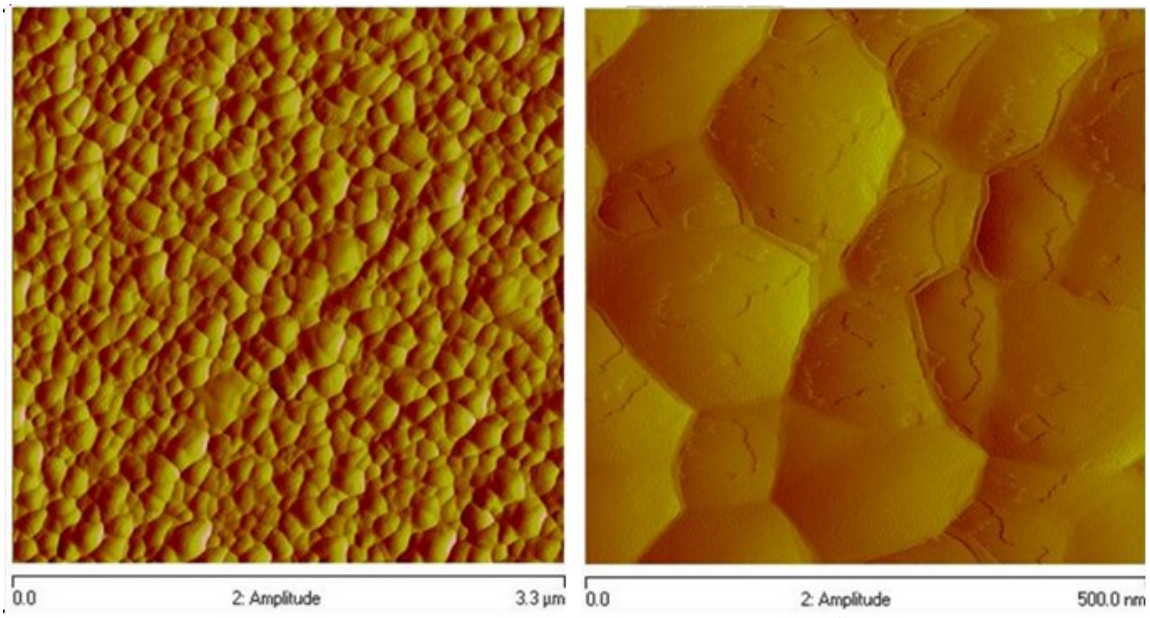

Figure 20: Tapping Mode Amplitude AFM Image of Defect Mediated Copper. (Left) 3.3 x 3.3 micron image shows polycrystalline film with relatively uniform growth of islands. (Right) 500 x 500 nanometer image of surface shows terrace and island formation on top of existing surface features. Nucleation of new terraces occurs at the grain boundaries and on the surface of the grain. Step edges randomly have a positive or negative change in height when moving from the center of the grain towards the grain boundary. Measured step heights are single angstroms high indicating single monolayer atomic terraces on top of the underlying grain. These features are consistent with 2-D terrace nucleation and growth in a layer-by-layer fashion. Grain size is ~120 nm.

2-point resistivity measurements were also taken for each film. Film thicknesses were measured using a profilometer. The standard, unmediated control sample had a measured resistivity of 4.3 ± 0.6 μΩ-cm. The SMG film at 40% constant coverage had a measured resistivity of 2.7 ± 0.4 μΩ-cm. The DMG film had a measured resistivity of 1.9 ± 0.3 μΩ-cm. Bulk Cu has a resistivity of 1.7 μΩ-cm so this DMG sample is approaching an ideal film resistivity. Decreases in resistivity are expected with increases in grain size and decreases in roughness according to Equations 4.1 and 4.2. This significant drop in resistivity, associated with the microstructural changes, is highly desirable in Cu electrodeposited of interconnects.

Table 1: Measured Resistivity of Copper Films

Deposition Conditions	Standard 0% Coverage	SMG 40%	SMG 100%	DMG	Bulk Copper
Resistivity μΩ-cm	4.3 ± 0.6	2.7 ± 0.4	12.1 ± 1.2	1.9 ± 0.3	1.7

The resistivity of the SMG film under 100% Pb coverage was significantly higher than the others because of the Pb contamination in these films.

4.5 Mediated Deposition of Dilute Cu-Fe Alloys

In addition to the deposition of elemental copper films, studies were conducted in a slightly modified electrochemical solution of 0.01 M $Cu(ClO_4)_2$, 0.01 M $Pb(ClO_4)_2$, and 0.002 M $Fe(ClO_4)_2$. Copper is the most noble of the three elements and will deposit preferentially over the iron added to the solution, however, there is also some limited room temperature miscibility of Fe in Cu. Due to this miscibility some Fe will deposit above the Nernst potential calculated for elemental deposition. Thus dilute amounts of Fe can be co-deposited into a Cu alloy. Standard and mediated depositions were run for this solution under the same conditions as for elemental Cu films. The microstructures of these films are shown in Figure 21. EDX compositional analysis showed equivalent chemistries for all the samples with approximately 98% Cu, 1.5% Fe, and 0.5% Pb. Pb was found in all samples in this system as the ternary Cu-Fe-Pb phase diagram allows for some solubility of Pb in Cu-Fe. Since the chemistries between samples are nominally the same, the structural differences are due solely to effects from mediation. These changes paralleled those found in the elemental films. Unmediated films showed rough, 3-D surfaces and high resistivities. Mediated films showed improvements in surface roughness with DMG alloy films also showing substantial drops in film resistivity.

Table 2: Measured Resistivities of Cu-Fe-Pb alloys

Deposition Conditions	Standard 0% Coverage	SMG 40%	DMG
Resistivity μΩ-cm	3150 ± 150	3100 ± 1000	610 ± 130

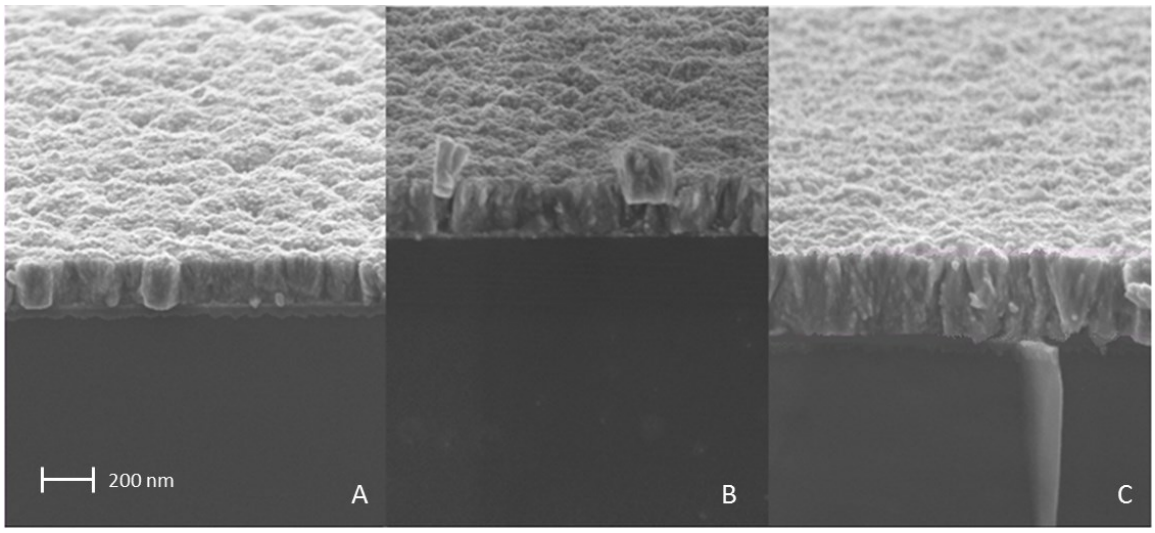

Figure 21: SEM images of cross sections of Cu-Fe-Pb films deposited onto Si substrates: A) Cu control film from standard (unmediated) deposition has rough surface with hills and valleys associated with Volmer Webber Growth: B) Cu from Surfactant Mediated Growth with 80% Pb coverage still has rough features associated with Volmer Webber Growth but is smoother than the control surface; C) Cu from Defect Mediated Growth has significantly smoother and flatter surface than the control sample. This implies a 2-D layer by layer growth mode.

4.6 Conclusions and Implications

Here we have demonstrated that defect and surfactant mediated growth can be applied to Cu electrodeposition. This demonstrates the viability of this technique outside of a model Ag system. DMG and SMG grown Cu films showed substantially fewer 3-D surface features than unmediated Cu deposition. AFM images show significant enhancement in 2-D terrace nucleation in the mediated deposition samples which results in 2-D layer-by-layer type growth. These mediated growth samples also show significant reduction in resistivity associated with the microstructural changes. UPD mediation represents a powerful alternative to other additives in electrochemical deposition of Copper. It is a tunable means of improving the quality of the deposited film and substantially lowering the film resistivity. Most elemental Copper films were Pb free meaning that Pb is contained to processing and would not appear in a final device.

This study on blanket copper films has significant implications for industrial technologies. Current Cu interconnects in integrated circuits are manufactured through complex electrodeposition and polishing techniques. The deposition solution requires several additives, whose effects are poorly understood, to improve the film's microstructural quality. These depositions also result in 3-D growth making geometric filling of patterned spaces difficult. Cu connects are intentionally overfilled and then back-etched in order to conform to circuit patterns. The use of mediators, instead of ambiguous additives, may allow for well controlled microstructures of interconnects. Additionally layer-by-layer growth may improve pattern filling and possibly eliminate

the need for overfill and back-etching. Finally the change in microstructure and lower resistivity may impact the electromigration and failure behavior of the deposited film.

Initial studies were also conducted on mediated deposition of Cu alloys. These alloys were shown to also have significant structural and electrical changes as a result of mediation. This means the use of mediators may be useful in microstructural control of deposited alloys as well.

References

1. Kelly, J., et al. Leveling and Microstructural Effects of Additives for Copper Electrodeposition. *Journal of the Electrochemical Society* **146** (1999)
2. Andricacos, P.C., et al. Damascene Copper Electroplating for Chip Interconnections. *IBM Journal of Research & Development* **42,** 567-574 (1998)
3. Ho, P.S. & Kwok, T. Electromigration in metals. *Reports on Progress in Physics* **52**, 301-346 (1989).
4. 23. Prasad, J.J.R. & Reddy, K.V. Electromigration in Thin Solid Films. *Thin Solid Films* **164**, 123-127 (1988).
5. 24. Lloyd, J.R. & Clement, J.J. Electromigration in copper conductors. *Thin Solid Films* **262**, 135-141 (1995).
6. 25. Hu, C.-K., Rosenberg, R. & Lee, K.Y. Electromigration path in Cu thin-film lines. *Applied Physics Letters* **74**, 2945 (1999).
7. Mayadas, A.F., Shatzkes, M. Electrical Resistivity Model for Polycrystalline Films:: The Case of Arbitrary Reflection at External Surfaces. *Phys. Review B* **1** (1970)
8. Fuchs, K. The Conductivity of Thin Metallic Films According to the Electron Theory of Metals. *Mathematical Proc. Of the Cambridge Phil. Soc.* **34** (1938)
9. Camacho, J. and Oliva, A. Surface and Grain Boundary Contributions in the Electric Resistivity of Metallic Nanofilms. *Thin Solid Films* **515** (2006)
10. Sieradzki, K., Brankovic, S.R. & Dimitrov, N. Electrochemical Defect-Mediated Thin-Film Growth. Science 284, 138-141 (1999).

11. Brankovic, S., Dimitrov, N. & Sieradzki, K. Surfactant mediated electrochemical deposition of Ag on Au (111). Electrochemical and Solid-State Letters 2, 443-445 (1999).
12. Brisard, G.M., Zenati, E., Gasteiger, H.A., Markovie, N.M. & Ross, P.N. Underpotential Deposition of Lead on Copper (111): A Study Using a Single-Crystal Rotating Ring Disk Electrode and ex Situ Low-Energy Electron Diffraction and Auger Electron Spectroscopy. Langmuir 2221-2230 (1995).
13. Chu, Y.S., Robinson, I.K. & Gewirth, A.A. Properties of an electrochemically deposited Pb monolayer on Cu(111). Physical Review B 55, 7945-7954 (1997).
14. Nasirpouri, F. On the electrodeposition mechanism of Pb on copper substrate from a perchlorate solution studied by electrochemical quartz crystal microbalance. Ionics 17, 331-337 (2011).
15. Hwang, S., Oh, I. & Kwak, J. Electrodeposition of epitaxial Cu (111) thin films on Au(111) using defect-mediated growth. Journal of the American Chemical Society 123, 7176-7 (2001).

Chapter 5: Nickel - Alumina Uniformly Dispersed and Hierarchical Composites

5.1 Introduction

While there is significant interest in studying the fundamental science behind electrochemical deposition, the driving force behind that interest is still to engineer a material appropriate for a given device. Though studying kinetic processes is beneficial for improving current technologies, designing and manufacturing new materials via electrodeposition is key in broadening the field and opening up new applications. Here we will discuss a novel means of manufacturing metal matrix-ceramic nanocomposites as well as the use of this technique to generate unique hierarchical composite systems and functionally graded materials.

Electrodeposition has continued to grow as an important industry tool not only for depositing traditional metal structures, but also for manufacturing more complex composite, oxide and semi-conducting thin films [1-6]. Nanocomposites and hierarchically ordered composite materials have grown as a topic of research interest over the past decade. Materials with these unique constructions lead to better strength to weight ratios, failure behavior, and other beneficial properties compared to those of traditional materials [7-9]. Hierarchical composite structures are specifically found in natural structural materials, which display superior mechanical properties to manufactured materials and often show significantly enhanced properties compared to those of their base components [7-9]. These materials have controlled composite structures at nanometer length scales as well as higher order structures ranging from

nanometer to 100 micron length scales. While maintaining these finely controlled microstructures and nanostructures, these materials are often produced at bulk size scales in nature. Simulations and analytical models of these structures predict that manufactured artificial hierarchical materials would also display superior properties compared to those produced by most current industry technologies [10-19]. Despite extensive research, limited progress has been made in actually manufacturing materials with these unique structures and properties. Much of the difficulty in manufacturing these hierarchical and composite structures has come in controlling them at both nanoscales and macroscopic length scales. While there are many refined techniques for creating nanostructures and processing bulk materials, generating an organized arrangement of these nanostructures in bulk quantities has proved challenging.

Electrochemical co-deposition provides a unique means of tackling many of the difficulties that have hindered the synthesis of these composite structures. Deposition rates can be finely tuned to nanometers/minute, but these same systems can also be robust enough to deposit at rates on the order of microns/minute. Additionally, total deposition thicknesses of the order of millimeters can be achieved. It has been shown in previous work that electrodeposition can also be used to create uniform metal-ceramic nanocomposite structures. By using a rotating disk electrode (RDE) system in an electrolyte solution that contains a suspension of ceramic nanoparticles, it is possible to imbed these particles into the metal matrix as the metal ions are being deposited [1-6]. This system allows for control of the oxide volume fractions of the metal - ceramic

nanocomposites as a function of rotation rate and deposition current per unit area. The ability to finely control nanoparticle incorporation and metal deposition at nanometer to millimeter length scales makes electrodeposition in an RDE system an ideal process for overcoming the challenges that have stifled the manufacturing of artificial hierarchical structures.

By varying the rotation rate of the RDE during electrodeposition we have been able to impose a controlled compositional variation of the nanocomposite through the thickness of the deposited material [20]. This method is capable of taking the primary nanocomposite structure and creating higher order structures from them. These secondary structures can have micron to millimeter length scales and are true artificial hierarchical structures with ordering along the thickness of the material. Although this RDE method can overcome microstructural control issues and manufacture robust nanocomposite materials, it is also quite limited in deposition area. Working areas are limited to $< \sim 0.2$ cm^2 as larger rotating electrodes lead to non-uniform fluid dynamics and reaction kinetics across the deposition surface. We have developed new composite deposition system that has similar microstructural control to an RDE system but can be scaled to large areas.

Here we will explore the manufacturing capabilities of these methods and investigations into the hardness, tensile strength, and other mechanical properties of these uniform and high order composite structures. Specific attention is given to a nickel metal matrix with imbedded alumina (Al_2O_3) nanoparticles as a model system for this process.

Chapter 5: Nickel - Alumina Uniformly Dispersed and Hierarchical Composites

The higher order structure presented here is a system consisting of nanoparticulate composite and single phase metal layers sequentially stacked to produce a long range periodic structure. This manufacturing technique produces materials with unique mechanical properties and at industrially relevant total size scales, and has immediate applications as a surface coating process for mechanical purposes and many other potential applications to be explored.

5.2 Experimental Methods

Previous work has extensively studied particle incorporation to create uniform nanocomposites (no secondary structure) for mechanical strengthening using an RDE system [1,2]. This study demonstrated the volume fraction of particles in the final composite follows the relation:

$$\frac{x_V}{(1-x_V)} = K\frac{\omega^{1/2}}{i} \qquad \text{EQ 5.1}$$

where x_v is the volume fraction of alumina, ω is the rotation rate (rpm), i is the current density (mA/cm^2), and K is a parameter based on the particle size, solution concentration, and valence of the electrolyte. This model applies in the limiting case where all particles that reach the deposition surface are incorporated into the film. This occurs when the current density is high enough and the mean stay time of the particle is long enough that the particle will sit on the surface and be encapsulated before it can move back into the solution. In this ideal case the particle incorporation rate can be simply written as a function of the particle diffusion length. The rotation rate of the RDE system controls the

hydrodynamic boundary layer, the effective diffusion length, between the bulk solution and the working electrode. Thus ω will be our means of directly controlling the volume fraction of particles in the composite.

An electrolyte solution composed of 1.24 M nickel sulfate, 0.5 M boric acid, 0.02 M nickel chloride, 0.5 g/L sodium dodecyl sulfate, 0.1 g/L coumarin, and 1% by volume alumina powder (350 nm diameter) was used for all experiments reported here unless otherwise noted. All solutions were deaerated using inert gas for at least 2 hours prior to deposition. Inert gas was continually blown over the solution during experiments to prevent oxidation. A Pine Research Instrumentation RDE motor and control system (AFMSRX and MSRX Speed Control) were used with a 5 mm diameter gold RDE. Ni foil was used as the counter electrode with a separate Ni foil used as a reference electrode. A LabView program was written and used to operate a National Instruments Compact DAQ (NI cDAQ-9172) that controlled the rotation rate of the RDE. A Princeton Applied Research potentiastat/galvanostat (PAR Model 263A) was used to control the deposition rate of the Ni.

For small-scale depositions, the Au RDE was electroplated with a copper strike prior to deposition to assist in releasing the final film from the Au substrate. This system, which parallels systems used in previous work, is diagramed in Figure 22.

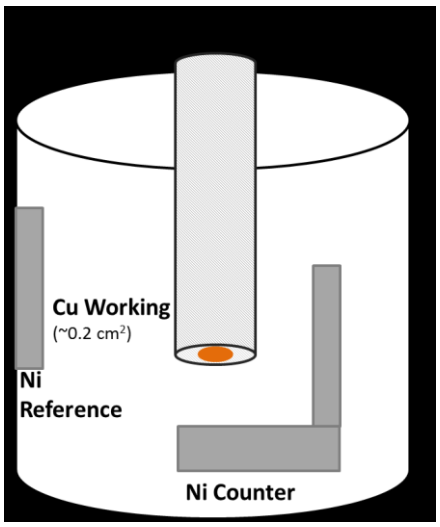

Figure 22: Schematic of electrochemical cell used for small scale depositions. The boundary layer at the surface of the working electrode is controlled by the rotation rate of the RDE. This layer serves as the effective diffusion length particles must travel in order to be incorporated into the film and is relatively uniform for small size scales (millimeters)

Schematics for the large-scale deposition designed and implemented here are shown in Figure 23. A rotating cylinder suspended in the solution works as an agitation source which allows for the incorporation of particles into the depositing metal. As the cylinder rotates, the particles stir into suspension and are incorporated into the growing nickel foil. The circular geometry of the cell ensures that the velocity of the cylinder is parallel to the entire working electrode surface. This allows for the same particle deposition rate along the full area of the film and allows for scaling of this system to

larger areas. The system utilized here uses a 1cm x 5cm strip of 3M copper conductive tape adhered to the wall of the electrochemical cell as the working electrode.

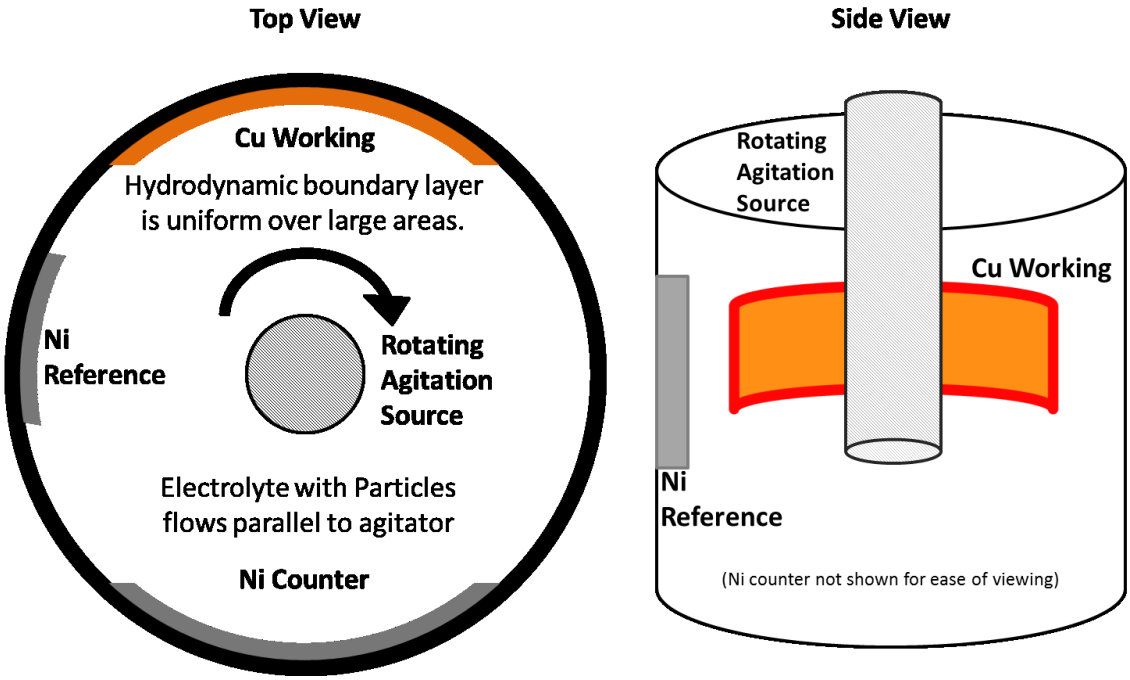

Figure 23: Schematic of Large-Scale Composite Electroplating System. A rotating cylinder moves the electrolyte parallel to the copper working electrode substrate. This stirring brings particles into suspension and provides uniform flow along the deposition surface.

Depositions were run at constant current through each experiment. Data reported here was generated at a current density of 20 mA/cm^2, corresponding to a deposition rate of about 20 microns/hour. Uniformly dispersed Al_2O_3 composites were manufactured using a constant rotation rate during deposition in either the RDE or the large-scale

system. For the layered composite structures the motor controller was set up such that the rotation rate would oscillate between 0 and a designated rpm as a square wave with equal lengths of time allotted to each rotation state. This ensured that equal amounts of Ni were deposited in each layer. Experiments were carried out under these deposition conditions using a rotation rate square wave signal with periods ranging between 2 minutes and 1 hour.

Depositions for hardness tests of layered samples were run such that final samples would consist of at least 50 layers and were also at least 200 μm in total sample thickness. Vickers Hardness tests of the samples were taken with the thickness of the film (growth direction) perpendicular to the indent area using a Leco Micro Hardness Tester.

Depositions for microtensile tests were run such that final samples would consist of at least 20 layers and were also at least 70 μm in total sample thickness. Microtensile specimens were cut out from large-scale samples using an electrical discharge machine (EDM). The gauge sections of these samples were 0.53 mm wide and 1.82 mm in length. These sample thicknesses were measured using optical microscopy and tensile tests were run using a custom microtensile rig described in Figure 24. Loads were recorded off of a 50 N load cell and optical images were taken during loading to track motion of surface features during loading. Digital image correlation (DIC) from published software (Digital Image Correlation and Tracking by Christoph Eberl, available through mathworks.com) was run on the captured images in MatLab to determine the strain during the tensile tests.

Figure 25 shows a microtensile specimen with . All tensile tests reported here were run at applied engineering "strain rates" of ~0.1 %/s. Although this is the rate that the linear actuator will operate at, play in the system and motion in the grips can result in a discrepancy between the applied strain and the actual strain. The actual engineering strain rate of the specimen will be somewhat lower than the applied rate and vary from sample to sample, however the strain rates between samples should be close enough to allow for comparison of mechanical properties between different test specimens.

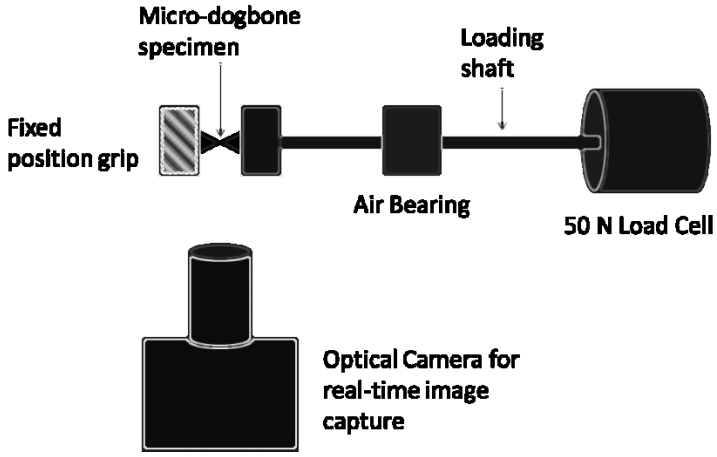

Figure 24: Schematic of Custom Microtensile Rig. The apparatus is comprised of a 50 N Load cell and linear actuator connected to a loading shaft. An air bearing is used to support the shaft and prevent friction from influencing load measurements. Custom grips are machined to support the micro-specimen. The grips do not clamp onto the sample in order to avoid damage in mounting the sample; instead a small (~2 N) pre-load is applied in order to secure the sample. An optical camera with magnification lens is used to digitally record images of the specimen during loading.

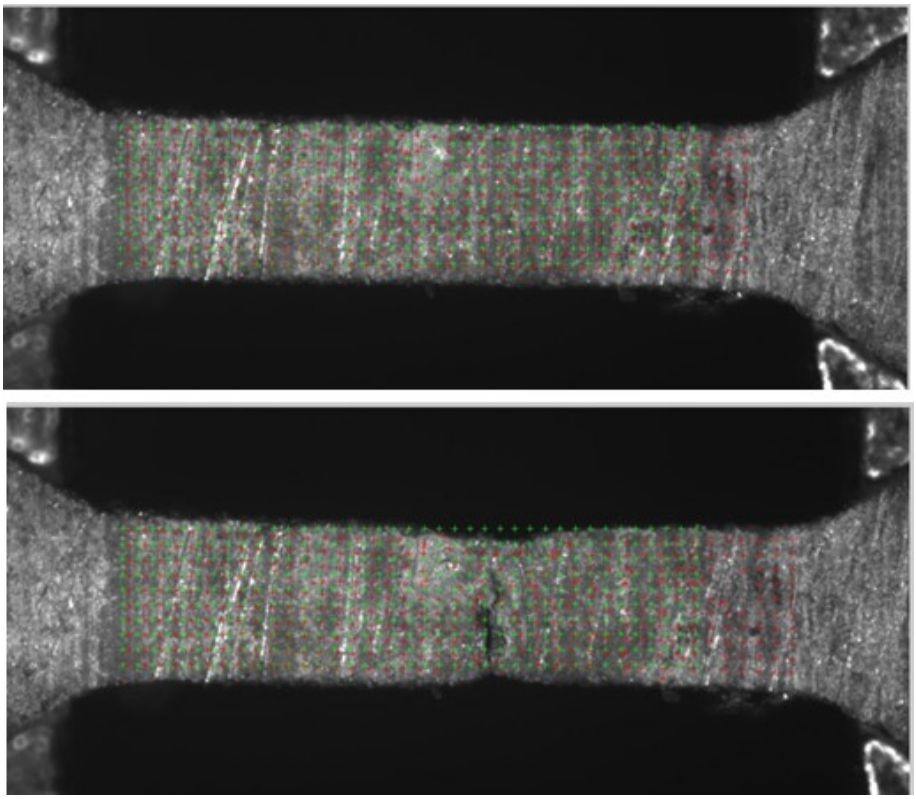

Figure 25: Optical Image of Microtensile Specimen with DIC Tracking Grid Superimposed (width of the gauge section is 0.53 mm); A 50 x 10 grid mesh is generated in MatLab on an image of the pre-loaded gauge section of the specimen. Each section (cell) of the grid tracks motion of the features present in the original cell. The original mesh is shown as green crosses with the current position of each cell shown as red crosses. The top image shows the sample during initial deformation stages. The bottom image shows the sample during ductile failure after significant elongation and necking occurred.

5.3 Results and Discussion

5.3.1 Uniformly Dispersed Nickel - Al_2O_3 Composites

Nickel matrices with uniformly dispersed Al_2O_3 nanoparticles were manufactured using the procedures described above. The uniformly dispersed composite (UDC) samples showed good particle incorporation with no significant conglomeration as seen in Figure 26.

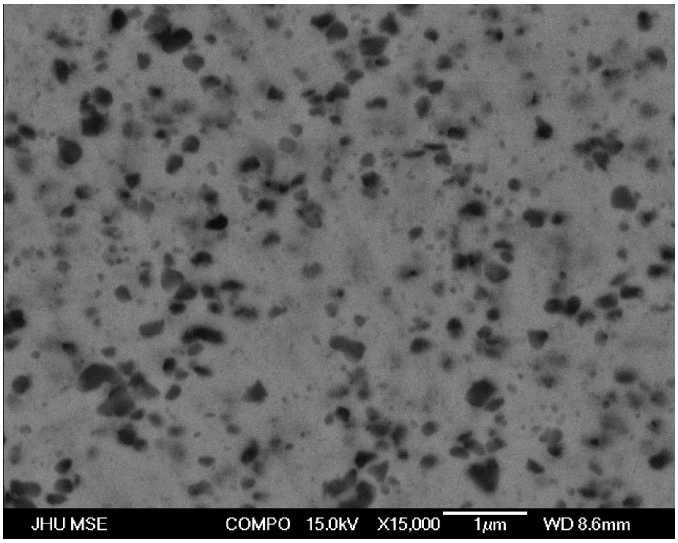

Figure 26: Scanning Electron Microscope image of uniformly dispersed 350nm Al_2O_3 particles in a Ni matrix. The particles do not show significant conglomeration and appear randomly distributed throughout the nickel matrix

The volume fractions of the composites were proportional to the rotation rate of the RDE in the case of small scale systems in line with previously reported work [1,2]. These films were crack and void free for particle volume fractions up to ~25% for

samples with 350 nm Al_2O_3 particles and ~5% for samples with 50 nm Al_2O_3 particles. Beyond this volume fraction, significant particle-particle contact begins to occur, which results in significant embrittlement (see Figure 27).

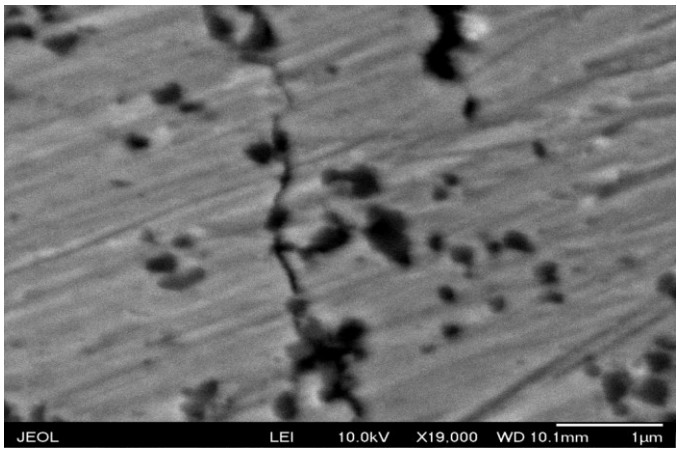

Figure 27: Crack formation and conglomeration in high volume fraction (>25% 350 nm Al_2O_3) uniform composite. Sample cracked on removal from electrochemical cell

Large-scale samples were only manufactured using 350 nm Al_2O_3 particles as the hard 50 nm reinforced particles are relatively brittle and difficult to handle over large areas. SEM images of large-scale samples show no significant microstructural differences from the small-scale RDE materials. Figure 28 shows a plot of particle volume fraction versus rotation rate for the large-scale system.

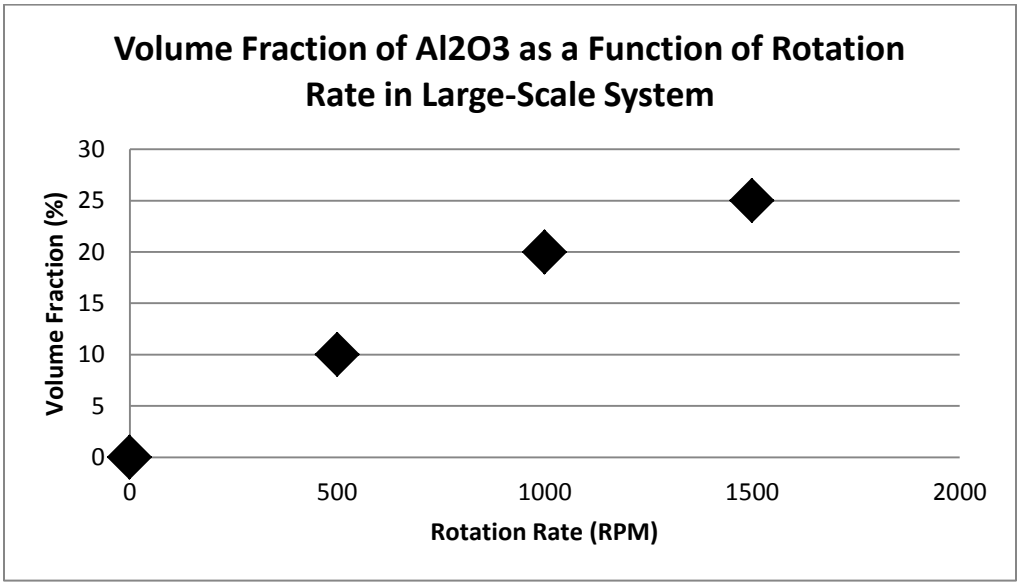

Figure 28: Volume Fraction of Al_2O_3 in samples manufacture in large-scale system. The volume fraction of particles in the composite increases with rotation rate. Volume fractions were determined using area fractions from SEM images of cross sections of the samples.

For these composite structures we expect a change in mechanical response that follows standard rule of mixtures behavior iso-stress conditions. That is the applied load is uniformly distributed about an arbitrary cross section of the composite material. Under these conditions it can be shown that the modulus of the composite will be a function of the moduli and volume fraction of the two constituent materials according to Equation 5.2:

$$\frac{1}{E_{composite}} = \frac{\nu_{particle}}{E_{particle}} + \frac{\nu_{matrix}}{E_{matrix}} \qquad \text{EQ 5.2}$$

where E is the elastic modulus and ν is the volume fraction of the indicated material. Percolation of particles and subsequent ramifications on mechanical properties are ignored in this work as the relevant particle volume fractions are below 25%. It is also assumed that the interface volume is small compared to the volume of the particle and can be ignored. For the case of 20% by volume composite of alumina in nickel, we find $E_{composite} = 227$ GPa, which is quite close to the modulus of pure nickel of 207 GPa. Thus we do not expect significant changes in the elastic modulus of the composite at these volume fractions.

We do, however, anticipate strengthening of the material through impedance of dislocation motion by the introduction of a second phase. For the case of a hard particle in a soft matrix, we can assume a bowing mechanism for impedance of dislocation motion through the material. This is true for the case where the energy required for the dislocation to pass through the particle and generate new particle-matrix interface area is higher than that required for the dislocation to deform around the particle. Thus a dislocation will be pinned at a particle but pass through the matrix between two particles. This strengthening mechanism is a function of the spacing between particles as shown in Equation 5.3:

$$\Delta\sigma_y \approx \frac{\mu b}{\langle L_p \rangle - 2r_p} \qquad \text{EQ 5.3}$$

where $\Delta\sigma_y$ is the increase in yield strength of the material, μ is the shear modulus of the matrix, b is the magnitude of the burgers vector of the dislocation in the matrix, r_p is the

average radius of the particle, and $\langle L_p \rangle$ is the average spacing between the centers of the particles.

$\langle L_p \rangle$ can be calculated as a function of the particle volume fraction ($\nu_{particle}$) and the average particle volume ($V_{particle}$) as follows (assuming the particles are spherical and uniformly dispersed).

$$\frac{1}{\langle L_p \rangle^3} = \frac{N_p}{V_{total}} = \frac{\nu_{particle}}{V_{particle}} \therefore \langle L_p \rangle = \sqrt[3]{\frac{4/3 \pi r_p^3}{\nu_{particle}}} \quad \text{EQ 5.4}$$

Substituting into Equation 5.3 we find that the strengthening of the material is inversely proportional to the particle size.

$$\sigma_y = \sigma_{pure,y} + \frac{\mu b}{r_p}\left(\sqrt[3]{\frac{4/3 \pi}{\nu_{particle}}} - 2\right)^{-1} \quad \text{EQ 5.5}$$

Thus use of nanoparticle reinforcements as opposed to micro or macro reinforcements can significantly increase the yield strength of the composite material even at relatively low volume fractions. It is also worthwhile to note that the modulus is solely a function of volume fraction, so the effective modulus and strength of the composite material can be decoupled by controlling the particle volume fraction and the particle size of the reinforcing phase independently.

The UDC samples showed hardness increases that followed a dislocation bowing mechanism (hardness increase is inversely proportional to the average spacing between Al_2O_3 particles and therefore proportional to the volume fraction). The measured Vickers Hardness as a function of particle volume fraction of the Ni- Al_2O_3 composite structure is shown in Figure 29.

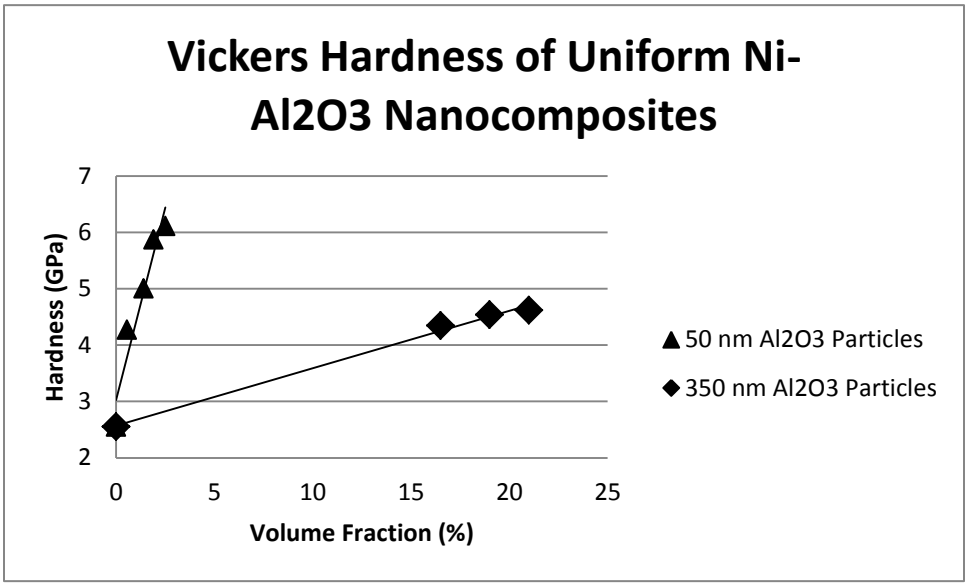

Figure 29: Vickers hardness data for uniform composite structures of Ni and 50 and 350 nm Al_2O_3 particles. Hardness measurements were taken with a load of 0.2 kgf held for 40 s. These results parallel those found previously.

Tensile tests were performed on micro-dogbones cut from the large-scale deposited materials. Yield strengths were determined using a 0.2% strain offset. Figure 30 shows the yield strengths of the uniform composite samples. These measurements

show very good agreement with the predicted strength increases from the yield stress of the pure nickel according to Equation 5.5.

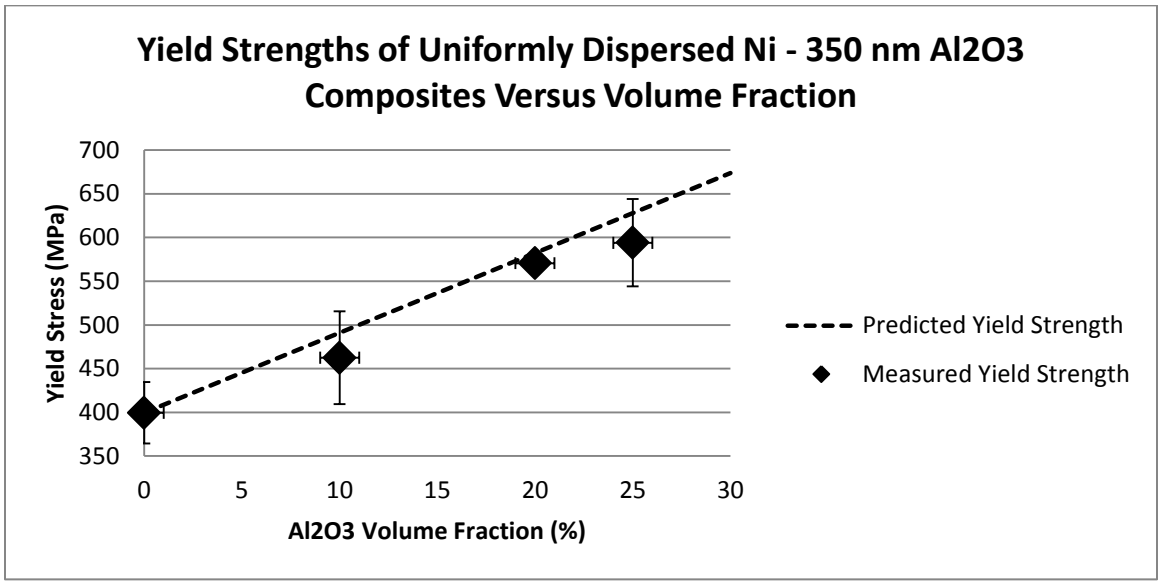

Figure 30: Yield Strength of Ni-Al2O3 Uniformly Dispersed Nanocomposites Versus Volume Fraction. The dashed line represents the predicted yield strength according to Equation 5.5 given the measured yield strength of the pure nickel sample. The diamond points represent averages of measured yield strengths from microtensile tests of composites of various volume fractions and matches well with the predicted values. This supports the concept that the strengthening of these composites is due to a dislocation bowing mechanism.

The tensile strain to failure was also measured for these uniform composites. Figure 10 shows approximate strain to failures for different composite volume fractions.

It was generally found that increases in strength corresponded to decreases in ductility (strain to failure). It is important to note that while the yield stresses for a particular microstructure were very consistent between samples, the strain to failure is highly variable and should only be interpreted qualitatively. In handling the films and microtensile specimens, small scratches and defects are easily added to the material. EDM cutting can also lead to rough surface features at the edges of the specimen. These defects can be significant in size compared to the cross section of the material and can induce sudden, critical failure. These defects will lower the measured strain to failure of the system and have an especially strong impact on brittle microstructures.

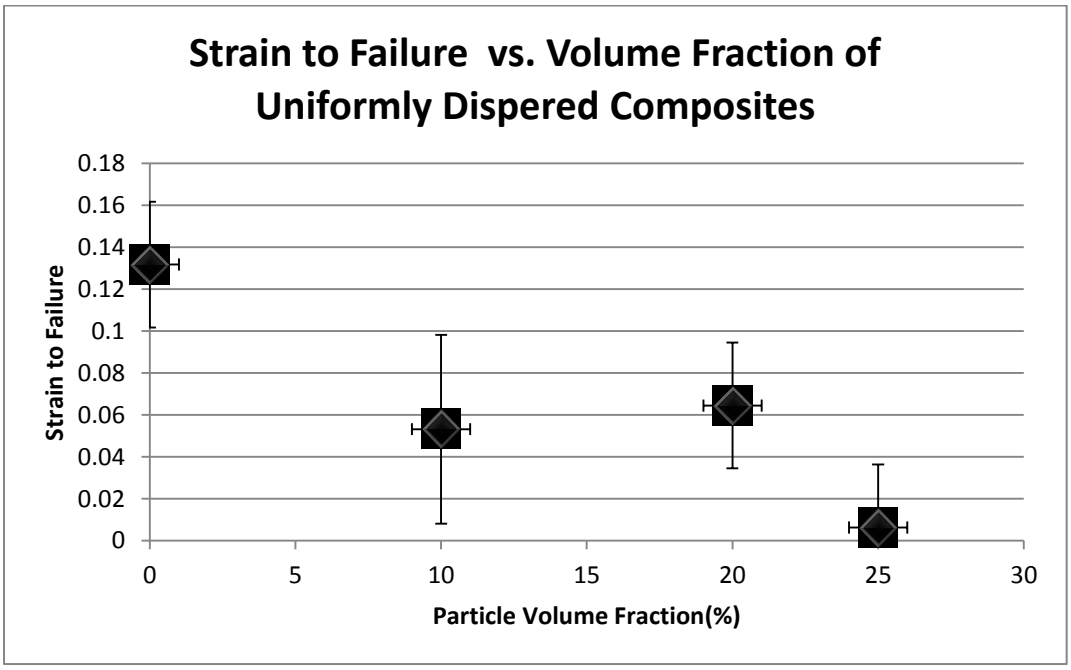

Figure 31: Strain to Failure of Ni-Al2O3 Uniformly Dispersed Nanocomposites Versus Volume Fraction. Although these points represent averages of several samples for each

volume fraction, the strain to failure values should only be discussed qualitatively as handling and preparation can produce various defects that significantly reduce the strain to failure of a sample.

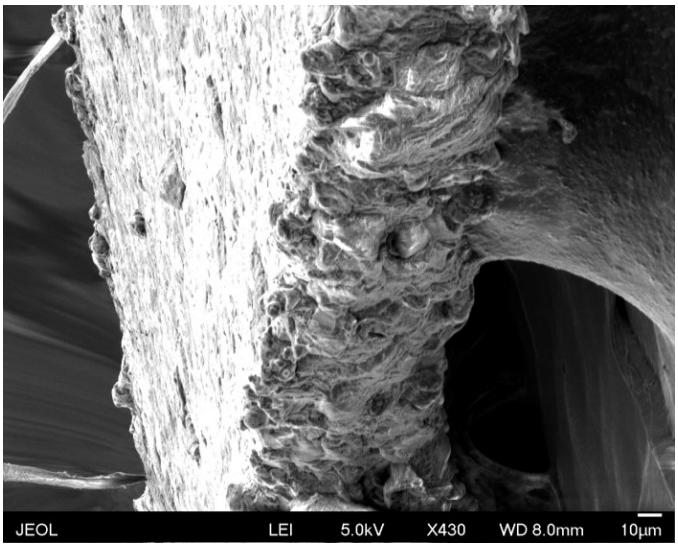

Figure 32: SEM of EDM Cut Surface Shows Roughness of Edges of Microdogbone Samples. The melt and recast region is typically 10 - 20 microns deep into the sample. The total recast region is small compared to the 530 micron width of the gauge, however local sharp features can lead to stress concentrations, crack formation, and failure.

In addition to mechanical properties characterization, it is useful to check other properties of interest that may be affected by the composite structure. Many industrial uses of Ni require ferromagnetic behavior so we have tested the magnetization properties of the composite material in order to assess possible negative property effects. Magnetic hysteresis measurements show that there is no significant change in the width of the

hysteresis loops and that the relative saturation magnetization drop is approximately equal to the volume fraction of Al_2O_3 particles in the samples (Figure 33). This indicates that the particles are simply acting as excluded volume from the ferromagnetic Ni matrix. The matrix magnetic properties are preserved despite significant changes in the mechanical properties of the material.

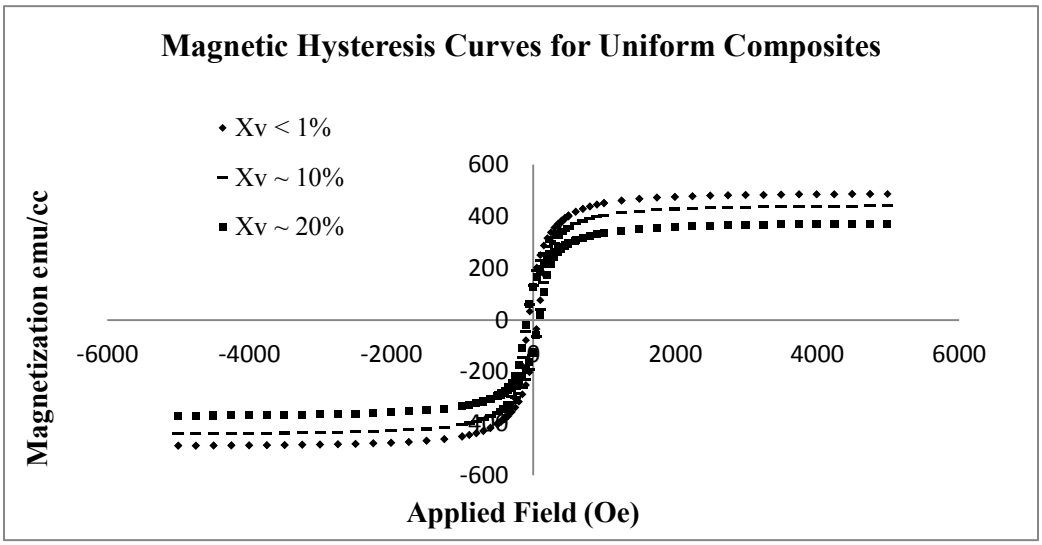

Figure 33: Magnetic hysteresis measurements for uniform Ni – 350 nm Al_2O_3 composite structures with particle volume fractions ranging from < 1% to 20%.

5.3.2 Layered Hierarchical Composite Structures

Using the same experimental techniques used to manufacture uniformly dispersed composite structures, we successfully produced well defined layered hierarhcical composite structures from metal ceramic nanocomposites simply by varying the rotation rate of the cylindrical agitator with time while continuously electrodepositing the Ni. Discrete layers composed of nominally pure Ni and 80% Ni: 20% Al_2O_3 by volume were formed with distinct interfaces between the single phase and composite regions. This particular volume fraction was chosen for the composite region of this hierarchical structure because the uniform results for the base composite demonstrated significant yield strength enhancements (an increase of 150 MPa) while still maintaining some ductility (~6% strain to failure). Formation of individual layers has been demonstrated at thicknesses as thin as ~1 micron to as thick as 50 microns. Interfaces were well resolved with interface thicknesses of the order of the nanoparticle size in both RDE and large-scale systems. However, the large-scale deposited materials do appear to have higher concentrations of alumina particles in the nickel-rich region. As the layer thicknesses approach the interface resolution, the higher order structure becomes less distinct. Smearing of layers becomes apparent at individual layer thicknesses < ~2 microns and the structure approaches a random dispersion of alumina particles in nickel rather than an organized hierarchy. It may be possible to improve interface resolution by pausing deposition during transitions between 0 and 1500 rpm to allow for the fluid dynamics to reach steady state or by using smaller scale particles. It is also noted that the nickel

matrix was continuous through the interfaces where in other artificial multilayer structures the interface separates two distinct phases. It was demonstrated that an overall thickness of up to 1mm was possible while maintaining sharp control over the microscale and the nanostructure of the individual layers. It is expected that this process would be easily scalable to large deposition surface areas and total thicknesses for technological applications given the controllable and scalable fluid dynamics of the large deposition system. Since the incorporation of particles into the metal matrix is well defined as a function of rotation rate, it is also feasible to make more complex layered and graded structures with linear or non-linear variations of volume fractions through the thickness of the deposited material. These functionally graded structures have also been proposed as potentially beneficial hierarchical structures [10-19].

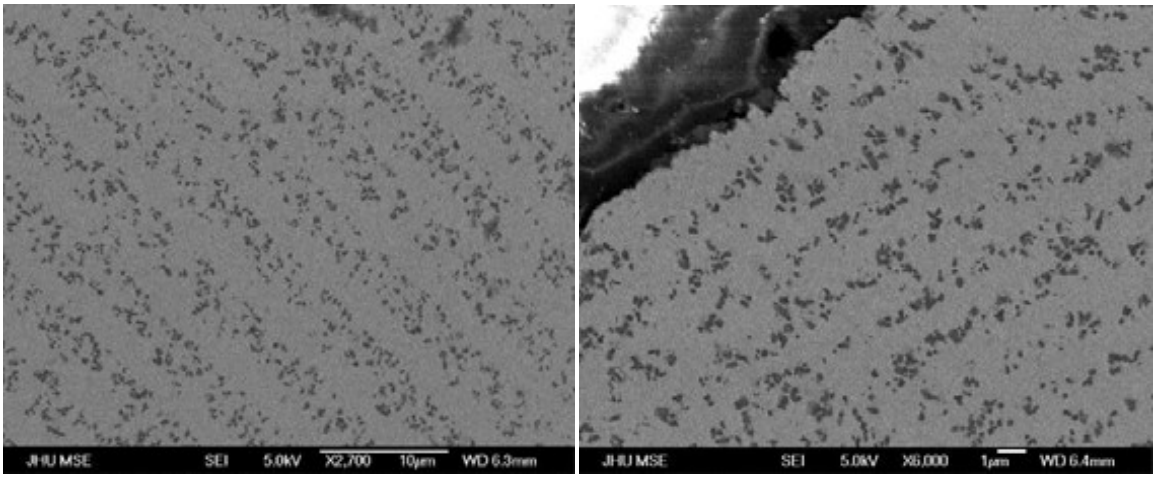

Figure 34: SEM micrographs of hierarchical systems composed of pure Ni layers and Ni-350 nm Al_2O_3 composite layers manufactured using an RDE; a) ~2.5 micron layers; b)

~900 nm layers, some smearing occurs between layers as individual layer thicknesses approach the ceramic particle size.

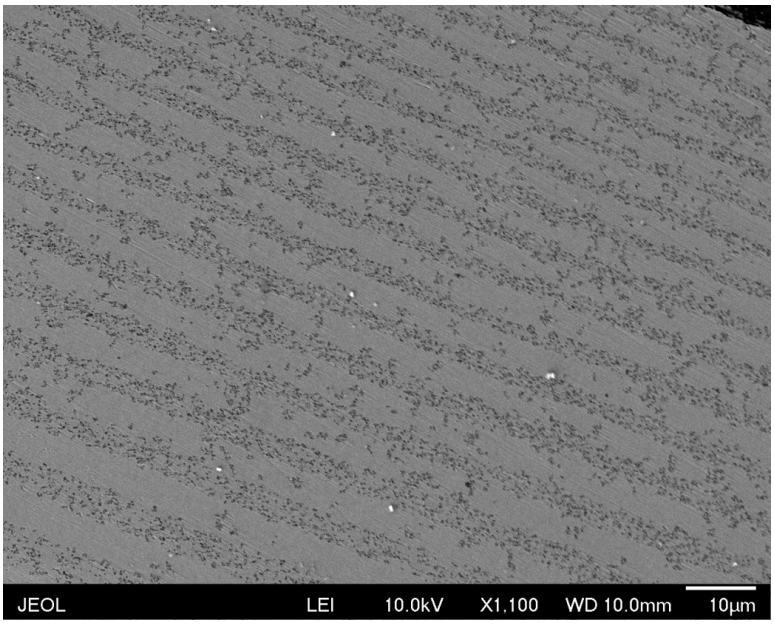

Figure 35: SEM of Layered Structure Manufactured using Large-Scale System. This system showed similar interface resolution and microstructure to the RDE system, however there was more substantial particle incorporation into the layers intended to be pure nickel.

Knowing the analytical expressions for the modulus and strength of a uniformly dispersed composite, it is possible to derive analytical solutions for the approximate modulus and strength of a structure composed of layers of composite and layers of pure metal. Here we will consider the cases of axial loading in-plane with the layers. In this case the modulus of the hierarchical composite is given by Equation 5.6:

$$E_{hc} = E_{composite}\nu_{composite} + E_{pure}\nu_{pure} \quad \text{EQ 5.6}$$

where E_{hc} is the modulus of the hierarchical composite material under this loading condition, $E_{composite}$ is the modulus of the UDC region as given by Equation 5.2, $\nu_{composite}$ is the volume fraction of the composite layered material, E_{pure} is the modulus of the pure metal layer which is the same as the matrix material in the composite layer, and ν_{pure} is the volume fraction of the pure layered material.

Substituting Equation 5.2 into Equation 5.6 and selecting the case where the matrix material is the same as the material of the neat layer, we arrive at Equation 5.7 for the modulus of this hierarchical material.

$$E_{hc} = \frac{1}{\frac{\nu_{particle}}{E_{particle}}+\frac{\nu_{matrix}}{E_{matrix}}}\nu_{composite} + E_{matrix}\nu_{pure} \quad \text{EQ 5.7}$$

For yielding to occur the material must be stressed to the point that a dislocation can generate at a free surface, move through the entirety of the material, and terminate at a free surface. In order for true yielding to then occur in the layered samples described here, the stress must be sufficiently high that dislocations move through both the soft and hard layers. During purely elastic deformation of the material we expect the stress-strain relation of the material to follow Equation 5.8:

$$\sigma_{hc} = \left[\frac{1}{\frac{\nu_{particle}}{E_{particle}}+\frac{\nu_{matrix}}{E_{matrix}}}\nu_{composite} + E_{matrix}\nu_{pure}\right]\epsilon_{hc} \quad \text{EQ 5.8}$$

where σ_{hc} is the stress in the hierarchical composite structure.

After straining the material sufficiently, the soft layers will reach their yield stress, $\sigma_{pure,y}$, and cannot effectively bear additional load.

$\sigma_{pure,y} = \sigma_{matrix,y} + \frac{\mu b}{L}$, L = layer thickness EQ 5.9

The load in the soft layer beyond this strain can be approximated as the yield stress of the layer itself. This is a common analytical assumption that treats the addition of plastic flow stress as a small compared to the yield stress. The stress-strain behavior of the hierarchical composite in this regime ($\epsilon_{hc1} > {}^{\sigma_{pure,y}}/_{E_{matrix}}$) would follow Equation 5.10.

$\sigma_{hc} = \frac{1}{\frac{v_{particle}}{E_{particle}} + \frac{v_{matrix}}{E_{matrix}}} v_{composite} \epsilon_{hc} + \sigma_{pure,y} v_{pure}$ EQ 5.10

The additional load is taken elastically by the hard layer until that layer also reaches its yield stress. Then the layered composite material will reach its yield stress according to the rule of mixtures.

$\sigma_{hc,y} = \sigma_{composite,y} v_{composite} + \sigma_{pure,y} v_{pure}$ EQ 5.11

Thus we expect the yield strength of the layered composite structure to be in between that of the pure layer and UDC layer. Equation 5.11 can be re-written as:

$\sigma_{hc,y} = \sigma_{matrix,y} + \frac{\mu b}{L} v_{pure} + \frac{\mu b}{\langle L_p \rangle - 2r_p} v_{composite}$ EQ 5.12

From this we find that the yield strength of the hierarchical composite should not exceed that of associated the uniformly dispersed composite unless the layer length scale, L, is smaller than the inter-particle spacing. In the systems described here, L is significantly larger than the inter-particle spacing of the uniformly dispersed composite. Vickers hardness testing with a load of 1 kg and a hold time of 40 s was performed on samples with individual nickel layer thicknesses ranging from 1 to 5 microns and control samples of pure nickel and a UDC (20% Al_2O_3 volume fraction) of the same composition of the composite layers within the hierarchical structure. Bilayer thickness is defined as the thickness of a pure nickel region plus the thickness of a neighboring composite region. The volume fractions of Al_2O_3 within a composite layer and for the overall material were the same for all of the samples reported here. The only variable between hierarchical samples was the layer thickness. Results of these tests are shown in

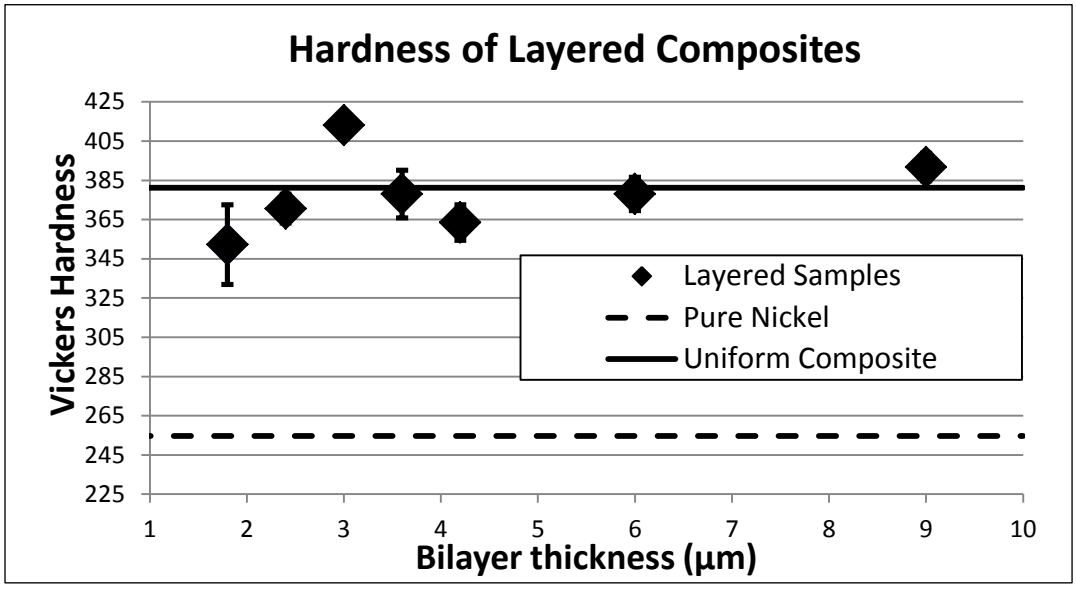

Figure 36. Samples showed increased hardness with decreasing layer thickness, which is expected according to Equation 5.12. A peak in hardness was observed at layer thicknesses of ~ 1.5 microns and bilayer thickness of ~ 3 microns. Layered structures smaller than this begin to reach the interface resolution limit of the deposition process and so they begin to behave more like a uniformly disperse composite than a hierarchical structure. While these trends as a function of layer thickness are somewhat expected, the overall hardnesses of the layered material is significantly higher than predicted by the rule of mixtures. The layered samples show hardnesses of equal or greater value to the hardness of the uniformly dispersed composite. Although we are adding soft material into the sample, we are still achieving similar strengths.

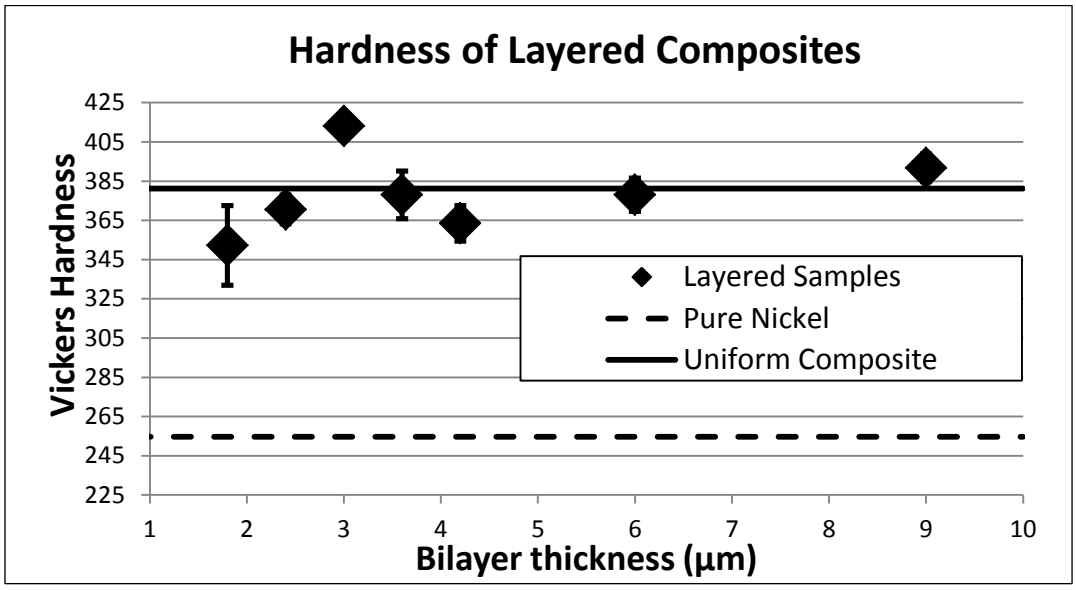

Figure 36: Plot of hardness values for layered composites with varying layer thicknesses; the measured hardness is well above any rule of mixtures of the layer component; a peak

in hardness in the layered samples is seen at ~3 microns bilayer thickness (the smallest structure before interface resolution becomes significant compared to layer thickness)

These trends in strengthening were also observed in tensile specimens of similar composition and structure. The only difference between the tensile specimens and hardness specimens is that there are slightly high concentrations of Al_2O_3 particles in the "pure" nickel layers. These scale up samples also had slightly worse interface resolution with layers becoming indistinct below ~2.5 micron individual layer thicknesses. Again, samples that consisted of layers of UDCs and layers of nearly pure nickel showed strengths as high, or higher than the strength of the corresponding uniformly dispersed composite. Once layer thicknesses approach the resolution limit of the system, the measured yield strengths drop as the material structure approaches that of a uniformly dispersed composite with a lower volume fraction than the control UDC sample. This corroborates the trends seen in the hardness measurements and implies this property is intrinsic to the material structure and not an artifact of the measurement technique.

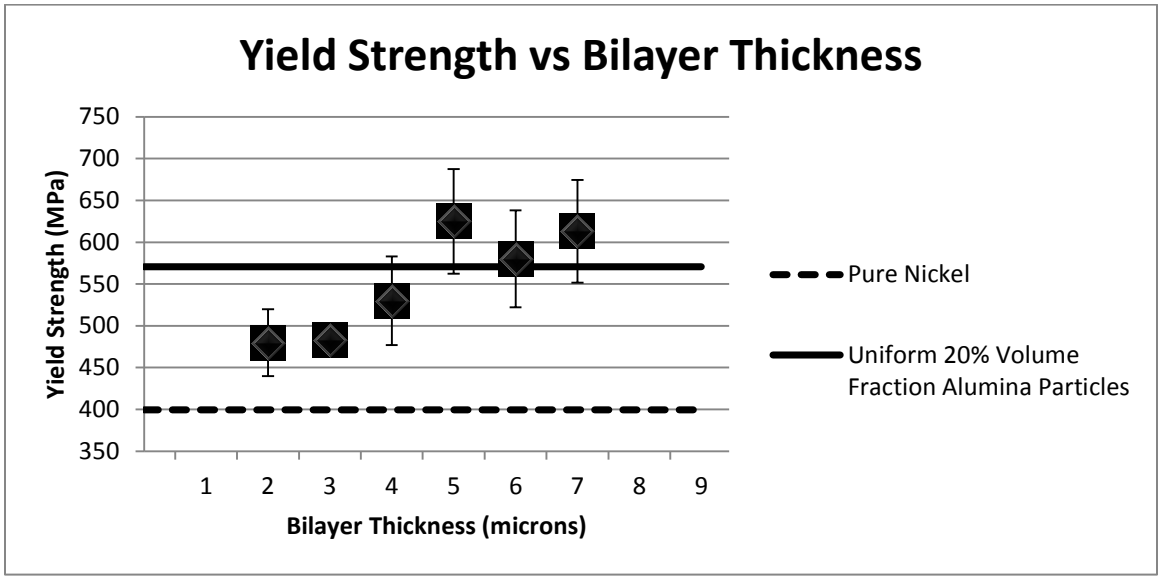

Figure 37: Average Microtensile Yield Strength versus Bilayer Thickness of Simply Layered Hierarchical Composite. Some layered microstructures displayed yield strengths above their base components. Once layer thicknesses approached the interface resolution, the microstructure returns to that of a uniformly dispersed composite and the strength drops accordingly. These tensile trends parallel hardness measurements.

In order for the layered composites to exceed the rule of mixtures, significant deviations from the analytically predicted strength from Equation 5.12 must occur. The fundamental assumptions in deriving this equation are well grounded in static mechanics, however, one of the key assumptions was that the flow stress in the material was small compared to the yield stress. This is reasonable based on the stress-strain curves for pure nickel (See Figure 38). However, it is possible that the presence of particles at the edges of the nominally pure nickel layers may be contributing to the flow stress of these layers.

Increases in the flow stress would allow the soft nickel layers to take on more load and result in a larger predicted hierarchical composite yield stress. It is also worth noting that there is some particle contamination in the Ni-rich layers. These particles may be contributing to the strengthening of the material by increasing the yield strength of the soft layers. More detailed analytical and computational models will need to be developed in order to fully explain the strengthening mechanism but these reasons are presented as possible rationalizations for the behavior.

In addition to the observed strength enhancements, layered samples show significant promise in improving the ductility compared to that of the UDC samples. The addition of the soft and ductile nickel layers seems to increase toughness of the material while maintaining high yield strengths (Figure 38).

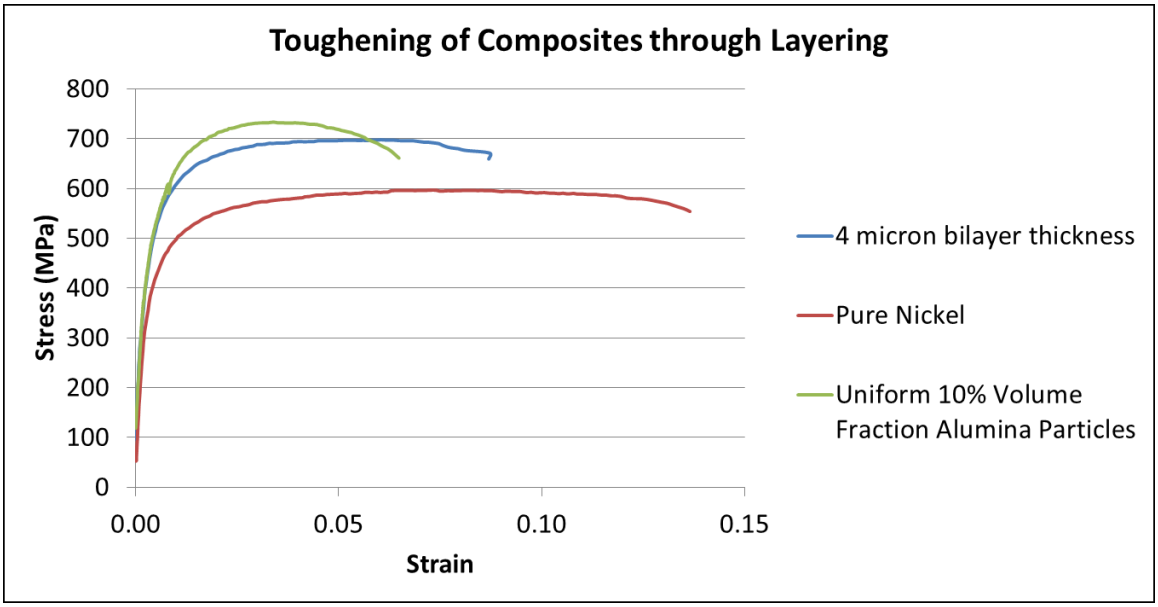

Figure 38: Examples of Stress Strain Curves of Microtensile Specimens of Various Microstructures. Some layered samples can maintain similar yield strengths to the uniform composites with substantial increases in ductility. Select hierarchical samples even show toughnesses close to that of the pure nickel.

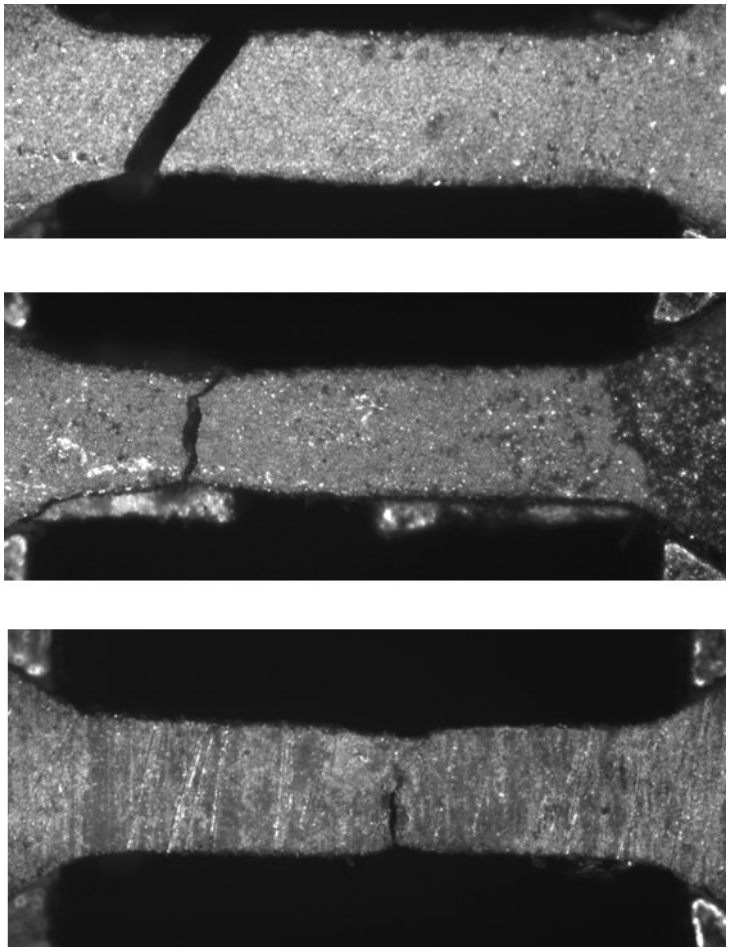

Figure 39: Optical Images of Fracture in Microtensile Samples of Various Composite Microstructures; (Top) Brittle failure of UDC with 20% 350 nm alumina particles with little necking and clear 45 fracture line, (Bottom) Ductile failure of pure nickel sample with significant necking, (Middle) Sample of 4 micron bi-layered composite of nickel and 20% alumina composite layers shows necking and cup-cone failure.

Because of the difficulty in accurately determining the strain to failure in the micro-tensile specimens, specific ductilities and toughnesses are not reported here. However, the fracture surfaces can be studies to reveal trends of ductility and embrittlement. Figure 39 shows optical images of failure of samples during tensile testing. The UDC composites clearly show brittle failure with little necking and failure along a 45° angle to the loading direction. The pure nickel samples show significant necking and ductility before failure. The layered composite samples tend to have cup-cone type failure after some necking in the sample. This fracture mechanism is indicative of an increase in ductility compared to the UDC samples.

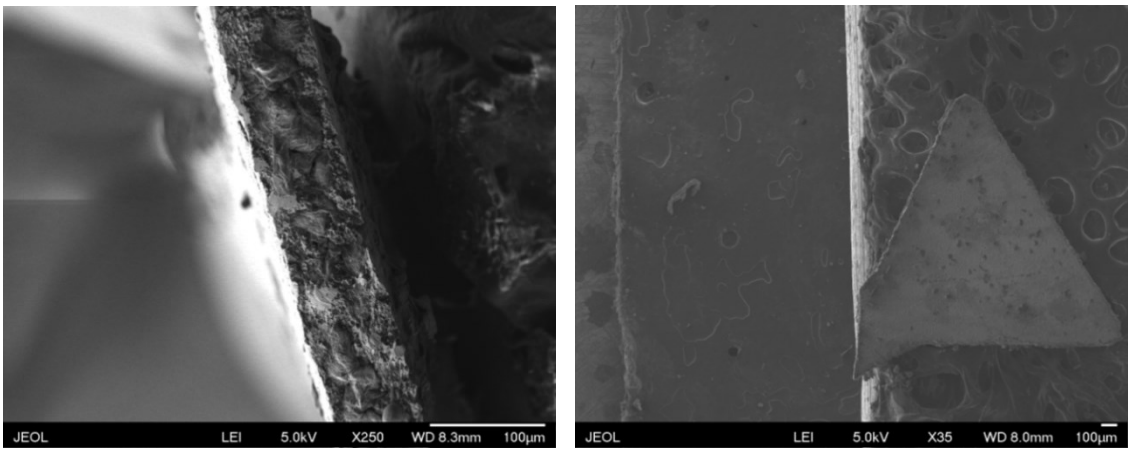

Figure 40: SEMs of Fracture Surface of Uniformly Dispersed Composite Microtensile Sample of 20% 350 nm Alumina. Relatively clean and shear fracture surface is indicative of brittle failure.

SEM Images of the fracture surfaces were also taken to investigate the microstructural fracture surface. Figure 40 shows images of the surface perpendicular and in line with the loading direction of a UDC sample. The sample fractured cleanly and resulted in a relatively flat fracture surface. Figure 41 shows a high magnification image of the failure surface. This surface shows exposed particles and pits where particles likely pulled out during failure.

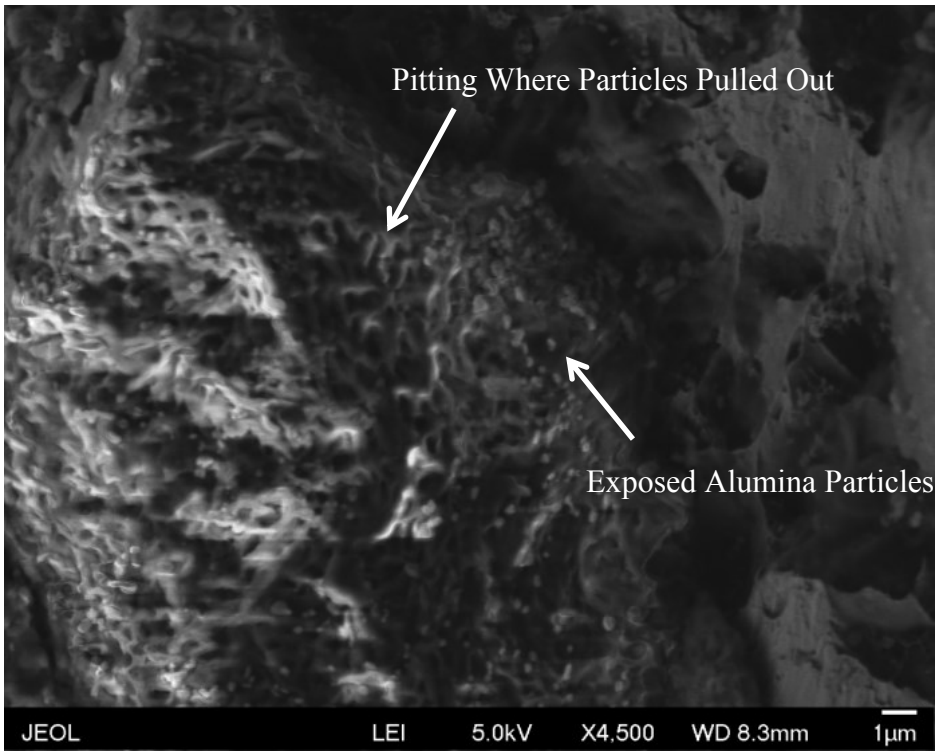

Figure 41: SEM of Fracture Surface of Uniformly Dispersed Composite Microtensile Sample. Within the grain shown some alumina particles are exposed while pitting nearby appears to be from pullout of other particles. Few drawn, ductile regions were found in this sample.

Figure 42 and Figure 43 show top down views (loading direction is in the plane of the image) of the fracture surface of a 6 micron bilayer hierarchical sample. This sample shows a cup-cone style fracture surface that has many three-dimensional features. High magnification images from this orientation show stacks of layers that have highly rounded edges. Figure 44 shows an edge on views (loading direction is into the plane of the image) of the same sample. The failure surface has many thin ligament-like features. These features are seen throughout the failure surface. These features indicate high degrees of local plastically at the failure surface. These significant differences in fracture surfaces indicate the layered hierarchical samples have more ductility than their UDC counterparts even though they have similar strengths.

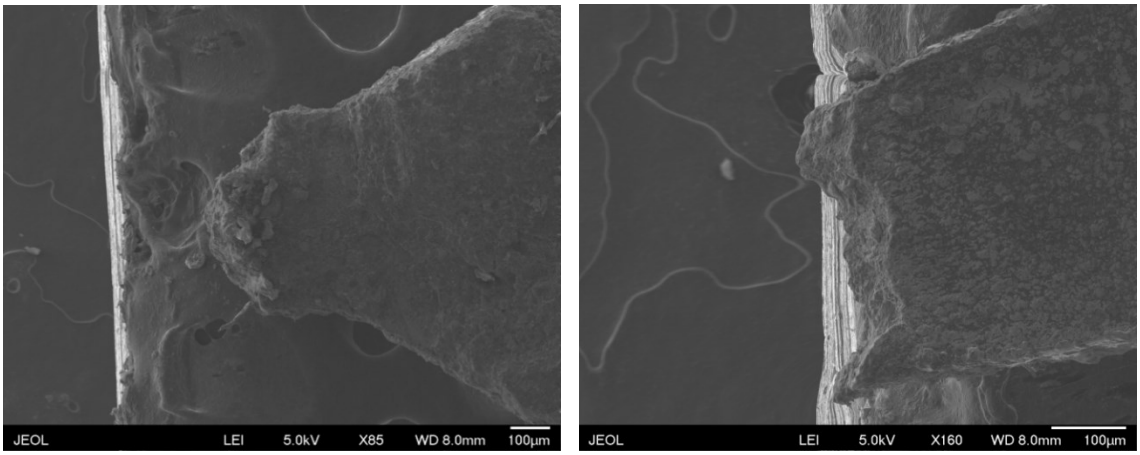

Figure 42: SEM of Fracture Surface of Layered Hierarchical Composite Sample (6 micron bilayer thickness). Samples show cup cone failure indicative of ductile failure.

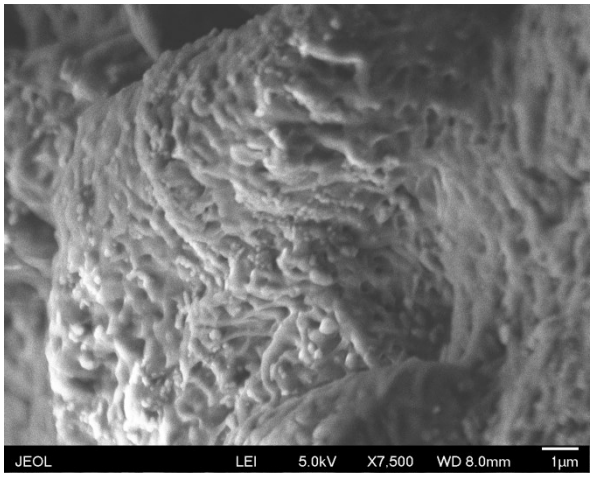

Figure 43: SEM of Fracture Surface of Layered Hierarchical Composite Sample (6 micron bilayer thickness) Layers are stacked in-plane of the image. Three dimensional shape of fracture surface indicates ductile failure.

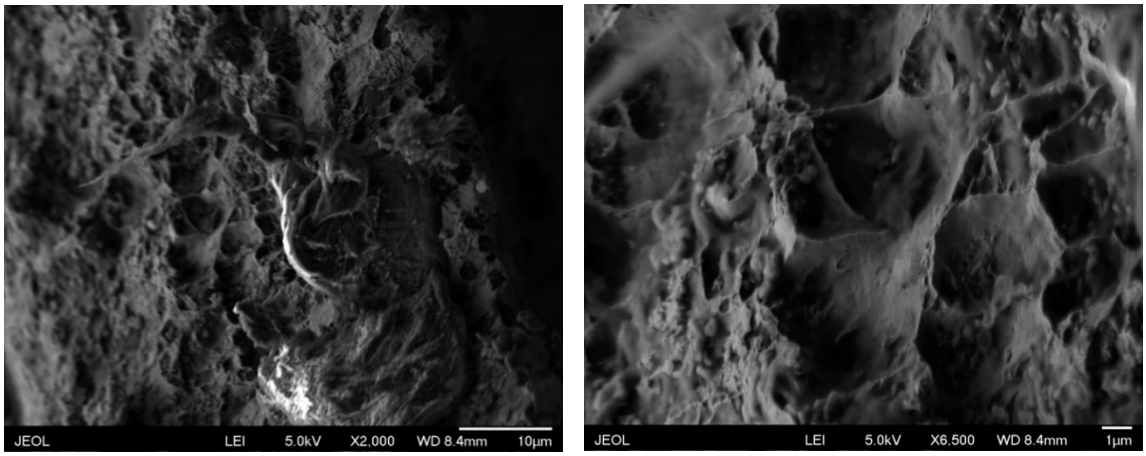

Figure 44: SEM Images of Fracture Surface of 6 Micron Bi-layer Composite Material; Layers are stacked perpendicular to the image and the loading direction is into the plane of the image. The majority of the fracture surface had thin, elongated segments of material that may be a result of plastic flow near or during failure.

5.3.3 Manufacturing of 3-D Hierarchical Composite Structures

In addition to simple layered structures, three dimensionally ordered structures have also been of interest as beneficial hierarchical structures. Specifically, bone and nacre have been shown to have structures composed of hard ceramic plates layered with a softer material and these stacks of plates are mated by another region of soft material. These materials demonstrate high yield strengths while maintaining toughness and this is often attributed to their unique composite structure. While full 3-D control of this deposition system is not feasible, it is possible to intentionally add features to the initial substrate material in order to generate a final 3-D structure. In order to demonstrate this Cu substrates were grooved using a diamond scribe before depositing the composite.

Optical images of cross sections of the layered samples deposited onto grooved Cu substrates are shown in Figure 45. These micrographs show that in the flat regions of the sample the layered structure is well preserved and parallel to the growth direction but that layering is disrupted in region above the substrate pattern through a significant thickness of the film. The layers curve and track the geometry of the substrate grooves slightly but the region directly above the minimum in the groove seems to be void of any Al_2O_3 particles. This lack of incorporated particles is likely due to a strong Lorentz force experienced by the particles in the region above the groove.

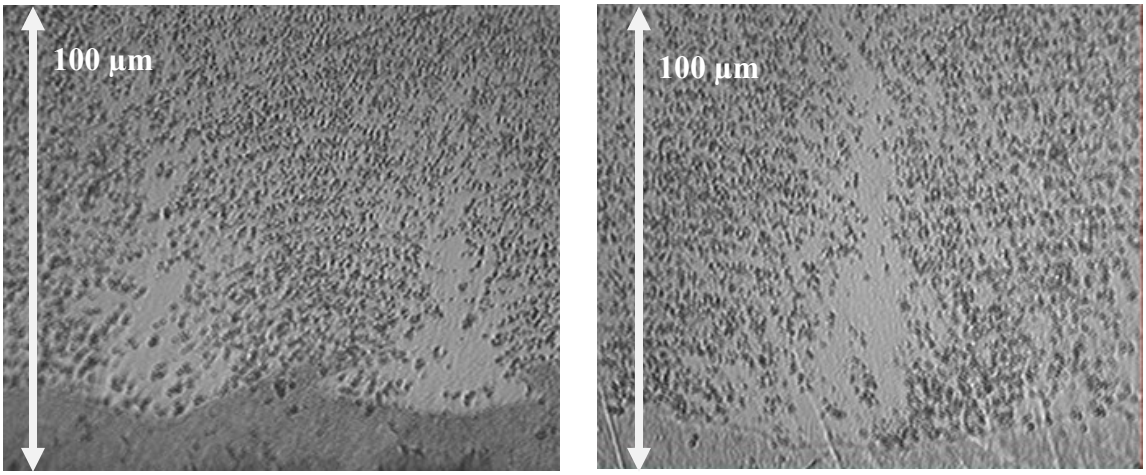

Figure 45: Optical images of cross sections of composite structure near a surface groove; There is a low concentration of particles in the deposited material directly above the groove.

As shown in Figure 46, the net charge of the grooved surface will result in a greater flux in the area above the groove compared to the flat surface. This is associated with a stronger electric field. The surfactant used in these experiments is anionic so the

particles are repelled from the negatively charged working electrode. At typical applied voltages this energy is small compared to thermal energy, but the grooved region may generate strong enough electric fields for the electrophoretic motion to be significant compared to the Brownian motion.

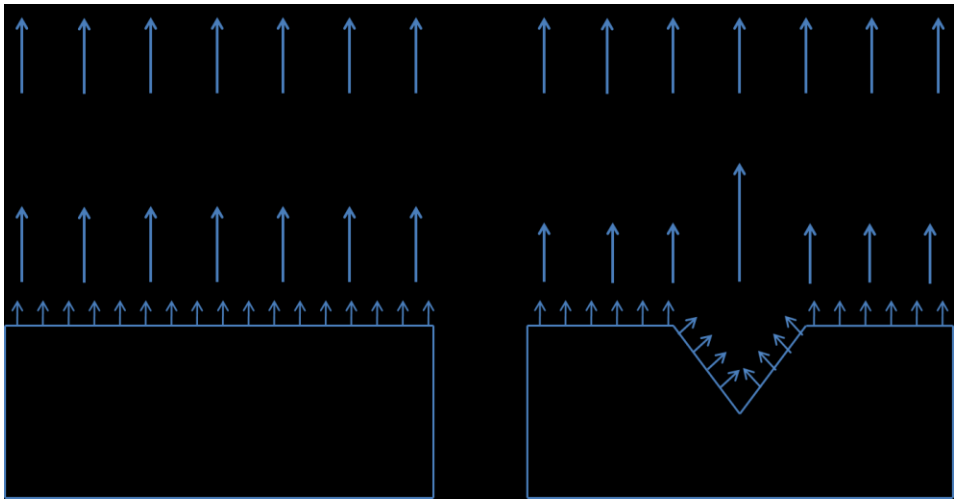

Figure 46: Schematic diagram of electric field in the vicinity of a groove. The increase in the effective metal surface area in the groove will lead to larger flux in the area directly above the feature. This corresponds to a stronger local electric field. The strong field directly above the groove will generate a Lorentz force that will influence the motion of a charged particle near the surface.

Particle motion studies were conducted in a parallel plate capacitor system that showed little to no observable motion due to Lorentz forces at applied potentials of 1 V (typical deposition potential for the Nickel system), however net directional velocities

were observed at 1.5 V. This indicates that increasing the local electric field flux from complex geometries is a plausible explanation for the lack of particles in the grooved regions. This method demonstrates manufacturing 3D hierarchical structures is feasible using substrate modification in conjunction with electrochemical co-deposition of composites.

5.4 Conclusions and Implications

Although hierarchical composite structures have been proposed as potentially beneficial material systems for some time, little progress had previously been made on actually manufacturing these materials in a controlled manner at relevant length scales. Co-deposition of metal matrix – ceramic nanoparticle composites presents a unique means of precisely manufacturing uniformly dispersed and higher order composite structures. Here this technique was used to manufacture large scale UDCs and layered hierarchical composite structures. Robust, crack free Ni films were manufactured with up to 25% Al_2O_3 350 nm particles by volume. The UDC samples showed expected mechanical enhancements with increasing hardness and yield strength according to an Orowand bowing mechanism. These samples also tended sacrifice ductility and toughness for this strength enhancement. Layered hierarchical composites showed unique mechanical properties with hardness and yield strengths increasing inversely to layer thickness. These layered materials can even demonstrate hardnesses and yield strengths higher than either base constituent, well beyond the rule of mixtures. These samples are

also qualitatively more ductile than UDC samples as. In addition to these basic structures, we have also shown that substrate manipulation can be used to generate more complex three dimensional hierarchically structured composites. This technique can be used to precisely manufacture high order composite structures and that those structures can lead to interesting and beneficial material properties.

These materials are already at industrially relevant size scales and may have immediate applications as surface wear coatings or stand-alone materials. In addition to the mechanical properties explored here, there may be interesting fracture toughness, high temperature, dynamic loading, and fatigue properties that stem from these structures that warrant future exploration. Cracks forming in the system will have to deflect around the hard particles in order to propagate through the material and the plastic zone around a crack tip travelling through the soft layer will be relatively large. Both of these mechanisms could provide improvements in fracture toughness and fatigue properties. Ni in particular is used in high temperature engine alloys and magnetic rotors so mechanical and magnetic performance under these conditions may prove beneficial. Dynamic loading and shear waves are known to reflect off of surface interfaces so controlled ordering in a composite may provide a means of tuning the dynamic response of a material. This process is also conducive to manufacturing other desirable microstructures with controlled compositional variance in multiple dimensions opening a large avenue of material systems and microstructures for future exploration.

5.5 References

1. Shao, X. Synthesis and Characterization of Soft Magnetic Thin Films, Nanocomposites, and Nanowires by Electrodeposition. (2002).
2. Shao, I., Vereecken, P. & Chien, C. Synthesis and characterization of particle-reinforced Ni/Al2O3 nanocomposites. *Journal of Materials Research* **17**, 1412-1418 (2002).
3. Garcia, I., et al. Electrodeposition and Sliding Wear Resistance of Nickel Composite Coatings Containing Micron and Submicron SiC Particles. *Surface & Coatings Technology* **148** (2001)
4. Lee H.K., et al. Codeposition of Micro- and Nano-Sized SiC Particles in the Nickel Matrix Composite Coatings Obtained by Electroplating. *Surface & Coatings Technology* **201** (2007)
5. Low, C.T.J., et al. Electrodeposition of Composite Coatings Containing Nanoparticles in a Metal Deposit. *Surface & Coatings Technology* **201** (2006)
6. Low, C., Wills, R. & Walsh, F. Electrodeposition of composite coatings containing nanoparticles in a metal deposit. *Surface and Coatings Technology* **201**, 371-383 (2006)
7. Jackson, A.P., Vincent, J.F.V. & Turner, R.M. The Mechanical Design of Nacre. *Proceedings of the Royal Society B: Biological Sciences* **234**, 415-440 (1988).
8. Rho, J.Y., Kuhn-Spearing, L. & Zioupos, P. Mechanical properties and the hierarchical structure of bone. *Medical engineering & physics* **20**, 92-102 (1998).

9. Barthelat, F. & Zhu, D. A novel biomimetic material duplicating the structure and mechanics of natural nacre. *Journal of Materials Research* **26**, 1203-1215 (2011).
10. Mortensen, A. & Suresh, S. Functionally graded metals and metal-ceramic composites: Part 1 Processing. *International Materials Reviews* **40**, 239-265 (1995).
11. Suresh, S. & Mortensen, A. Functionally graded metals and metal-ceramic composites: Part 2 Thermomechanical behaviour. *International Materials Reviews* **42**, 85-116 (1997).
12. Kieback, B., Neubrand, a. & Riedel, H. Processing techniques for functionally graded materials. *Materials Science and Engineering: A* **362**, 81-106 (2003).
13. Giannakopoulos, A., Suresh, S. & Finot, M. Elastoplastic analysis of thermal cycling: layered materials with compositional gradients. *Acta metallurgica et mater.* **43**, 1335-1354 (1995).
14. Anderson, P. & Li, C. Hall-Petch relations for multilayered materials. *Nanostructured materials* **5**, 349–362 (1995).
15. Erdogan, F. Fracture mechanics of functionally graded materials. *Composites Engineering* **5**, 753-770 (1995).
16. Bull, S. & Jones, A. Multilayer coatings for improved performance. *Surface and Coatings Technology* **78**, 173–184 (1996).
17. Michel, J.C., Moulinec, H. & Suquet, P. Effective properties of composite materials with periodic microstructure: a computational approach. *Comput. Methods Appl. Mech. Engng.* **172**, 109-143 (1999).

18. Singha, M.K., Prakash, T. & Ganapathi, M. Finite element analysis of functionally graded plates under transverse load. *Finite Elements in Analysis and Design* **47**, 453-460 (2011).

19. Olatunji-Ojo, a. O., Boetcher, S.K.S. & Cundari, T.R. Thermal conduction analysis of layered functionally graded materials. *Computational Materials Science* **54**, 329-335 (2012).

20. Farias, S., et al. (Invited) Manufacturing of Hierarchical Composite Structures via Controlled Ceramic Nanoparticle Incorporation in Electrodeposited Thin Films. *ECS Transactions*, **41** (2012)

Appendix A: Select Microtensile Data of Ni-Al_2O_3 Nanocomposites

This appendix shows selected representative tensile data of uniformly dispersed and layered hierarchical Ni-Al_2O_3 composite structures. While these results are summarized in Chapter 5, this appendix will detail the data analysis, property determination, and reproducibility discussed previously. Figure 47 shows an example of two microtensile stress-strain curves for a UDC composite sample. There is good agreement between these independent samples of similar microstructure.

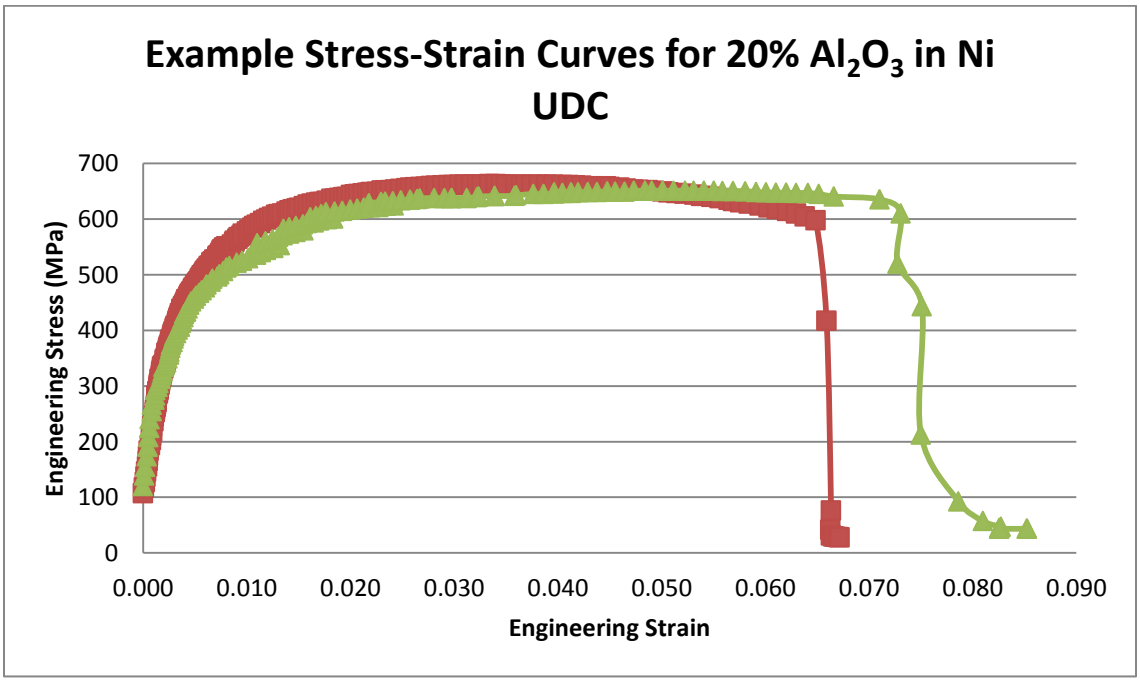

Figure 47: Example Stress-Strain Curves for 20% Al_2O_3 in Ni UDC Composites. These microtensile curves show two independent samples with equivalent microstructures.

Appendix A: Select Microtensile Data of Ni-Al2O3 Nanocomposites

Figure 48 shows a 0.2% offset strain used to determine the yield strength of a sample. The slope of the stress-strain curve at small strains is determined by a linear fit. This slope is then used to create a line offset from the experimental curve by 0.2%. The intersection of these two curves is taken to be the yield strength of the sample. In general the calculated slope is between 100-300 GPa which is the appropriate range for the composite samples based on the constituent materials. Slip in the instrumentation and between the sample and the grips can occur during initial loading and there is some variability in the pre-load amount so this is not a precise method for determining the modulus but still results in fairly consistent yield stresses.

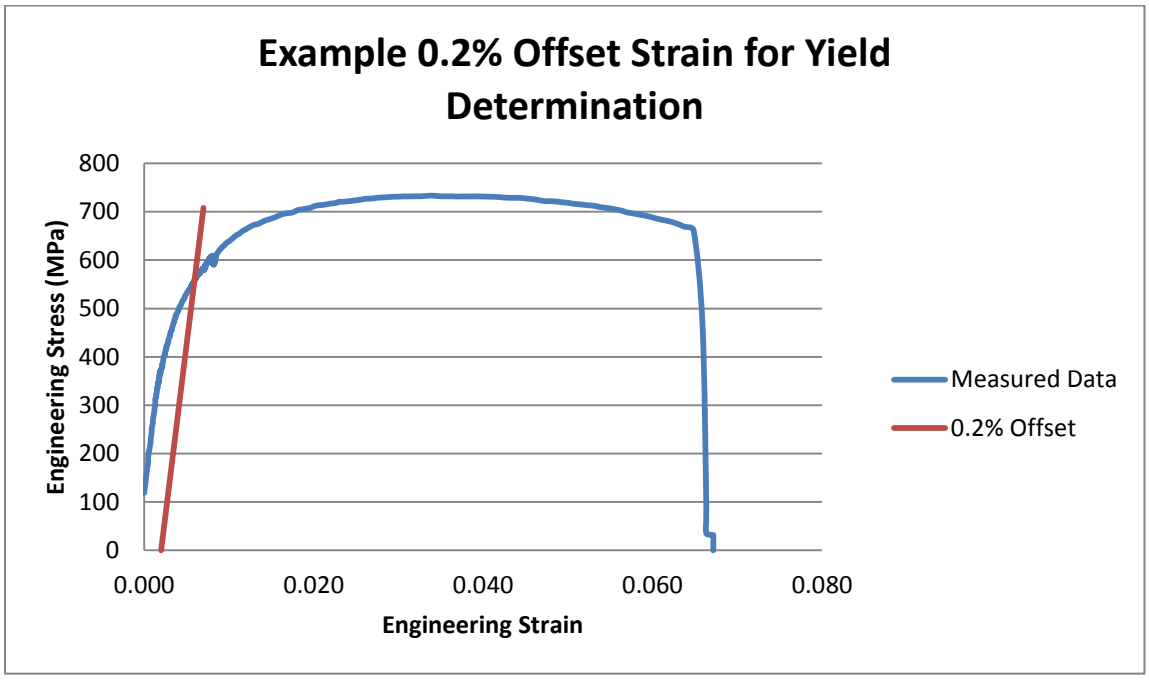

Figure 48: Example of 0.2% Offset Strain Yield Determination.

Appendix A: Select Microtensile Data of Ni-Al2O3 Nanocomposites

Figure 49 shows another set of typical stress-strain curves observed for samples of equivalent microstructure. While the samples show similar behavior early on during deformation, they have very different strain to failures. This variability is likely due to surface defects created during cutting and handling of the micro-specimens. The small thicknesses of these samples (~100 microns) make them particularly sensitive to this type of damage. This makes it difficult to determine a true intrinsic strain to failure from these tests.

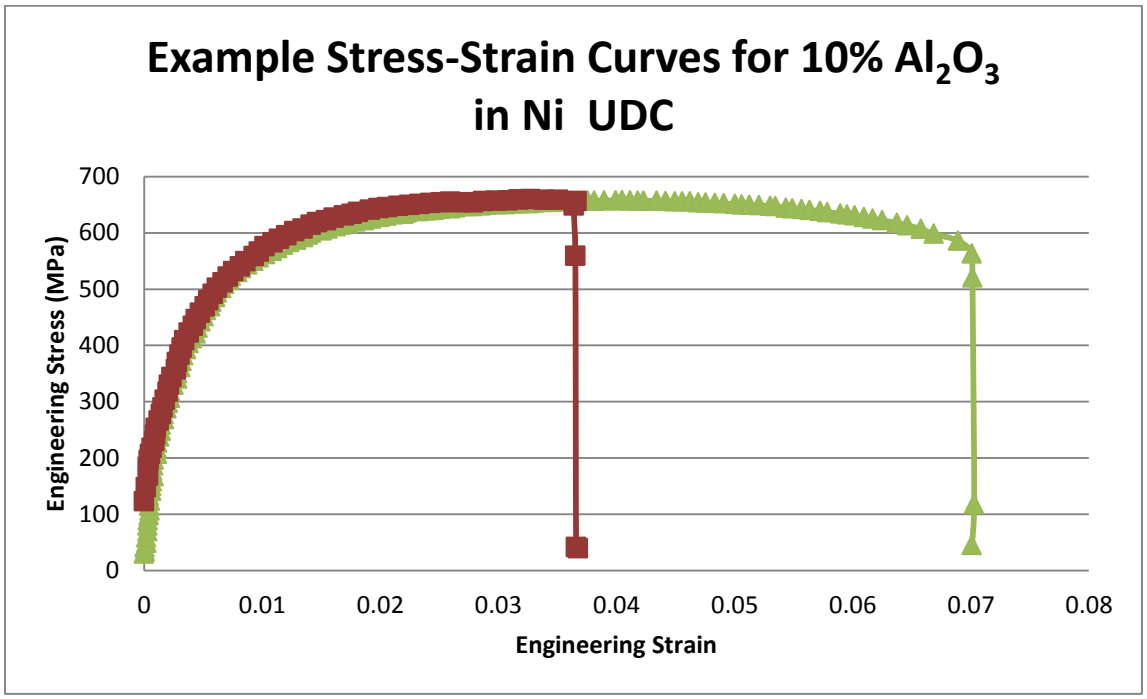

Figure 49: Example Stress-Strain Curves for 10% Al_2O_3 in Ni UDC Composites. These microtensile curves show two independent samples with equivalent microstructures.

Appendix A: Select Microtensile Data of Ni-Al2O3 Nanocomposites

Representative stress-strain curves for pure Ni and UDC Al_2O_3 in Ni are shown in Figure 50. Several tensile tests were run on independent samples from each microstructure. These curves are taken from samples that showed significant ductility. The strain to failure should only be decreased from the damage susceptibility described previously so these samples are the best representation of changes in intrinsic values. Increasing the particle volume fraction increases the yield strength and subsequently decreases the ductility and toughness of the sample.

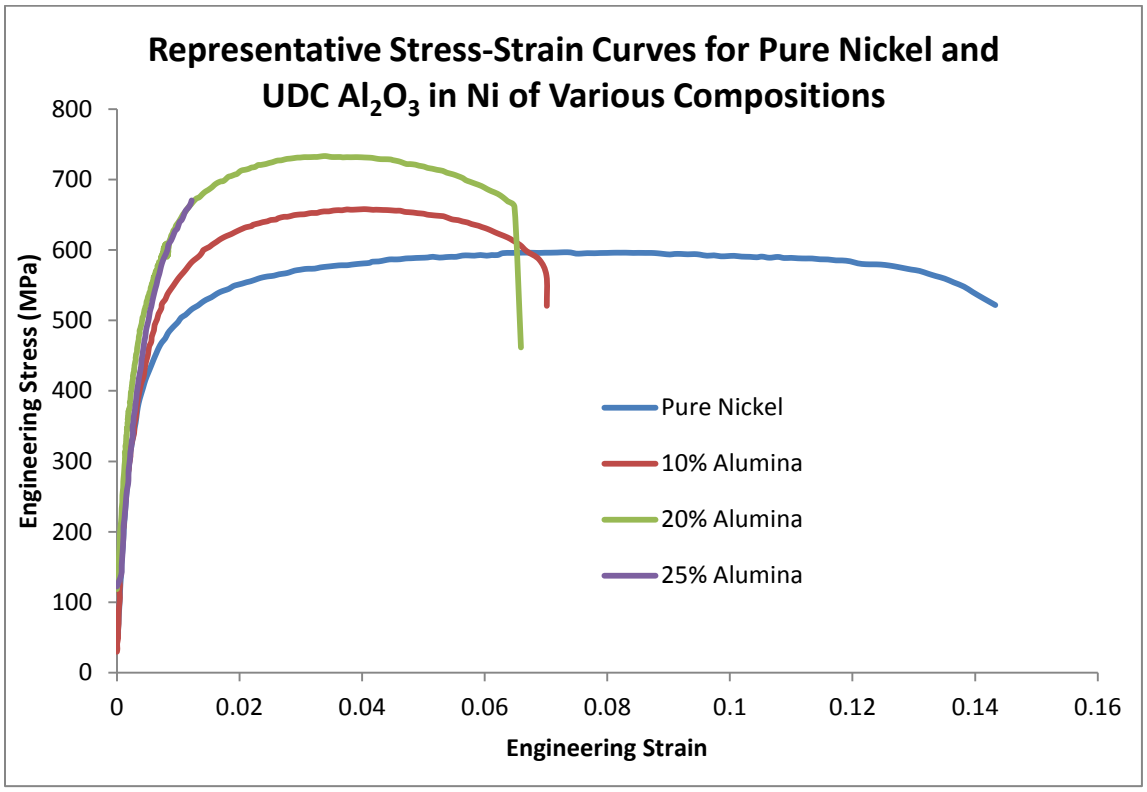

Figure 50: Stress-Strain Curves for Pure and UDC Composite Samples.

Appendix A: Select Microtensile Data of Ni-Al2O3 Nanocomposites

The layered hierarchical composite stress-strain curves have more complicated trends as they show high strengths until the individual layer spacing (~0.5 x the bilayer spacing) approaches the interface resolution of the sample. Below this microstructural resolution limit, the composite tends to behave more like a uniformly dispersed composite rather than a layered one. Figure 51 shows some representative curves for samples of different bilayer thicknesses with layers of nominally pure nickel and layers of 20% 350nm alumina particles by volume. The large thicknesses (5-7 microns) showed strengths similar to or greater than those measured in a 20% 350nm alumina UDC. Samples with bilayer thicknesses below 5 microns had lower strengths (similar to those seen in a 10% 350nm alumina UDC) but substantial increases in measured ductility. Fractography of the composites supports evidence that introduction of pure nickel layers into the composite samples increases ductility, however the variability in strain to failure makes determination of an intrinsic ductility and toughness difficult.

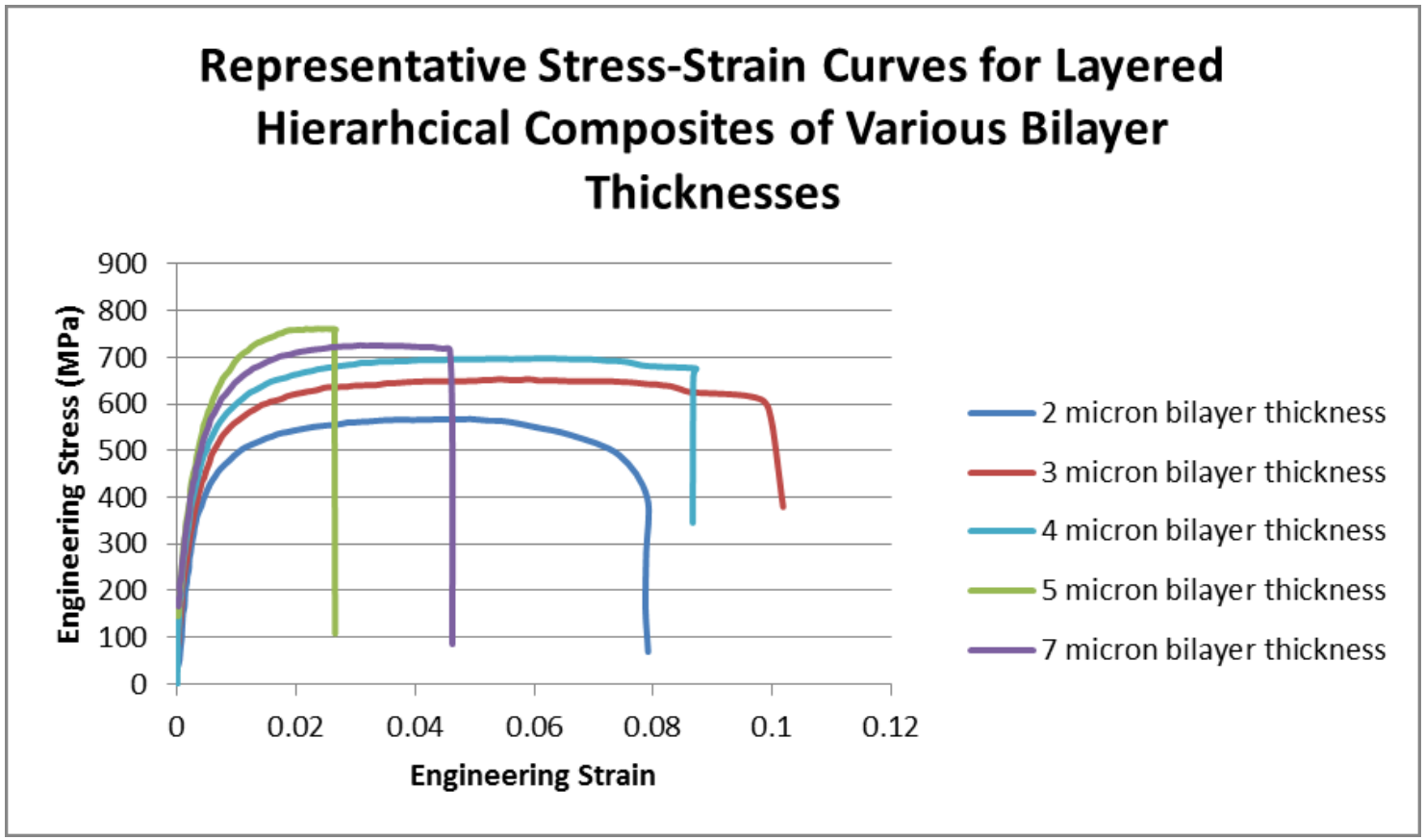

Figure 51: Representative Stress-Strain Curves for Layered Hierarchical Composites with Composite Layers of 20% alumina by volume. These tensile curves show an increase in strength with a reduction in bilayer spacing from 7 to 5 microns but decreases in strength with further reductions in thickness as the structure becomes indistinct and more like a UDC.

Curriculum Vita

Stephen Farias joined the Johns Hopkins University Department of Materials Science and Engineering under Prof. Robert Cammarata after completing a Bachelors of Science & Engineering in Mechanical and Aerospace Engineering at Princeton University in 2007. During his time at Hopkins he worked on several research projects including studies on electrodeposition of elemental thin films, electrodeposition of composites, electrodeposition of thermoelectric compounds, fabrication of nanostructured materials, and manipulation and purification of nano-entities in non-uniform electric fields. A list of relevant authored publications, conference proceedings, and patents is given below.

In addition to this research work, Stephen was also active in graduate student groups, outreach work, and in organizing department events. He served as the department representative to the graduate student government from 2008 – 2014 and the university travel grants committee from 2008 – 2010. He organized many departmental and campus-wide events including invited speaker seminars, graduate student happy hours, and intramural sports. He volunteered to mentor Baltimore area high-school students through MRSEC and NSF summer intern programs and through outreach events at the Maryland Science Center. He has also served a volunteer mentor to at-risk students in Baltimore City through the Incentive Mentoring Program.

Curriculum Vita

Publications and Proceedings

1. S. Farias, P. Breysse, et al. Layered and Functionally Graded Nanocomposite Thin Films with Unique Mechanical Properties. *MRS Proceedings*, **1304** (2011)
2. S. Farias, A. Young, et al. (Invited) Manufacturing of Hierarchical Composite Structures via Controlled Ceramic Nanoparticle Incorporation in Electrodeposited Thin Films. *ECS Transactions*, **41** (2012)
3. S. Farias, N. Dee, et al. Effects of Pb Mediation on Stress Evolution of Ag Electrodeposited Films. *in writing*
4. S. Farias, N. Dee, et al. Improved Microstructure and Resistivity of Cu Electrodeposited Thin Films Using Single Additive Mediated Growth. *in preparation*
5. S. Chi, S. Farias, et al. Synthesis of Vertically Aligned Gold Nanowire-Ferromagnetic Metal Matrix Composites. *ECS Transactions*, **41** (2012)
6. S. Chi, S. Farias, et al. A Novel Approach to Synthesize Lanthanum Telluride Thermoelectric Thin Films in Ambient Conditions. *MRS Proceedings*, **1543** (2013)
7. S. Chi, S. Farias, et al. A Novel Approach to the Synthesis of Nanochanneled Nickel Membranes. Submitted to MRS Communications, (2013)

Patents

1. Su Chi, R. C. Cammarata, C. L. Chien, Donglei Fan, Stephen Farias, and Danru Qum "Systems and Methods for Separating Metallic and Nonmetallic Particles in a Mixed-Particle Suspension " (US patent, 13/902,191, Submitted June, 2013)